Composite Silver/Titania Photocatalysts for Visible Light Water Splitting: The Role of Silver Surface Plasmons

by

David Brooke Ingram

A dissertation submitted in partial fulfillment
of the requirements for the degree of
Doctor of Philosophy
(Chemical Engineering)
in The University of Michigan
2011

Doctoral Committee:

Associate Professor Suljo Linic, Chair
Professor Phillip E. Savage
Professor Johannes W. Schwank
Associate Professor Max Shtein

"New knowledge is the most valuable commodity on earth.
The more truth we have to work with, the richer we become."
—Kurt Vonnegut

This dissertation is dedicated to my loving wife Nicki and my wonderful son Elliott. This would not have been possible without your boundless love and support.

ACKNOWLEDGEMENTS

I would first like to thank my advisor, Professor Suljo Linic, who has been a fantastic mentor and colleague throughout my time at the University of Michigan. Suljo's dedication to and genuine interest in pursuing novel research was a great motivator. He also gave me the opportunity to attend many conferences, which have greatly benefited my development as a scientist and helped me make many professional contacts that will serve me well throughout my career. I would also like to thank my thesis committee: Professors Johannes Schwank, Philip Savage and Max Shtein. The comments provided during the data meeting, on the written dissertation and during the thesis defense have been exceedingly useful and have resulted in a significantly improved dissertation. I am also thankful for the other ways in which the faculty have helped—particularly Professors Schwank and Savage as well as Professor Nicolas Kotov—from providing access to equipment and professional contacts to training talented students and fostering a sense of collaboration.

I would also like to acknowledge all of the members of the Linic Research Group, past and present. When I started as a PhD student, the students in the group (Dr. Siris Laursen, Dr. Eranda Nikolla, Dr. Joydeep Mukherjee, Dr. Neil Schweitzer, Hongliang Xin and Andrew Getsoian) were instrumental in teaching me many scientific and engineering concepts, as well as helping me learn how to conduct research. Phillip Christopher, who joined the lab at the same time as I did, and Adam Holewinski, who joined a year later, have both been great friends and colleagues. I

have enjoyed learning along side them and I know they have taught me much more than I have taught them. Their constant dedication and hard work has certainly inspired me to work harder on my projects. The younger students in our group have also been very helpful in many ways, and I wish them continued success: Matt Morabito, Marimuthu Andiappan, Katrina Ramsdell, Thomas Yeh, Michelle Przybylek, Brittany Lancaster, Tim Van Cleve, Paul Hernley and Jianwen Zhang. I was also lucky enough to work directly with two outstanding undergraduate students in the lab: Jonathan Bauer and Michael Maas. Both were incredibly helpful running experiments in the lab and analyzing data. I have every confidence that they will both excel in graduate school and beyond.

My friends and family also deserve a large portion of the credit for my success. My parents Peggy and Sid Ingram have always been supportive throughout my academic training, encouraging me to pursue my scientific interest and providing moral and financial support along with the way. I also have to thank my sister Melissa Smar and grandmother Mary Brooke, who have always been supportive and encouraging in many different ways. My friends in Ann Arbor have in many ways formed a surrogate extended family for my wife, son and me—Megan and Joe Mayne, Amy and Jim Bucher, Michelle and Daniel Lilly, Tom Westrich and Meghan Cudihy, Kevin Critchley and Georgina Wilkins. I am grateful to get to share in the lives of these newly married couples, and am so appreciative of all the free baby sitting and the numerous other ways in which they have enriched my family's life.

I owe a huge debt of gratitude to my longtime friend—and "partner in crime" as he likes to say—Prachi Gauriar. Prachi has always been there with a sympathetic ear and sage advice. He also spent an incalculable amount of time helping me with our computer cluster and various programming tasks. Finally, the most important

people to thank are my wife Nicki and son Elliott. This dissertation would not have been possible without their love and support. Being a graduate student is not always easy, but I think being the spouse of a graduate student is even more difficult. So, from the bottom of my heart, thank you.

TABLE OF CONTENTS

LIST OF FIGURES

Figure

CHAPTER 1

Prologue

1.1 Summary

The current magnitude of global energy demands is presented and some problems with the continued reliance on fossil fuels are discussed. Potential solutions to these problems are discussed, particularly the use of solar energy to synthesize solar fuels using semiconductor photocatalysts. The general topic, scope and organization of this dissertation are detailed.

1.2 Global Energy Production

Global primary energy consumption in 2008 was approximately 500 quadrillion BTU ($\sim$5 x 10^{20} J) [1], which corresponds to an average energy consumption rate of approximately 16 terawatts (TW). These figures are projected to grow as the world's population reaches nearly 10 billion by 2050 [1]. Even though energy intensity is steadily declining, global primary energy consumption is projected to increase to 27 TW by 2050 and 43 TW by 2011 [2], as shown in Figure 1.1b. Approximately 85% of world's energy in 2008 was provided in the form of fossil fuels (oil, coal and natural gas) [1]. Renewable sources accounted for only $\sim$5%, with the majority coming from hydroelectric generation [1].

Many estimates report that there are enough proven reserves of conventional fossil

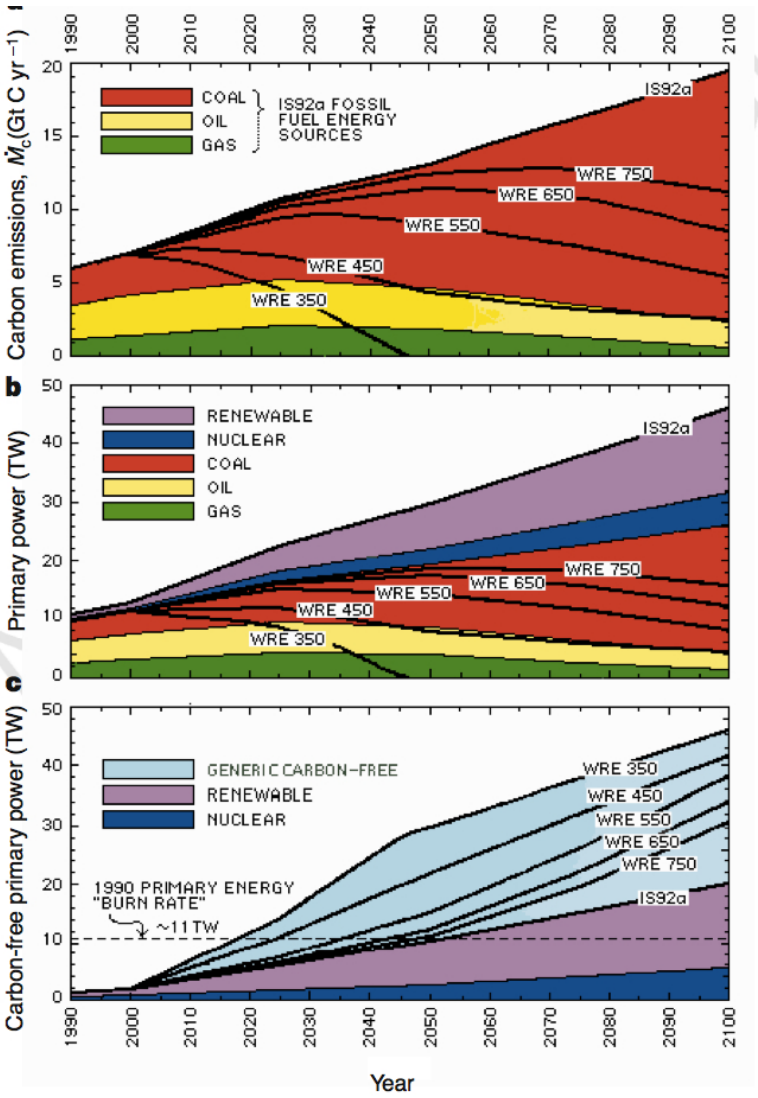

Figure 1.1: Projections of global carbon emission rates and energy consumption rates from ref. [2]. (a) Carbon emissions in gigatons of carbon per year (GtC/yr) projected to year 2100. Black lines show total emission for different projection models. Colors indicate the fraction of the total due to coal, oil and natural gases sources. (b) Global energy consumption rate (primary power) projected to year 2100 and fractions from different energy sources. (b) Projections of required carbon-neutral energy rates to meet the carbon emission goals in (a) under different projections. IS92a refers to the base case, which assumes trends as of 1998 remain unchanged. WRE 350 indicate projections and requirements to stabilize atmospheric CO_2 levels at 350 ppm by volume (likewise WRE 450–750).

fuels to supply the world's energy use at a constant consumption rate of ∼30 TW for several centuries. For example, based on 1998 rates of consumption, the World Energy Assessment Report [3] estimated that there are approximately 50–150 years of proven crude oil and natural gas reserves as well as an additional 200–500 years of natural gas reserves if oceanic methane clathrates are included. Furthermore, the report indicated 1,000 to 2,000 years of other fossil fuel resources (coal, oil shale and tar sands).

1.3 Challenges to Continued Fossil Fuel Use

Continued heavy reliance on fossil fuels, however, has several potential problems, the first of which is economic in nature. Oil prices are forecast to continue to increase, with various estimates predicting a steady increase in the average annual price to approximately $125–200 per barrel (in 2008 dollars, i.e. not including increases due to inflation) by the year 2035 [1]. This is compared to an average 2008 value of approximately $80.

Another major problem of continued fossil fuel use is the potential impact on the environment caused by sustained and increased carbon emissions. As mentioned above, despite a decrease in energy intensity, the world's energy consumption rate is projected to significantly increase simply due to an increase in population. It is estimated that at current consumption and emission rates the rate of carbon emission globally will increase from the 2001 value of 6.6 gigatons of carbon per year (GtC/yr) to 13.5 GtC/yr by 2050 [2, 4], see Figure 1.1a. The exact effects on the environment of anthropogenic carbon emissions are still uncertain and are hotly debated. However, what is clear is that modern human society is causing elevated emissions of CO_2. It is also clear from several very long-term geological data sets (up

to 650,000 years in the past [5, 6]) that, over this time period, elevated global average temperatures have been strongly correlated with—but not necessarily caused by—elevated levels of CO_2 in the atmosphere. The main naturally occurring mechanism of carbon removal from the atmosphere is dissolution in the world's oceans; however, equilibration times between the atmosphere, the near-surface layer of the oceans and the deep oceans are between 400 and thousands of years [7]. The result is that, without intervention such as sequestration technologies, whatever effects may be caused by the next several decades of elevated carbon emissions will likely persist in the environment for hundreds to thousands of years.

To cap carbon emissions at current rates, and prevent future increases as global energy consumption continues to increase, it is projected that at least 10 TW of energy will need to be provided by carbon-neutral sources by 2050 [2]. Reduction in the current carbon emission rate will of course require even more of the global energy portfolio to be carbon-neutral (up to 30 TW by 2050 based on some carbon reduction plans [2]). Some carbon reductions can be effected by improvements in energy efficiency (e.g. vehicle fuel economy). However, it is clear that new large-scale carbon-neutral energy sources need to be developed to meet these challenges.

1.4 Solar Energy

The total world energy consumption for the entire year of 2008 ($\sim$5 exajoules) is equivalent to the energy of sunlight striking the earth for just 70 minutes (the average energy rate from the sunlight striking the earth's surface is $\sim$120,000 TW [8]). However, currently only approximately 1.5% of global energy production comes from a solar source (mostly biomass) [1]. There are many potentially promising research avenues for utilization of solar energy. For instance, large-scale biomass could po-

tentially make a significant impact. Some projections estimate that if energy crops (e.g. switchgrass) were planted on all of the world's naturally irrigated land area not needed to grow food, the maximum energy output would be just 5–10 TW [7]. However, other biomass technologies (and combinations of technologies) such as algae and cellulosic biomass hold significantly more hope for meeting the future carbon-neutral energy requirements [7, 9]. Direct electricity production using photovoltaic (PV) cells is another interesting avenue. While very large, the land area requirements for 10 TW of PV energy are certainly attainable, particularly when considering distributed generation point sources. One problem with PV energy is that a separate storage technology is required to overcome natural temporal and spatial variations of solar flux, and it is not clear what the best options are. Significant increases in PV and storage efficiency, and even large improvements in cost, are required to make the technology practical, but this is certainly an avenue worth serious pursuit.

1.5 Solar Fuels

Another particularly promising solar energy technology, and the focus of this dissertation, is the direct production of solar fuels using sunlight. The idea here is essentially to mimic nature, in a way, by using a photocatalyst that can absorb sunlight and use electrochemical reactions to convert the photon energy into the energy of chemical bonds (the specific physical processes are discussed in Chapter 2). The net effect is that solar energy can be used to directly transform a low energy compound such as water into a high energy one (hydrogen). Because of this bio-mimicry concept, this technology is often referred to as artificial photosynthesis, as depicted in Figure 1.2 [10]. Reactions such as solar production of hydrogen from water are often referred to as photosynthetic reactions because the resulting

fuel (H_2) has a higher energy value than the reactant (H_2O), i.e. the reactions are endothermic. This term is used to distinguish solar fuel reactions from exothermic photoreactions (e.g. photo-induced decomposition reactions), which do not yield high energy (or high value) products. This distinction will be made in more detail in Chapter 2. Because natural (botanical) photosynthesis uses both CO_2 and H_2O as reactants, the term artificial photosynthesis is occasionally limited to photo-processes that convert—simultaneously or in tandem—both CO_2 and H_2O to useful fuels, but this stricter definition is not pervasive. Throughout this thesis we focus primarily on the production of hydrogen from water using the energy of light and do not discuss CO_2 activation.

1.6 Scope of the Dissertation

It has been known for several decades that certain semiconductors can absorb photons in the UV-visible portion of the electromagnetic spectrum, and use the absorbed energy to activate water, producing hydrogen and oxygen. This phenomenon, called the Fujishima-Honda effect [11], is discussed in detail in Chapter 2. While this technology has been investigated for 40 years, the process produces hydrogen at very low rates because of inherent deficiencies of the semiconductors. More recent progress has demonstrated that adding metal nanoparticles to the semiconductor can enhance the photocatalytic rates through a variety of phenomena (Chapter 2) [12–25]. If the metal nanoparticles are specially tailored they can also interact with the UV-visible photons through the excitation of surface plasmons [26–29]. Very recently it was demonstrated that this interaction is potentially a much more powerful way to enhance the semiconductor activity [17, 19, 20, 23–25]. This specific class of composites photocatalysts, which comprises a conventional semiconductor and specifically

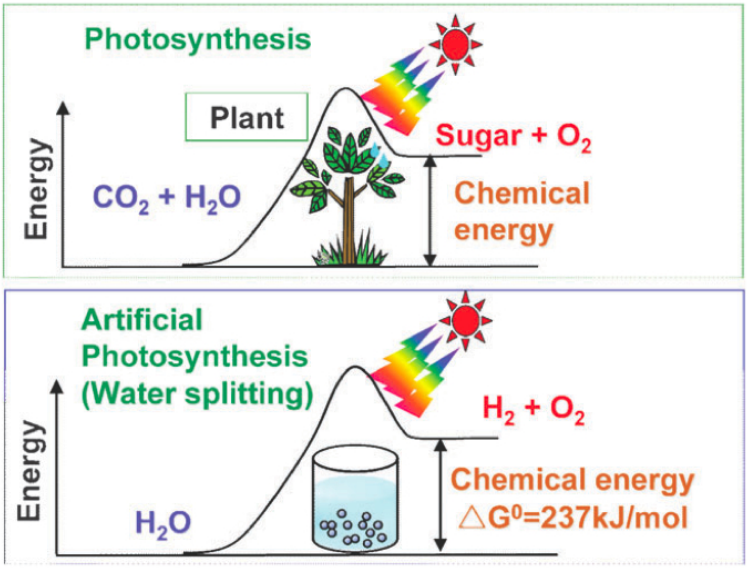

Figure 1.2: Natural photosynthesis versus artificial photosynthesis from ref. [10]. (a) In natural photosynthesis, plants use biological photocatalysts to absorb photons and transfer the energy of the light into energy of bonds, transforming CO_2 and H_2O into sugars and oxygen. (b) In artificial photosynthesis, a semiconductor photocatalyst is used to absorb photons and channel the energy of the light into the energy of chemical bonds, transforming a low value reactant such as water into hydrogen.

designed plasmonic metal nanoparticles, is the focus of this dissertation. We use a range of experimental, theoretical and computational tools to investigate the underlying physical mechanisms that govern the enhancements. We demonstrate the construction and evaluation of the new composite materials. And we construct models that capture and predict their behavior, which can be used to guide the design of optimized composite photocatalysts, especially when used in conjunction with other advances being pursued in parallel in other labs and in other fields (for example, advanced synthesis techniques).

1.7 Organization of the Dissertation

This short introduction is followed by Chapter 2 "Semiconductor Photocatalysis", which introduces the physical phenomena behind photocatalytic transformations on the surface of a semiconductor, especially the Fujishima-Honda effect [11]. The chapter focuses on the photocatalytic splitting of water to form hydrogen and oxygen; however, photo-decomposition of organic compounds is also discussed briefly. A list of required attributes for semiconductor photocatalysts is discussed and in the context of this list, the major common deficiencies of current semiconductor materials are discussed. Finally, the chapter introduces a particularly promising strategy for the development of improved photocatalysts (i.e. combining the semiconductor materials with specially designed metal particles).

Chapter 3 "Synthesis, Experimental and Computational Methods" contains detailed descriptions of various methods used throughout the thesis (primarily Chapters 4, 5 and 6). The chapters themselves contain short methods sections, which present crucial information regarding methodology specific to that particular chapter, as well as references to specific sections within Chapter 3 for further information.

Chapter 4, "Predictive Models for Plasmonic Metal/Semiconductor Photocatalysts" presents some initial investigations of the enhancement of semiconductor activity by the addition of photo-excited plasmonic metal nanostructures. The activity, as measured by an organic decomposition test reaction, is tested for several different composite samples with different optical properties. This allows for the construction of a model that effectively captures the enhancement mechanism by taking into account only the constituent elements' optical properties. This method is extended, with the aid of optical simulations, to create a theoretical model to predict the optimum design of this class of semiconductor photocatalysts based on selection of the optical characteristics.

Chapter 5, "Plasmon-Enhanced Water Splitting" builds on the concepts in Chapter 4 to design and test a composite plasmonic metal/semiconductor photocatalyst that demonstrates enhanced activity for the production of hydrogen and oxygen from water, compared to that of the semiconductor alone [20]. It has been suggested based on optical simulations that the enhancement could be due to a non-homogeneous distribution of electric fields induced by the metal plasmon resonance [17, 24]. This concept is tested and confirmed experimentally for the first time, providing crucial insights into the underlying physical mechanisms [20].

Chapter 6 "Geometric Model for Designing Plasmonic Metal/Semiconductor Composites" is motivated by the finding in Chapter 5. The demonstration in Chapter 5 that the enhancement is due to the spatially non-homogeneous distribution of electric fields induced by the plasmon resonance suggests that the geometric arrangement of building blocks in the composites is a key aspect of their design. In Chapter 6, this is experimentally tested by monitoring the performance of a set of photocatalysts as a function of changes in the geometric arrangement of the metal and semiconductor

building blocks. A theoretical model is developed that explains the dependence of the activity on geometry.

Chapter 7, "Conclusions and Future Outlook" summarizes the mechanistic insights gained throughout the previous chapters, to present a holistic view of the optimum design of composite plasmonic metal/semiconductor photocatalysts. A few important topics that continue to challenge the future application of this technology are discussed. These topics include potential strategies to improve overall efficiencies, problems and progress in large-scale implementation of the technology, and some basic economic considerations regarding broad use of water splitting as an energy production technology.

References

[1] U.S. Department of Energy, *Annual Energy Outlook*; Technical Report, 2011.

[2] Hoffert, M. I.; Caldeira, K.; Jain, A. K.; Haites, E. F.; Harvey, L. D. D.; Potter, S. D.; Schlesinger, M. E.; Schneider, S. H.; Watts, R. G.; Wigley, T. M. L.; Wuebbles, D. J. *Nature* **1998**, *395*, 881–884.

[3] United Nations Development Programme, *World Energy Assessment*; Technical Report, 2003.

[4] Intergovernmental Panel on Climate Change, *Third Assessment Report*; Technical Report, 2001.

[5] Petit, J. R. et al. *Nature* **1999**, *399*, 429–436.

[6] Siegenthaler, U.; Stocker, T. F.; Monnin, E.; Lüthi, D.; Schwander, J.; Stauffer, B.; Raynaud, D.; Barnola, J.-M.; Fischer, H.; Masson-Delmotte, V.; Jouzel, J. *Science* **2005**, *310*, 1313–1317.

[7] Lewis, N. S.; Nocera, D. G. *PNAS* **2006**, *103*, 15729–15735.

[8] Gust, D.; Moore, T. A.; Moore, A. L. *Acc. Chem. Res.* **2009**, *42*, 1890–1898.

[9] Agrawal, R.; Singh, N. R.; Ribeiro, F. H.; Delgass, W. N. *PNAS* **2007**, *104*, 4828–4833.

[10] Kudo, A.; Miseki, Y. *Chem. Soc. Rev.* **2009**, *38*, 253–278.

[11] Fujishima, A.; Honda, K. *Nature* **1972**, *238*, 37–38.

[12] Subramanian, V.; Wolf, E.; Kamat, P. V. *J. Phys. Chem. B* **2001**, *105*, 11439–11446.

[13] Arabatzis, I. M.; Stergiopoulos, T.; Bernard, M. C.; Labou, D.; Neophytides, S. G.; Falaras, P. *Appl. Catal. B* **2003**, *42*, 187–201.

[14] Subramanian, V.; Wolf, E. E.; Kamat, P. V. *J. Am. Chem. Soc.* **2004**, *126*, 4943–4950.

[15] Tian, Z.-Q.; Ren, B. *Annu. Rev. Phys. Chem.* **2004**, *55*, 197–229.

[16] Tian, Y.; Tatsuma, T. *J. Am. Chem. Soc.* **2005**, *127*, 7632–7637.

[17] Awazu, K.; Fujimake, M.; Rockstuhl, C.; Tominaga, J.; Murakami, H.; Ohki, Y.; Yoshida, N.; Watanabe, T. *J. Am. Chem. Soc.* **2008**, *130*, 1676–1680.

[18] Kowalska, E.; Abe, R.; Ohtani, B. *Chem. Comm.* **2009**, 241–243.

[19] Christopher, P.; Ingram, D. B.; Linic, S. *J. Phys. Chem. C* **2010**, *114*, 9173–9177.

[20] Ingram, D. B.; Linic, S. *J. Am. Chem. Soc.* **2011**, *133*, 5202–5205.

[21] Silva, C. G.; Juárez, R.; Marino, T.; Molinari, R.; García, H. *J. Am. Chem. Soc.* **2011**, *133*, 595–602.

[22] Primo, A.; Corma, A.; García, H. *Phys. Chem. Chem. Phys.* **2011**, *13*, 886–910.

[23] Kumar, M. K.; Krishnamoorthy, S.; Tan, L. K.; Chiam, S. Y.; Tripathy, S.; Gao, H. *ACS Catal.* **2011**, *1*, 300–308.

[24] Liu, Z.; Hou, W.; Pavaskar, P.; Aykol, M.; Cronin, S. B. *Nano Lett.* **2011**, *11*, 1111–1116.

[25] Hou, W.; Liu, Z.; Pavaskar, P.; Hung, W. H.; Cronin, S. B. *J. Catal.* **2011**, *277*, 149–153.

[26] El-Sayed, M. A. *Acc. Chem. Res.* **2001**, *34*, 257–264.

[27] Burda, C.; Chen, X.; Narayanan, R.; El-Sayed, M. A. *Chem. Rev.* **2005**, *105*, 1025–1102.

[28] Kelly, K. L.; Coronado, E.; Zhao, L. L.; Schatz, G. C. *J. Phys. Chem. B* **2003**, *107*, 668–677.

[29] Brus, L. *Acc. Chem. Res.* **2008**, *41*, 1742–1749.

CHAPTER 2

Semiconductor Photocatalysis

2.1 Summary

This chapter presents a brief introduction to photocatalytic transformations on semiconductors. We focus on a discussion of the photocatalytic splitting of water to form H_2 and O_2. Photocatalytic organic decomposition reactions are also briefly discussed. We discuss a list of requirements for a semiconductor photocatalyst and discuss the common deficiencies of many single-component materials. We also discuss the addition of metal nanoparticles to a semiconductor. The major approach reported in literature is the addition of co-catalysts, where the co-catalysts do not directly interact with light, but serve to increase the semiconductor activity through a few effects. However, recently it has been demonstrated that the addition of photo-excited metal nanoparticles can enhance the semiconductor activity through a range of possible interaction mechanisms, each of which can contribute to enhancing the photo-activity under certain conditions. The discussion in this chapter summarizes the major proposed mechanisms and lays the groundwork for more rigorous investigation and analysis of the enhancement mechanisms presented in the chapters to follow.

2.2 Introduction

As discussed in Chapter 1, the enormous solar flux at the earth's surface (∼120,000 TW) represents a unique capacity to provide a very large amount of clean, renewable solar fuels [1, 2]. However, this is contingent on the availability of materials that can efficiently capture sunlight and transform the energy of the photons into the energy of chemical bonds, effectively using the solar energy to upgrade a low-energy compound to a high-energy one. Heterogeneous photocatalysts for various light-induced chemical transformations, including splitting of water and decomposition of organic compounds, are almost exclusively semiconductors [3, 4]. Semiconductors are characterized by a filled valence band, which is separated in energy from the empty conduction band, as shown in Figure 2.1. This separation, called the band gap, defines the minimum amount of energy input necessary to move electrons from the valence to the conduction band. For example, valence electrons can be promoted to the conduction band by adding energy in the form of an electrical potential.

2.2.1 The Fujishima-Honda Effect

Interestingly, electrons can also be promoted by photons having energy that exceeds the semiconductor band gap. In 1972, it was realized that this phenomenon could be used to drive the photocatalytic splitting of water* to form H_2 and O_2 [5]. Electrolysis of water requires 1.23 V (or 1.23 eV). This is the same energy as a photon with wavelength of 1008 nm,† which this means that a large proportion of solar photons have sufficient energy (the solar spectrum is shown in Figure 2.1b). However, water is transparent to UV-visible (∼300–800 nm) light and in practice the direct

*For brevity and simplicity we will simply use the term "water splitting" to mean the production of H_2 and O_2 from water using light and mediated by a photocatalyst (typically a semiconductor). Electrolysis and direct photolysis of water are not discussed in this thesis, so this naming convention should not cause any confusion.

†The conversion of energy (in eV) to wavelength (in nm) is: $E[\text{eV}] = 1239.4/(\lambda[\text{nm}])$.

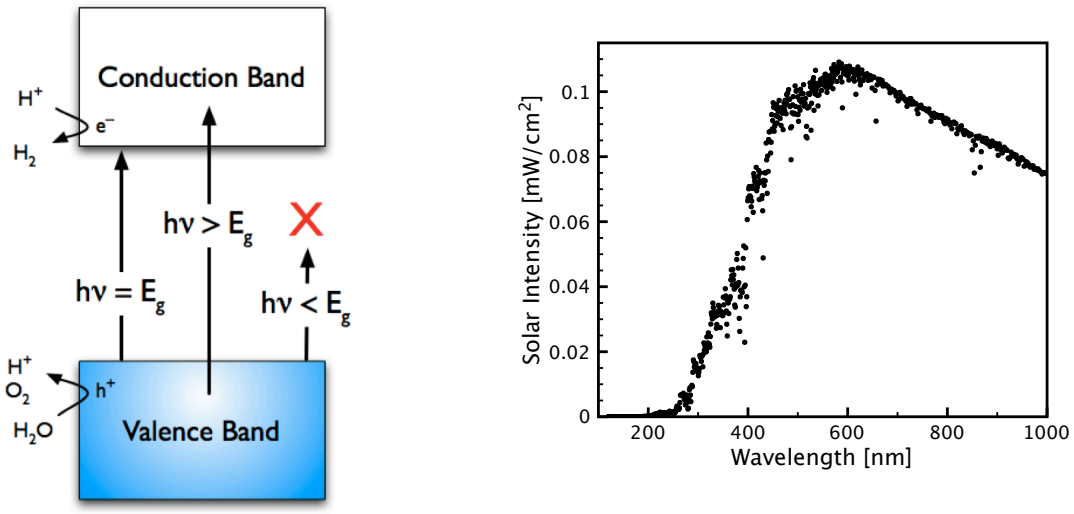

Figure 2.1: Schematic of a semiconductor band diagram and the solar spectrum. (a) Schematic of a semiconductor band diagram. The valance band and conduction band are separated by the band gap (E_g). Photons with energy equal to or exceeding the band gap can promote an electron from the valence to the conduction band, leaving behind an electron hole (h^+) in the valence band. Depending on the potentials, electrochemical half-reactions (for example, the water splitting half-reactions) can be activated by the photo-generated electrons and holes. (b) Intensity of solar light as a function of wavelength (total intensity $\sim$125 mW/cm^2); data for the AM1.5 solar spectrum are from the National Renewable Energy Laboratory (NREL), http://rredc.nrel.gov/solar/spectra/am1.5/. Direct photolysis of water requires photons with wavelength of less than 190 nm; however, via the Fujishima-Honda effect, photocatalytic water splitting could theoretically be accomplished (with the appropriate semiconductor) using photons with wavelength less than 1000 nm.

photolysis of water can be accomplished only with wavelengths shorter than 190 nm. Fujishima and Honda's discovery, sometimes called the "Fujishima-Honda effect", was that the photo-induced splitting of water could be catalyzed by an appropriate semiconductor (their initial discovery employed anatase phase TiO_2, but it has since been demonstrated for other semiconductors).

In this system, a flux of photons is absorbed by the semiconductor when the photon energy exceeds the energy of the material's band gap. An electron is promoted from the semiconductor valence band to the conduction band, leaving behind an empty state in the valence band (referred to as an "electron hole" or simply a "hole", h^+). Water splitting is an electrochemical process, described by the combination of the two half-reactions shown in Equations 2.1 and 2.2 for water splitting in acidic media.

$$H_2O + 2h^+ \longrightarrow 2H^+ + 1/2O_2 \tag{2.1}$$

$$2H^+ + 2e^- \longrightarrow H_2 \tag{2.2}$$

Or Equations 2.3 and 2.4 for water splitting in basic media.

$$2OH^- + 2h^+ \longrightarrow H_2O + 1/2O_2 \tag{2.3}$$

$$2H_2O + 2e^- \longrightarrow 2OH^- + H_2 \tag{2.4}$$

These half-reactions are referred to as the oxygen evolution half-reaction (Equation 2.1 or 2.3) and the hydrogen evolution half-reaction (Equation 2.2 or 2.4). We note that the two sets of reactions are equivalent and differ only by the water dissociation reaction, Equation 2.5.

$$H_2O \longrightarrow H^+ + OH^- \tag{2.5}$$

For example, by subtracting Equation 2.5 from Equation 2.1 twice, Equation 2.3 is obtained and by adding Equation 2.5 to Equation 2.2 twice, Equation 2.4 is obtained.

The overall water splitting reaction is the sum of the oxygen evolution and hydrogen evolution half-reactions ($H_2O + 2e^- + 2h^+ \longrightarrow H_2 + 1/2O_2$). As mentioned above, the overall redox potential of the water splitting reaction is 1.23 V. If the photo-generated holes have potential more positive than 1.23 V on the normal hydrogen electrode (NHE) scale, they can drive the oxygen evolution half-reaction. The photo-excited electrons can drive the hydrogen evolution half-reaction if their potential is more negative than 0 with respect to NHE.

The net effect is that the energy of UV-visible photons can be used to drive this highly endothermic chemical transformation (1.23 V equates to a heat of reaction of 237 kJ per mole of H_2O consumed),[‡] essentially allowing for the deposition and storage of solar energy into the energy of chemical bonds. Figure 2.2 presents a comparison of various semiconductor band positions and their alignment with respect to the water splitting half-reactions [6, 7]. This figure is a convenient way to demonstrate the first set of requirements of a photocatalyst for (unassisted) water splitting:

(1) The potential of the semiconductor valence band must be more positive than 1.23 V with respect to NHE.

(2) The potential of the semiconductor conduction band must be more negative than zero with respect to NHE.

(3) Although this is implied by (1) and (2) it is worth stating explicitly: because the overall water splitting redox potential is 1.23 V, the energy of the semiconductor band gap must exceed 1.23 eV.

These requirements are often summarized colloquially by stating that the semiconductor band gap must "straddle" the redox potentials. We note that system

[‡]The standard potential of water splitting is 1.23 V per electron. There are two electrons involved per H_2O molecule transformed, resulting in a total free energy change of 2.46 eV, or 237 kJ/mol.

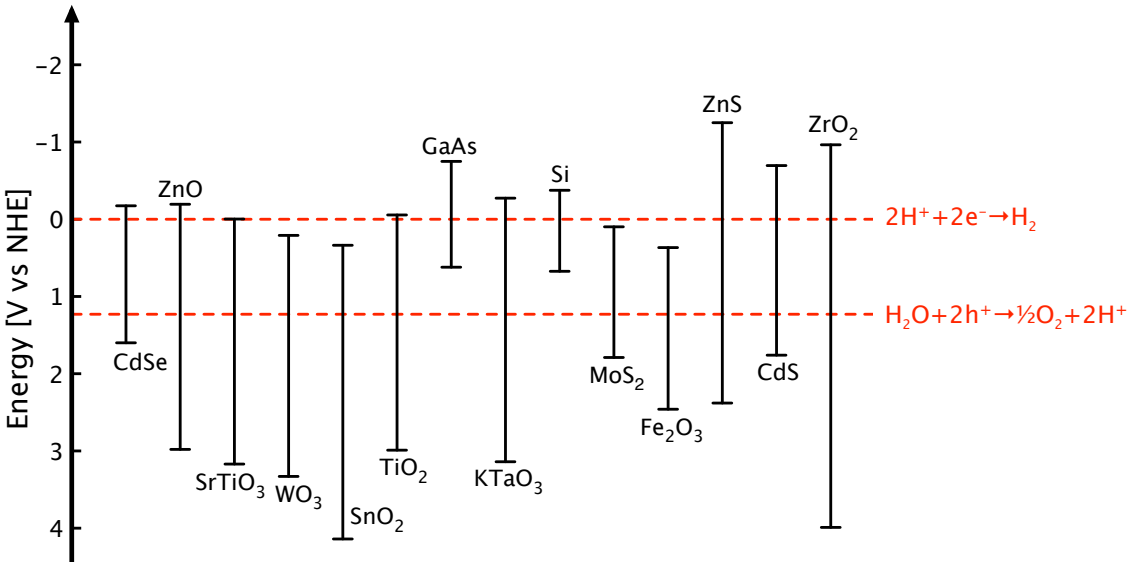

Figure 2.2: Positions of the valence band and conduction band for a range of semiconductors (data from references [6] and [7]). Redox potentials for the water splitting half-reactions versus the normal hydrogen electrode (NHE) are also indicated. For the water splitting reaction to be thermodynamically favorable, the band gap should straddle these redox potentials, i.e. the semiconductor conduction band should have higher energy (more negative potential) than the hydrogen evolution potential (0 vs NHE) and the valence band should be lower in energy (more positive potential) than the oxygen evolution potential (1.23 V).

charge neutrality is required; therefore, at steady state it is not possible for only one half-reaction to proceed at a time. Both electrons and holes must satisfy the potential requirements above for overall water splitting. However, it is possible for a system to perform only one water splitting half-reaction if another electrochemical half-reaction proceeds to balance the charge (this is generally accomplished by using a sacrificial reagent and will be discussed in more detail in the following section).

2.2.2 Experimental Water Splitting Systems

There are two main categories of experimental systems that can be used to accomplish these photochemical transformations [4, 5, 8–10]. The first of these, which was used by Fujishima and Honda in their work discussed above, uses two different electrodes for the water splitting half-reactions. The electrodes are placed in a photoelectrochemical (PEC) cell and connected through an external electrical circuit. The working electrode is typically constructed of a semiconductor deposited on a conductive substrate and this is connected electrically to a counter electrode (typically Pt), as illustrated in Figure 2.3. A reference electrode must also be employed in order to determine electric potentials on an absolute scale.

At this point it is worth making the distinction between n-type and p-type semiconductors. These designations refer to the "majority charge carrier" within the bulk of the semiconductor—n-type has majority negative charge carriers (electrons) in the bulk, while p-type has positive charge carriers (holes) as the majority carrier. This means that in water the opposite charge carrier migrates to the surface—holes migrate to the surface of an n-type semiconductor and electrons for p-type [11, 12]. Because of this, photo-electrodes for hole activated processes (e.g. oxygen evolution half-reaction or organic decomposition reactions) are constructed of n-type semiconductors. In contrast, photo-electrodes for electron driven processes (e.g. hydrogen

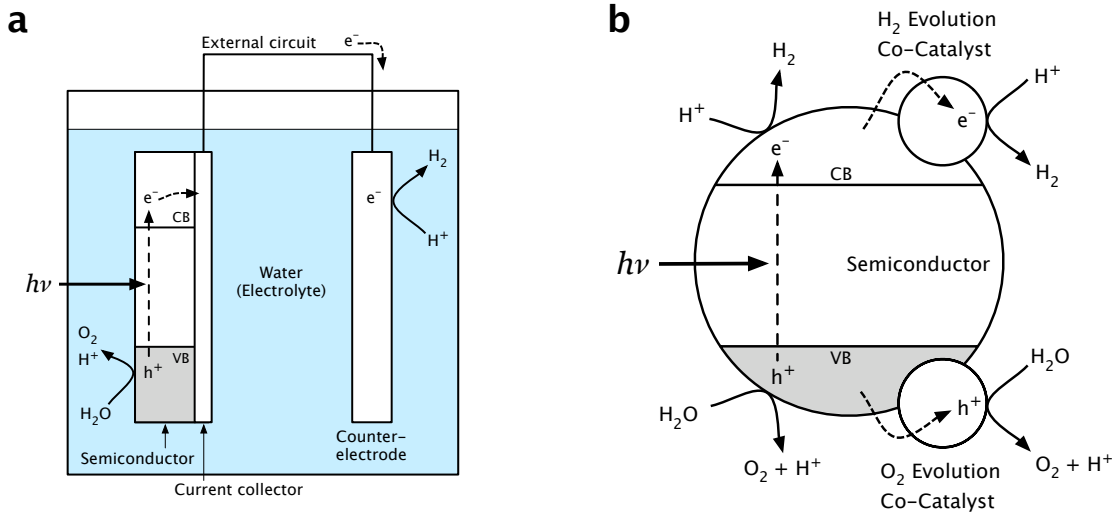

Figure 2.3: Schematic diagrams of two water splitting experimental systems. (a) Photoelectrochemical (PEC) cell system for production of H_2 and O_2 from water (processes for an n-type semiconductor are shown). When illuminated with photons of energy exceeding the band gap, excited charge carriers are formed in the semiconductor photoanode. The holes diffuse to the semiconductor surface and drive the oxygen evolution half-reaction ($2H_2O + 4h^+ \longrightarrow O_2 + 4H^+$). Electrons are collected and travel to the counter electrode where they drive the hydrogen evolution half-reaction ($2H^+ + 2e^- \longrightarrow H_2$). (b) Particle-based water splitting photocatalyst. Excited charge carriers (both electrons and holes) must diffuse to the particle surface where they drive the two half-reactions, usually at specially designed co-catalyst sites.

evolution half-reaction) are typically constructed of p-type semiconductors. In the experiments discussed in this document, and in many studies throughout the literature, n-type semiconductors are used to facilitate the oxygen evolution half-reaction and a metal counter electrode is employed for the hydrogen evolution half-reaction. The metal counter electrode is usually a simple Pt wire or foil—high surface area is not required because the hydrogen evolution reactions is very facile on Pt. The drawback is that Pt is very expensive, and because of a significant thrust in the literature is the development of less expensive p-type semiconductors that can be used in place of Pt for the hydrogen evolution half-reaction [13, 14].

Regardless of semiconductor type, illumination with light of the appropriate energy leads to the formation of charge carriers in the semiconductor. For an n-type semiconductor, energetic holes diffuse to the semiconductor/liquid interface where they participate in the oxygen evolution half-reaction. Energetic electrons move to the Pt counter electrode where they participate in the hydrogen evolution half-reaction. This experimental configuration has several benefits. If the PEC cell is designed appropriately, it is possible to separate H_2 and O_2 as they are evolved and forgo the need for costly downstream separation processes. The external electrical circuit allows application of a potential bias, which changes the electron energy by tuning the potential of the counter electrode [11]; for example, this is beneficial when the photo-excited electrons are not energetic enough to evolve H_2. Furthermore, measuring the photo-generated current (photocurrent) around the external circuit is a quick, easy method of determining the water splitting reaction rate, since two electrons must move from the semiconductor to the counter electrode for each molecule of water consumed. However, when using photocurrent as an analog of the water splitting reaction rate, one must be careful to ensure that the half-reactions occur-

ring at the electrodes are indeed the water splitting half-reactions, rather than the electrons and/or holes being consumed by another undesired electrochemical half-reaction [15–17]. This is typically accomplished by checking that gaseous H_2 and O_2 are evolved in the appropriate stoichiometric ratio, i.e. two moles of H_2 for each mole of O_2.

Alternatively, photo-catalysts that can perform both half-reactions on the surface of photocatalytic particles have also been identified. As discussed above, single-component photocatalysts are generally not able to meet all of the necessary requirements for overall water splitting. Therefore these systems typically require the addition of co-catalyst particles on the semiconductor surface. Charge carriers diffuse to the specially designed co-catalyst sites where they drive the two half-reactions. The co-catalyst acts to help separate the charge carriers and prevent recombination and to improve the kinetics of the hydrogen evolution half-reaction, the oxygen evolution half-reaction, or both. This is illustrated in Figure 2.3 and described in more detail later in this chapter. This configuration benefits from being experimentally simpler; however, it is not possible to measure photocurrent or adjust the electron energy with an external potential bias, so the semiconductor band positions must be positioned correctly with respect to the half-reaction potentials for overall water splitting.

In either experimental configuration it is common to see the use of sacrificial reagents (electron or hole scavenger) so that only one of the water splitting half-reactions occurs. This allows for the study of the individual half-reactions by ensuring that the overall rate is limited by the half-reaction in question. However, it is prudent to keep in mind that the overall water splitting process (without scavengers) on most semiconductor photocatalysts is typically limited by the rate of oxygen evolution

(particularly in the absence of an oxygen evolution co-catalyst) [9, 10].

2.2.3 Other Photocatalytic Reactions

Most of this dissertation focuses on the light-activated overall splitting of water to form H_2 and O_2; however, semiconductors are also useful for a wide range of organic decomposition (oxidation) reactions. These reactions are useful in the field of environmental remediation; for example, TiO_2 can be used to decompose organic pollutants in wastewater [18–26]. Another application is constructing self-cleaning surfaces. For example, studies have demonstrated that a thin coating of TiO_2 can catalyze the decomposition of airborne pollutants, meaning that the coated surface stays cleaner [27, 28]. While we mostly focus on the water splitting reaction throughout this document, we do also investigate organic decomposition as a test reaction in Chapter 4, so this class of reaction bears some discussion. The mechanics of charge carrier formation in the semiconductor are the same as previously discussed. However, there are two keys points that differentiate photocatalytic organic decomposition from photocatalytic water splitting.

The first major difference is that organic decomposition reactions are activated by the photo-generated holes at the semiconductor surface and the excited electrons are scavenged by oxygen (either in the surrounding air or more commonly dissolved in the aqueous reaction medium) [20, 21]. The resulting oxygen ions form OH radicals, which aid in the decomposition of the organic compounds. As such, the organic reactions are not two distinct and easily separable electrochemical half-reactions. Dissolved oxygen is a very efficient electron scavenger, almost regardless of the potential of the excited electrons, so external biasing is not necessary. The consequence of these attributes is that photocatalytic organic decomposition is not typically carried out in a PEC cell experimental system as described above in the context of water

splitting.

The second major difference, depicted in Figure 2.4, is that organic decomposition reactions are exothermic processes. The role of the photocatalyst is essentially to channel the energy of photons into activating the organic molecule, forming a radical, which then proceeds "downhill" in energy to the eventual complete mineralization products [20, 21, 29]. On the other hand, as previously mentioned, splitting water to form H_2 and O_2 is highly endothermic. Because of this it is often referred to as a photosynthetic reaction, in that the photo-catalyst has to effectively channel the energy of photons into synthesizing new, high-energy chemical bonds. In fact, at reasonable potentials each elementary step in the water splitting process is endothermic and requires the input of an energetic, photo-generated hole in order to proceed in the forward direction [30, 31]. Furthermore, all the water splitting elementary steps are reversible and, without the driving force supplied by the photo-generated holes, the elementary steps have a driving force to proceed in the reverse direction, toward reforming H_2O rather than producing H_2 and O_2. This is in stark contrast to the mechanism of organic decomposition. After activation by a photo-generated hole, the organic radical proceeds irreversibly in the forward direction without additional photon input [20, 21].

Even with these differences, organic decomposition reactions can provide a useful test reaction for evaluating photocatalytic activity of a semiconductor, as we will see in Chapter 4. There are a few reasons why experimentally one may want to investigate organic decomposition rather than water splitting. Chief among these is that if a dye molecule is chosen as the organic reactant, one can use quick and accurate spectroscopic techniques to measure the reactant concentration with time (provided that the dye's optical properties are chosen appropriately vis-à-vis the light

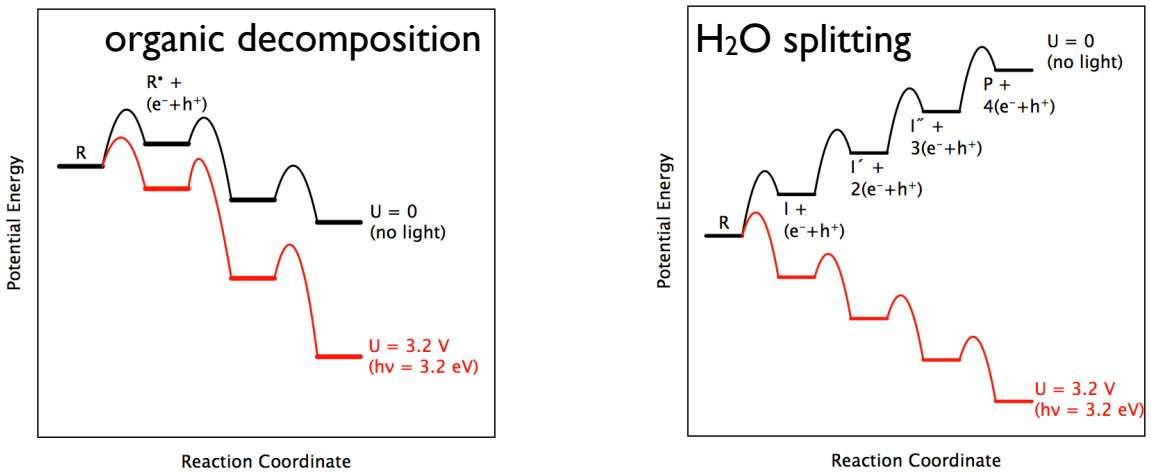

Figure 2.4: Schematic drawings depicting the approximate energy landscapes for a generic organic photo-decomposition reaction and photocatalytic water splitting. (a) Potential energy for a generic organic decomposition reaction (e.g. methylene blue decomposition) with no light (black curve) and light with photon energy of 3.2 eV (red curve). In the exothermic organic decomposition reaction, the photocatalyst serves to absorb photons and channel the energy into overcoming the activation barrier to formation of a radical species, which then spontaneously decays "downhill" in energy to complete mineralization (CO_2 + H_2O). (b) Potential energy for photocatalytic water splitting with no light (black curve) and light with photon energy of 3.2 eV (red curve). In water splitting, the photocatalyst must channel photon energy into overcoming the large thermodynamic barrier (∼237 kJ/mol) as well as significant activation barriers for each step of the water splitting process. Essentially, this means that a new photons is required to drive each reversible elementary step in the water splitting reaction pathway.

source, as discussed in detail in Chapter 4). This is an advantage compared to water splitting, where direct measurement of changes in species concentrations (minute changes in water concentration or minute amounts of evolved gasses) is difficult to measure accurately. However, the characteristics discussed in the paragraphs above do mean that there are significant differences between the two classes of reactions, and care must be taken to avoid making assumptions about the performance of a material for water splitting, for example, just because it performs well for decomposition of a particular organic molecule.

2.2.4 Desired Properties of a Photocatalyst

While the appeal of the direct conversion of solar into chemical energy has been recognized for a long time, commercial applications of these technologies are scarce. The only commercial scale projects remain limited to very specialized applications of photocatalytic organic decomposition, for example sun-activated self-cleaning surfaces [27, 28, 32], UV-light induced purification and sterilization applications [28, 33, 34], etc. Even these technologies are very limited in their size and scope.

The reason for the difficulty in wide-scale implementation of photocatalytic processes—particularly photosynthetic processes—is the stringent requirements on the photocatalysts themselves. As discussed above, the first basic requirements are that the semiconductor bands must be positioned appropriately in energy with respect to the electrochemical half-reactions. For water splitting, this means that the semiconductor valence band must have a potential more positive than 1.23 V versus NHE to activate the oxygen evolution half-reaction. In practice, the hole potential must be even more positive than 1.23 V versus NHE, usually closer to 1.6 V or more, because additional energy is required to overcome the kinetic barrier for the activation of the oxygen evolution reaction [10]; this additional required electric potential is typically

referred to as the "overpotential". The semiconductor conduction band must also have a potential more negative than 0 versus NHE. And of course implied by these two requirements is the fact that the semiconductor band gap must be larger than 1.23 eV. These requirements immediately eliminate some materials from consideration as single-component photocatalysts for overall water splitting. Amorphous Si, for example, is widely used in solar cells because of its small band gap of 1.1 eV (meaning that it absorbs a wide portion of the solar spectrum, light with wavelength of 1125 nm and below). However, this band gap is too low to drive the overall splitting of water. Another semiconductor, hematite (α-Fe_2O_3) has a wide enough band gap (2.3 eV) and absorbs a large portion of the solar spectrum (wavelengths below 540 nm). However, the conduction band of hematite has a potential of 0.5 V versus NHE, which means that a large electrical bias is necessary to give the photo-excited electrons enough energy to drive the hydrogen evolution reaction. Of course, balancing these considerations is the fact that the band gap should be as narrow as possible, in order to allow for the absorption of as much of the solar spectrum as possible. For example, ZrO_2 has conduction and valence bands positioned correctly with respect to the water splitting half-reaction potentials. However, the band gap of 5.0 eV is too wide, and only allows for the absorption of photons with wavelength less than 250 nm (the solar spectrum contains little radiation below 300 nm, see Figure 2.2).

In addition to these thermodynamic considerations, potential photocatalysts must also effectively deliver the photo-generated electrons and holes to the semiconductor/liquid junction, where the half-reactions are performed (e.g. the hole-driven oxygen evolution reaction). This is partly a consideration of the intrinsic majority charge carrier (i.e. n-type versus p-type, as discussed above). For n-type semicon-

ductors, holes will typically be the preferred surface species. Even so, most potential n-type photocatalysts suffer from a high rate of charge carrier recombination in the bulk before the holes can reach the surface [16, 35–37]. This is due to a discrepancy in the relatively high penetration depth of photons and the relatively low mean free path of charge carriers [36, 38]. The charge carrier mean free path is defined as the average distance charge carriers can diffuse before being consumed through recombination. Because the photon penetration depth is large, most charge carriers are formed in the semiconductor bulk [38]. The fact that the charge carrier mean free path is much smaller means that many charge carriers are lost to recombination before reaching the surface and driving the water splitting half-reactions. Efficient semiconductor photocatalysts must minimize this recombination rate and more effectively deliver charge carriers to the semiconductor/liquid junction. This will be a common theme throughout several sections of this dissertation, especially Chapter 5. Once charge carriers are delivered to the semiconductor surface, the surface must also possess high catalytic activity, i.e., have surface sites that allow for elementary chemical transformations associated with the half-reactions to be performed with small activation barriers (the overpotential must be minimal).

Potential materials must also be stable under water splitting conditions (i.e. under illumination, in water and sometimes subjected to an external electrical bias). CdS, for example, would appear to be an ideal water splitting photocatalyst based on Figure 2.2 alone. The conduction and valence bands are positioned appropriately with respect to the water splitting half-reactions and the band gap is fairly narrow (2.4 eV or 516 nm), which allows for absorption of a large portion of solar photons. However, when excited with energetic photons, CdS itself rather than H_2O is oxidized

by the resulting holes [4].

$$\mathrm{CdS} + 2\mathrm{h}^{+} \longrightarrow \mathrm{Cd}^{2+} + \mathrm{S} \tag{2.6}$$

The same is often true of other sulfide semiconductors [4]. Oxide semiconductors are typically more stable under water splitting conditions, since they are typically already in a high oxidation state [4]. However, even some oxide semiconductors, such as ZnO, suffer from photo-instability in water [4].

$$\mathrm{ZnO} + 2\mathrm{h}^{+} \longrightarrow \mathrm{Zn}^{2+} + 1/2\mathrm{O}_2 \tag{2.7}$$

From a stability and thermodynamic standpoint, Kudo et al. have suggested that the only viable single-component semiconductor materials are ZrO_2, $KTaO_3$, $SrTi_3$ and TiO_2 [4]. However, even these materials have shortcomings (e.g. co-catalysts are required to improve kinetics, band engineering is required to extend absorption range, etc.).

In addition to these numerous considerations, potential water splitting photocatalysts must be highly abundant and affordable, in order to ultimately facilitate the widespread production of large amounts solar fuels at reasonable cost. This favors materials such as TiO_2, Fe_2O_3, Si, etc., which have a very high natural abundance, and consequently are inexpensive. For example, the bulk price of TiO_2 is currently less than $\sim$1¢/lb and on the lab scale it can generally be obtained from suppliers such as Evonik/Degussa for free.

2.2.5 Common Photocatalyst Deficiencies

These required properties have made it very difficult to identify promising semiconductor photocatalysts, since most single-component materials do not satisfy all the requirements. An often-studied photocatalyst, hematite Fe_2O_3, is very appealing

due to its high earth abundance and narrow band gap (2.3 eV). However, hematite suffers a misaligned conduction band, as mentioned above, although this can be corrected by applying an external potential bias ($> 0.5V$) in exchange for an added efficiency loss. More troubling is the low mobility of charge carriers within the bulk of hematite and limited catalytic activity for both half-reactions [39–41]. Semiconductors that exhibit excellent mobility of charge carriers have been identified, such as Si [13, 14] and GaN [42]; however, in general these materials also exhibit poor catalytic activity for both half-reactions and may not have sufficient band gap energy (Si) and/or band alignment (GaN) for overall water splitting.

The most investigated semiconductor photo-catalyst is anatase phase TiO_2, because it meets many of the requirements—it is inexpensive and abundant, stable under water splitting conditions and the band positions are more-or-less properly aligned [12, 27, 28, 38, 43].[§] Because of these attributes, TiO_2 is often used as a benchmark semiconductor photocatalyst, and as such we will focus on it in this dissertation. The major drawback of anatase TiO_2 is its large band gap of 3.2 eV, which limits photo-absorption only to the UV region of the solar spectrum (i.e., photons in the visible region do not have enough energy to surmount the band gap). Since the UV region represents only $\sim$5% of solar spectrum, TiO_2 is not very efficient when sunlight is used to drive the reactions. This can be partially alleviated by doping TiO_2 with impurity elements such as nitrogen or carbon [44–50].

Even if these problems could all be surmounted in one material, rates of photocatalytic reactions under sunlight are inherently limited by the relatively diffuse nature of the solar flux. In a location such as Michigan, the solar flux is $\sim$ 125 mW/cm^2, which means that approximately 10^{17} solar photons impinge on a surface area of 1

[§]In practice, TiO_2 requires a small external potential in order to facilitate the H_2 evolution reaction because, under illumination, the conduction band potential may become slightly more positive than the H_2 evolution potential.

cm^2 each second. The result is that for a theoretical two-dimensional semiconductor surface only ∼100 solar photons collide with one surface atomic site (typical area of 10 $Å^2$) each second. This photo-impingement rate sets an upper bound on the maximum possible rate of photo-catalytic transformations. Since each mole of H_2 produced requires four photons, the maximum per site turnover frequency is 50 s^{-1}. For a conventional oxide semiconductor such as TiO_2, films on the order of a few micrometers are required to absorb a significant fraction of light [39, 51, 52]. If an equal probability for photon absorption is assigned for each site, for a 1 micrometer thick semiconductor film with 5-Å thick single layer, on average one charge carrier pair is formed on a site only ∼ every 20 seconds. This is extremely low, particularly for reactions, such as water splitting, where each elementary step is inherently endothermic, and there is high probability for reverse reactions.

These deficiencies, combined with the inherent semiconductor deficiencies discussed above, mean that reaction rates on semiconductors photocatalysts are exceedingly low. For example, a typical commercial thermo-catalytic process, currently used to make hydrogen form fossil or bio-renewable hydrocarbons, has a rate that is ∼100,000 times higher on a per active surface site basis than the rate of photocatalytic water splitting on a single-component homogeneous semiconductor film. This is depicted in Figure 2.5, which shows a typical turnover frequency (reaction rate normalized by the number of active sites) for a thermo-catalytic hydrogen production reaction (e.g. methane steam reforming), as compared to the approximate turnover frequency for a state-of-the-art TiO_2 water splitting photocatalyst. We note that these rates are normalized on a per active site basis. For a semiconductor photocatalyst, every site can theoretically be active for absorption of photons and transferal of the photo-generated charge carriers to drive the water splitting half-

reactions. In contrast, to minimize reactor volume a typical thermo-catalyst requires that the active metal sites are dispersed on a high surface area support material, such that the metal may only comprise less than 1% of the total mass. This means that it is not precisely equivalent to compare turnover frequencies on supported metals and bulk semiconductors and it may not be reasonable (or even necessary) to expect that semiconductor turnover frequencies should rival that of conventional catalysts. Nevertheless, the comparison shown in Figure 2.5 is instructive of the differences and challenges encountered when investigating semiconductor photocatalyst, particularly when approaching the field from the background of conventional heterogeneous catalysis.

As detailed above, the ideal maximum upper limit of the photocatalytic rate in Figure 2.5 is dictated by the number of solar photons available with energy exceeding 1.23 eV per surface cite, although realistically is it noted that 1.6–2.4 eV photons are generally needed to overcome kinetic overpotentials and concentration gradients at the semiconductor/liquid interface [10]. If using anatase TiO_2 as the photocatalyst (3.2 eV band gap), the number of photons available for reaction decreases dramatically; anatase absorbs only photons with wavelength greater than 387 nm, which equates to ∼4% of the solar spectrum. This decreases the maximum rate by a factor of 25. As discussed above, a single atomic layer of semiconductor is insufficient to absorb the solar flux, and typically a film on the order of one micron thick is required (∼2,000 atomic layers) [51, 52]. This requirement reduces the per site rate by an additional factor of 2,000. The remaining losses (a factor of ∼50–100) are due to the other semiconductor deficiencies discussed above, primarily the issue of loss of charge carriers due to bulk recombination. The practical significance of these low rates is that the required reactor size (i.e. land areas) and capital investment

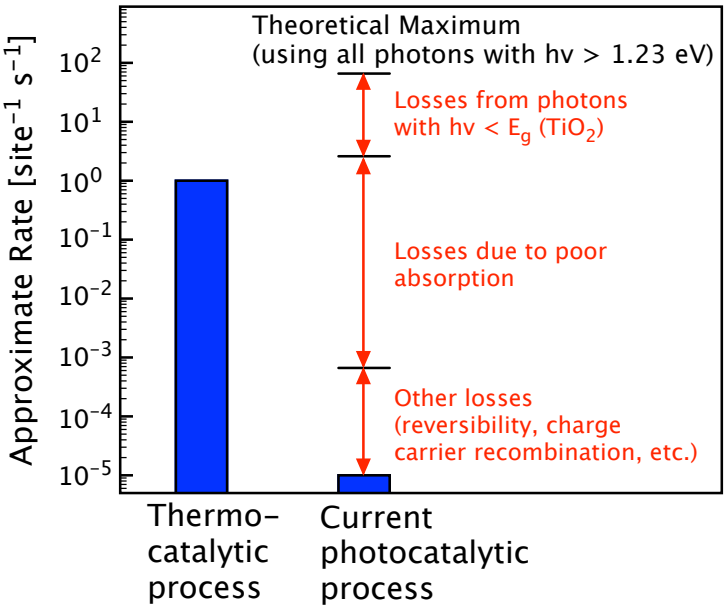

Figure 2.5: Approximate rates (turnover frequency) of H_2 production from current thermocatalytic and photocatalytic processes (via photocatalytic water splitting). The theoretical maximum photocatalytic rate is approximated by assuming a solar flux of 100 mW/cm^2, which corresponds to ∼100 photons per second per surface site with sufficient energy (exceeding the 1.23 eV required for water splitting). Four photons are required per reaction ($2H_2O + 4h\nu \longrightarrow 2H_2 + O_2$), which yields a maximum H_2 evolution rate of approximately 50 site^{-1}s^{-1}. Taking the case of anatase phase TiO_2 (3.2 eV band gap), only 4% of solar photons have energy exceeding the band gap, which lowers the rate to 2 site^{-1}s^{-1}. Complete absorption of the solar flux for a homogeneous semiconductor film requires a thickness on the order of a micrometer (∼2,000 atomic layers), which decreases the rate to approximately 0.001 site^{-1}s^{-1}. These losses due to poor absorption can be partially alleviated by employing more sophisticated semiconductor geometries, rather than homogenous films. The remaining losses are due to a combination of factors (primarily charge carrier recombination). Typical measured photocatalytic rates for homogeneous semiconductor films are on the order of 10^{-5} site^{-1}s^{-1}.

are prohibitively large for commercialization of any of the current technologies (we will briefly discuss issues of reactor design and economics in Chapter 7). Clearly, new directions are needed to design materials with higher photocatalytic activity for producing solar fuels using sunlight.

2.3 Recent Progress

As discussed above, identifying a semiconductor with high photocatalytic activity for water splitting has been complicated by the large set of strict requirements imposed upon them. Recent progress in identifying and synthesizing new materials has produced materials that meet some of these requirements [3, 4, 14, 42], but no single-component materials effectively meet all of the criteria. Earth-abundant oxides (e.g. TiO_2 and Fe_2O_3) have attracted the most attention as photocatalysts because of their high abundance, low cost, and stability under a wide range of conditions. However, there are several key problems that limit almost all oxide semiconductor photocatalysts, including the two mentioned. These specific problems were discussed in detail above and are effectively summarized by the following: (1) The kinetics of elementary surface transformation on semiconductors is generally quite slow. (2) Many semiconductors have a wide band gap, which limits what portion of the solar flux they can absorb. (3) The solar flux is inherently diffuse by nature. (4) Semiconductors generally exhibit a high rate of charge carrier recombination [35, 38]. This is due to the difference between the large penetration depth of photons into the oxide bulk and the short mean free paths of charge carriers. This means that a high percentage of charge carriers recombine in the oxide bulk before diffusing to the semiconductor surface [38]. The result is that the surface concentration of photo-generated charge carriers is generally quite low, and therefore rates of surface

reactions (e.g. the oxygen evolution half-reaction on a TiO_2 surface) are very low. Attempts to address this problem have typically involved manipulating the semiconductor morphology in order to improve photon absorption while minimizing the distance charge carriers must travel to reach the semiconductor/liquid interface—for example, quasi-one-dimensional morphologies such as nanotubes [13, 42, 53–62]. These structures improve photocatalytic activity because the electron transport down the length of the tube is increased in comparison with a collection of nanoparticles, while the distance holes must travel to reach the semiconductor/liquid interface is relatively small (the upper limit is half of the tube wall thickness).

2.3.1 Metal Co-catalysts

Another method of improving the photocatalytic activity of semiconductors is to decorate the surface of the semiconductor with a co-catalyst. These co-catalysts are typically very small particles of various metals (Ir [63], Ag [64], Au [63, 65–67], Pt [63], etc.) or metal oxides (RuO_2 [10], etc.). These metal or metal oxide co-catalyst particles do not directly interact with the source illumination, i.e. they have no photo-response upon illumination with the photon wavelength chosen for the experiments. Rather, the purpose of the co-catalyst particles is to provide more catalytically active surface sites in order to improve the kinetics of the half-reaction(s) performed at the semiconductor surface. Essentially, the semiconductor absorbs light and produces charge carriers, the photo-generated charge carriers in the semiconductor are then transferred into the co-catalyst particles, where the surface is designed and chosen to facilitate the desired half-reaction(s), see Figure 2.3b.

The common oxide semiconductors mentioned above are n-type materials, i.e. holes diffuse to the surface and drive the oxygen evolution reaction. Most oxide materials are inherently poor oxygen evolution catalysts; therefore, the addition of

a co-catalyst for the oxygen evolution reaction is particularly common [63–67]. For similar reasons, for p-type semiconductors (such as Si) the addition of a hydrogen evolution co-catalyst is common in literature [10, 14]. It is also possible to find reports of semiconductor photocatalysts with co-catalysts added for both the oxygen and hydrogen evolution half-reactions [4, 10]. This is usually only necessary when a particle-only system (as opposed to a PEC cell system) is used, since the metal counter electrode in a PEC cell typically facilitates the hydrogen evolution half-reaction with high rates.

Another consequence of the addition of metal particles to a photo-excited semiconductor is that recombination of charge carriers may be decreased. Addition of a metal to the surface of a semiconductor photocatalyst results in the formation of a Schottky junction, which for an n-type semiconductor allows the transfer of electrons from the semiconductor to the metal particles, but prevents electron transfer back across the Schottky barrier [10, 16, 43]. The result is that the metal co-catalyst helps to separate electrons and holes, increasing the effective lifetime of the charge carriers. Increased hole lifetime in the semiconductor can increase the rate of hole-driven processes, such the oxygen evolution half-reaction. If the energy of excited electrons transferred to the co-catalyst is sufficient, they can drive the hydrogen evolution half-reaction from the surface of the co-catalyst particle.

In the previous section we summarized four problems that limit almost all oxide semiconductor photocatalysts. This class of composite co-catalyst/semiconductor photocatalysts shows enhanced activity over that of a pure semiconductor, via improved kinetics of the surface chemical transformation(s). However, these materials do not address the other common problems discussed above. As discussed above, the metal co-catalyst nanoparticles in these systems are transparent to the light

used to excite the semiconductor. Very recently, it was discovered that additional enhancement of semiconductor photo-activity could be observed if the added metal nanoparticles are specifically tailored to exhibit a strong interaction with the source illumination [23, 24, 26, 41, 67–78]. The result is that both metal and semiconductor can be directly excited with incident photons, and through various interactions discussed below, the photo-activity of the composite can be enhanced, compared to the activity of the semiconductor alone. In these systems, the metal nanoparticles are characterized by their strong interaction with UV-visible photons through the excitation of surface plasmon resonance [79–82].

2.3.2 Plasmonic Metal Nanoparticles

Since light is simply an oscillating electromagnetic field, when exposed to photons, the surface electron density in a metal nanoparticle is collectively polarized in oscillating directions. This oscillation of surface electron density is referred to as a surface plasmon. The surface plasmon resonance (SPR) condition is met when the incident photon frequency matches the natural frequency of the surface electron density oscillating against the restoring force of the background field of positively charged nuclei. The wavelength (or frequency) of photons required for resonance is a function of the composition of the metal, the nanoparticle geometry (shape and size) and the dielectric constant of the surrounding medium [79–82].

Typically, gold, silver and copper nanoparticles have SPR within the UV-visible region of the electromagnetic spectrum, and hence these metals tend to be the most often discussed in the scope of solar illumination [83, 84]. This is shown in Figure 2.6a, which presents normalized experimental UV-visible extinction spectra for spherical nanoparticles of these three metals (consult the Characterization section of Chapter 3 for detailed experimental methods). The measured extinction is due

to two effects: (1) Under SPR conditions, the extinction is due to the excitation of surface plasmon (SP) states. These show up not as a single transition, but as a distribution of states, centered at approximately 410 nm for Ag, 510 nm for Au and 600 nm for Cu. (2) The high energy portions of the spectra, indicated with dashed lines in Figure 2.6a, are due to the excitation of interband transitions (i.e. promotion of d-band electrons to the sp-band) [85, 86]. This document focuses on the use of the SPR phenomenon primarily in Ag, which is dominated by the SPR in the UV-visible region. As such the interband transitions will not be discussed in much detail, although it is important to keep in mind for interpreting spectra and will be commented on a few times in subsequent chapters.

The wavelength and intensity of SPR for a given metal is also dependent on the shape and size of the nanoparticle, as this affects the spatial confinement of the electron oscillation [79–82]. For example, Figure 2.6b shows normalized experimental extinction spectra for Ag nanoparticles with wire, sphere and cube geometries. It is difficult to directly compare the SPR positions across geometries, but suffice it to say that this gives another method by which to change the SPR across the electromagnetic spectrum. It is interesting to note that cubes generally have the strongest interaction with light for a given particle volume, because the sharp corners essentially act to concentrate the surface plasmons, as discussed below. We also note that wires have two distinct modes (transverse and longitudinal), which depend on the orientation of the wire with respect to the incident photon polarization [82, 87]. This effect can be important in well-defined spectroscopic measurements, but it usually averaged out in randomly oriented samples such as shown in Figure 2.6b.

The effect of particle size is demonstrated in Figure 2.6c, which shows the normalized experimental extinction spectra for cubic Ag nanoparticles as a function of edge

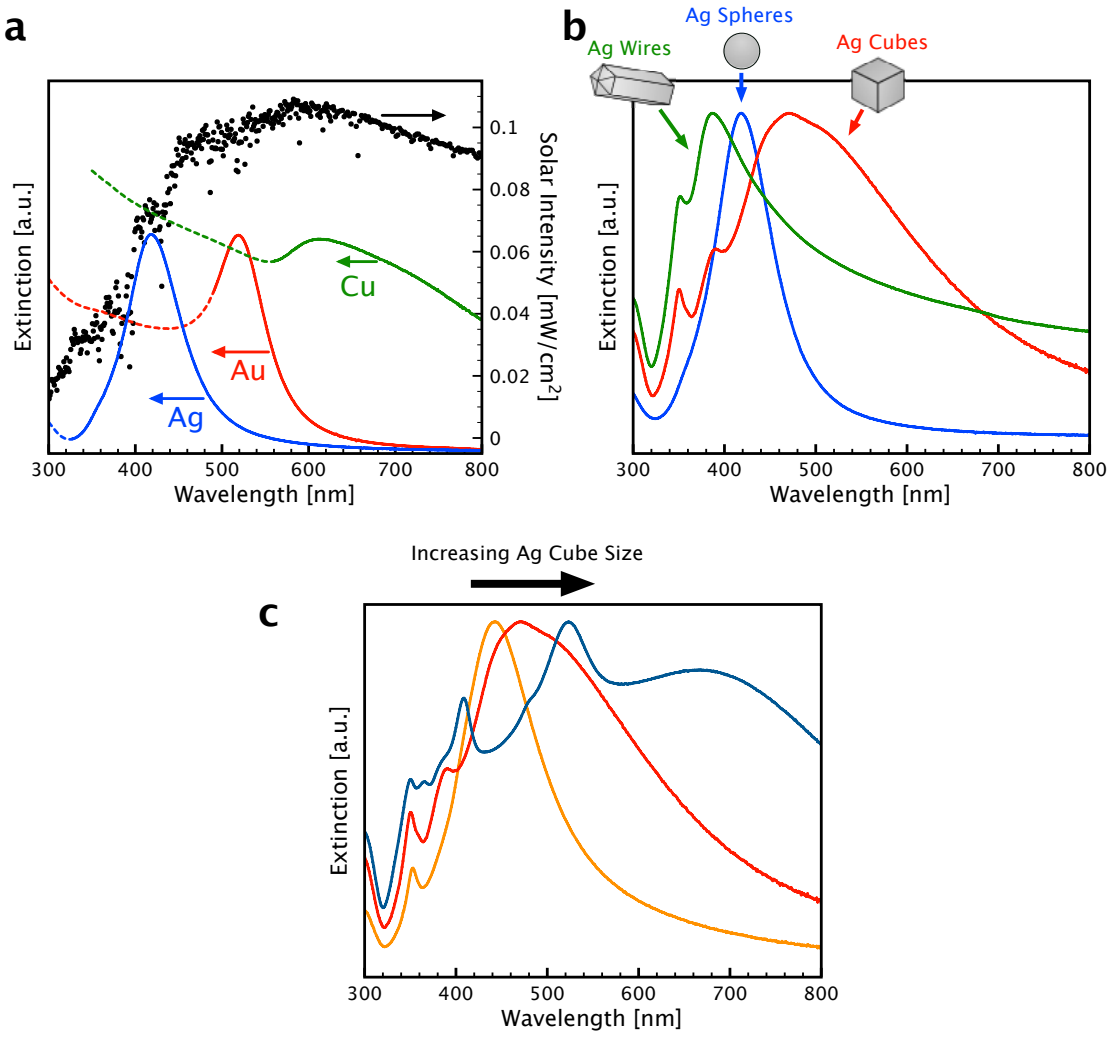

Figure 2.6: Metal plasmon resonance is a function of nanoparticle composition, shape and size. (a) Normalized experimental extinction spectra for spherical Ag, Au and Cu nanoparticles. Particle diameters are 38 ± 12 nm for Ag, 25 ± 5 nm for Au and 133 ± 23 nm for Cu. The dashed segments indicate regions dominated by interband transitions and solid segments indicate SPR. Black points show the intensity of AM1.5 solar illumination (National Renewable Energy Laboratory, http://rredc.nrel.gov/solar/spectra/am1.5/). (b) Normalized experimental extinction spectra for Ag spheres (38 ± 12 nm diameter), Ag cubes (79 ± 12 nm edge length) and Ag wires (90 ± 12 nm diameter and > 30 aspect ratio). (b) Normalized experimental extinction spectra for three sizes of Ag cubes (edge lengths of 56 ± 8 nm, 79 ± 13 nm and 129 ± 7 nm).

length. As the particles get smaller, the electrons are confined to a smaller area, increasing the natural frequency of the electron density oscillation and decreasing the SPR wavelength (increasing the energy of SPR) [79–82]. As shown collectively by Figure 2.6, changing the composition, size and shape of the metal nanoparticles allows us to tune the SPR across the entire UV-visible region of the spectrum, and beyond [84, 88]. We will return to this concept several times throughout this document, particularly in Chapter 4.

An interesting consequence is that the excitation of SPR on a metal nanoparticle is accompanied by a build-up of very intense oscillating electric fields in the neighborhood of the nanostructure [79–82]. These fields are essentially the consequence of the transfer of photon energy to surface plasmons, which are localized on the nanoparticle surface. Because they are confined near the surface of the nanoparticle, the intense fields are spatially non-homogeneous [82]. Figure 2.7 shows the results of a set of finite-difference time-domain (FDTD) optical simulations [89, 90], which accurate simulate the interaction of a metal nanostructure with incident light (see the Optical Simulations section of Chapter 3 for discussion of the simulation methodology). Figure 2.7a shows the spatial distribution of the SPR-induced enhancement in the electric field intensity[¶] around a cubic Ag nanoparticle with 75-nm edge length. Figure 2.7b shows the intensity of the field as a function of distance across the dashed line in Figure 2.7a. The figures show that the enhancement of the electric field intensity near the surface of the Ag particle is as high as a factor of 1,000 and drops with distance away from the particle approximately proportional to 1/distance. The field enhancements near two particles separated by 1 nm, where electron density can be even more tightly focused, can be as high as 10^6 or greater, as shown in Figures 7c

[¶]Electric field intensity is defined as the magnitude of the field squared. Enhancement in field intensity is defined as the field intensity at a point in space, normalized by the intensity of the flux of source photons.

and 7d (see also refs. [91, 92]). These spatially non-homogeneous field concentration and enhancement effects are generally referred to as "near-field" effects, in that they are localized effects and cannot be directly observed from a distant perspective (e.g. with a spectrometer).

Another important result of the SPR phenomenon is that plasmonic metal nanostructures are very good scatterers of light, particularly when the diameter or edge length of the particle is greater than approximately 50 nm [93, 94]. This means that when plasmonic metal particles are added to a host matrix, the average pathlength of photons through the structure is increased, with respect to the original material. This scattering phenomenon is typically referred to as a "far-field" effect, because the increased pathlength can directly be measured from a macroscopic viewpoint, i.e. by measuring the change in the far-field scattering and extinction spectrum of the matrix upon addition of plasmonic metal particles [95–97].

A third result of the plasmon resonance is that some energy of the SPR can be channeled into energizing lattice vibrations (phonons) in the metal particle (i.e. heating the particle), especially for particles much smaller than 50 nm [98–100]. However, an appreciable temperature increase (on the order of a degree Centigrade or more) under the most favorable conditions requires illumination with a light source several orders of magnitude more intense than sunlight [98–100]. This plasmon-heating phenomenon is useful in some applications, but will not be discussed in this document.

2.3.3 Plasmonic Metal/Semiconductor Composites

These unique aspects of plasmonic nanostructures make them useful for a variety of applications such as single-molecule spectroscopy [82, 101–103], drug delivery [104], solar cells [97] and others [105, 106]. Recently a few contributions have also suggested

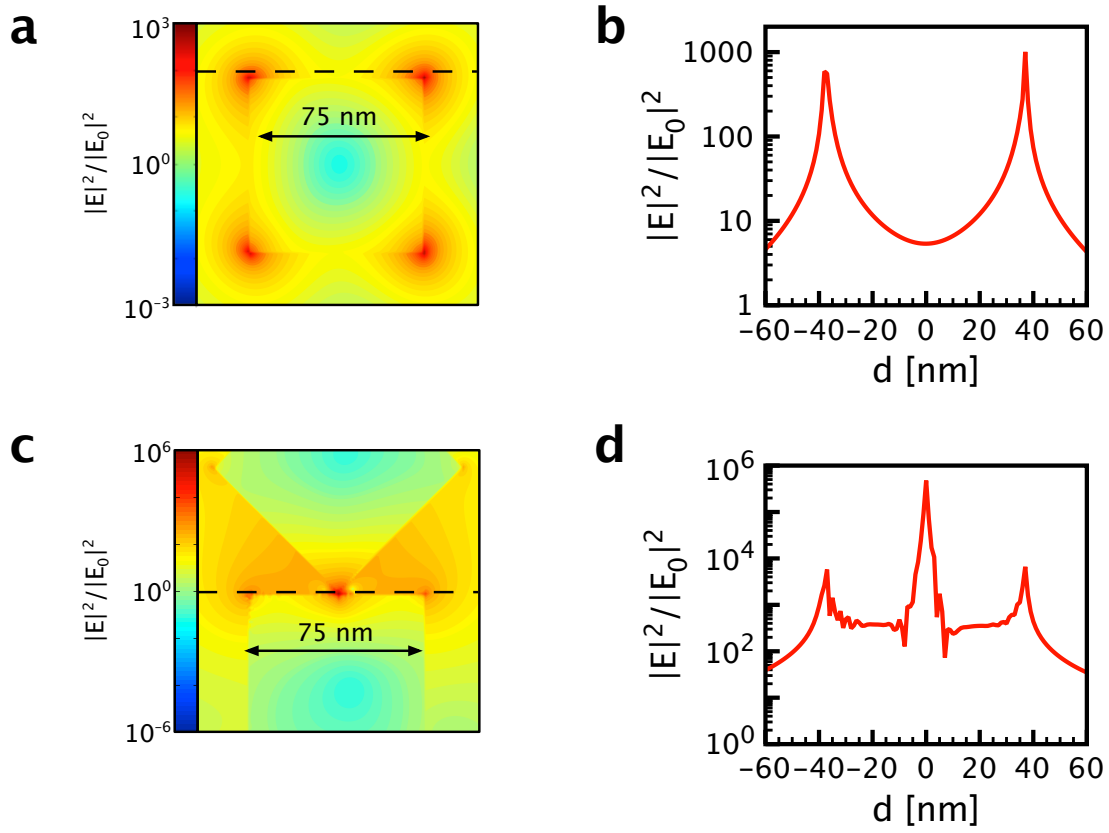

Figure 2.7: The excitation of metal SPR is accompanied by very intense, spatially non-homogeneous electric fields around the nanoparticle. (a) Spatial distribution of the SPR-induced enhancement of electric field intensity at the SPR peak wavelength (420 nm), calculated from an FDTD simulation, for 75-nm edge length Ag nanocube. (b) Enhancement in the electric field intensity in (a) as a function of distance along the dashed line indicated in (a). (c) Spatial distribution of the SPR-induced field intensity enhancement, from an FDTD simulation of two 75-nm Ag nanocubes separated by 1 nm (one cube is rotated 45°). (d) Enhancement in the electric field intensity in (c) as a function of distance along the dashed line indicated in (c).

that plasmonic nanostructures can be combined with conventional semiconductor photocatalysts to create composite materials with enhanced photo-activity [23, 24, 26, 41, 67–78]. Several mechanisms have been proposed, any or all of which could prove to be important under certain conditions and interpretation of results in the few publications has been difficult. With a few exceptions, mechanisms have been hypothesized, but not directly tested. In the following section we describe briefly the proposed enhancement mechanisms and in the following chapters we investigate the mechanisms in greater detail.

There are a number of physical interactions that are relevant to an analysis of composite plasmonic-metal/semiconductor systems under illumination and which will form the basis for the discussion of the results in later chapters:

(1) Charge transfer from the semiconductor to the metal, which separates electrons and holes and increases the lifetime of charge carriers [63–67]. This mechanism, discussed above in the context of co-catalysts, is independent of the metal SPR but could still play an important role.

(2) Transfer of electrons from the photo-excited metal to the semiconductor [67–69, 72], which increases the concentration of excited electrons in the semiconductor (this is similar to a dye sensitization mechanism [9, 107]).

(3) Far-field radiative transfer of energy from metal to semiconductor, due to an increase in the average photon pathlength ("scattering mechanism") [95–97]. Essentially, the presence of metal nanoparticles that interact with source photons act like "nano-mirrors", allowing some photons multiple passes through the system and effectively increasing the average photon pathlength.

(4) Near-field radiative transfer of energy from the SPR-induced intense electric fields near the surface of the metal nanoparticle (near-field electromagnetic mech-

anism") [26, 70, 71, 74, 75, 77]. Charge carrier formation in a semiconductor is proportional to the local electric field intensity ($|E|^2$) [108, 109]. Simulations of SPR-induced electric fields (as shown above) indicate greatly increased local electric fields. It has been hypothesized based on these simulations that the formation of charge carriers can be increased in the nearby semiconductor.

(5) As mentioned above, localized SPR-induced heating is another interesting phenomenon; however, it requires very high intensity light sources and even using optimal nanostructures is negligible under the solar flux [98–100], so we will not expound upon it here.

The relative predominance of each of these interactions will be a function of the properties of the system—both the properties of the individual building blocks (such as the metal SPR wavelengths and semiconductor absorbance) and also the meta-properties of the composite materials (for example, the geometric arrangement of the building blocks and the position of the metal SPR and semiconductor absorbance with respect to the wavelength of the light source). It is possible that in some systems multiple or even all of the mechanisms could play a role simultaneously.

These materials, which are a composite of conventional semiconductor paired with specially designed photo-excited metal nanostructures, have emerged only in the past few years as a promising new class of photocatalysts that show enhanced photo-activity compared to the semiconductor alone. The main goals of this dissertation is to demonstrate this new photocatalyst technology, to investigate the fundamental physical mechanisms underlying the activity enhancement and to use this mechanistic understanding to develop models and predictive tools that will guide the future design and optimization of these materials.

2.4 Conclusion

A brief introduction to photocatalytic transformations on semiconductors was presented. We focused on a discussion of the photocatalytic splitting of water to form H_2 and O_2 and photocatalytic organic decomposition reactions were also briefly discussed. A list of requirements for a semiconductor photocatalyst and the common deficiencies of many single-component materials was presented. We also discussed the addition of metal nanoparticles to a semiconductor. The traditional approach reported in literature is the addition of co-catalysts, where the co-catalysts do not directly interact with light, but serve to increase the semiconductor activity through a few effects. However, recently it has been demonstrated that the addition of photo-excited metal nanoparticles can enhance the semiconductor activity through a range of possible interaction mechanisms, each of which can contribute to enhancing the photo-activity under certain conditions. The discussion in this chapter summarizes the major proposed mechanisms and lays the groundwork for more rigorous investigation and analysis of the enhancement mechanisms presented in the chapters to follow.

References

[1] U.S. Department of Energy, *Annual Energy Outlook*; Technical Report, 2011.

[2] Gust, D.; Moore, T. A.; Moore, A. L. *Acc. Chem. Res.* **2009**, *42*, 1890–1898.

[3] Takata, T.; Tanaka, A.; Hara, M.; Kondo, J. N.; Domen, K. *Catal. Today* **1998**, *44*, 17–26.

[4] Kudo, A.; Miseki, Y. *Chem. Soc. Rev.* **2009**, *38*, 253–278.

[5] Fujishima, A.; Honda, K. *Nature* **1972**, *238*, 37–38.

[6] Nozik, A. J.; Memming, R. *J. Phys. Chem.* **1996**, *100*, 13061–13078.

[7] Serpone, N.; Pelizzetti, E. *Photocatalysis*; Wiley, New York, 1989.

[8] Bard, A. J.; Fox, M. A. *Acc. Chem. Res.* **1995**, *28*, 141–145.

[9] Grätzel, M. *Nature* **2001**, *414*, 338–344.

[10] Walter, M. G.; Warren, E. L.; McKone, J. R.; Boettcher, S. W.; Mi, Q.; Santori, E. A.; Lewis, N. S. *Chem. Rev.* **2010**, *110*, 6446–6473.

[11] Nozik, A. J. *Annu. Rev. Phys. Chem.* **1978**, *29*, 189–222.

[12] Linsebigler, A. L.; Lu, G.; Yates, Jr., J. T. *Chem. Rev.* **1995**, *95*, 735–758.

[13] Maiolo III, J. R.; Kayes, B. M.; Filler, M. A.; Putnam, M. C.; Kelzenberg, M. D.; Atwater, H. A.; Lewis, N. S. *J. Am. Chem. Soc.* **2007**, *129*, 12346–12347.

[14] Hou, Y.; Abrams, B. L.; Vesborg, P. C. K.; Björketun, M. E.; Herbst, K.; Bech, L.; Setti, A. M.; Damsgaard, C. D.; Pedersen, T.; Hansen, O.; Rossmeisl, J.; Dahl, S.; Nørskov, J. K.; Chorkendorff, I. *Nat. Mater.* **2011**.

[15] Ohtani, B. *Chem. Lett.* **2008**, *37*, 217–229.

[16] Ohtani, B. *J. Photochem. Photobio. C* **2010**, *11*, 157–178.

[17] Maschmeyer, T.; Che, M. *Angew. Chem. Int. Ed.* **2010**, *49*, 2–6.

[18] Yoneyama, H.; Takao, Y.; Tamura, H.; Bard, A. J. *J. Phys. Chem.* **1983**, *87*, 1417–1422.

[19] Anpo, M.; Chiba, K.; Tomonari, M.; Coluccia, S.; Che, M.; Fox, M. A. *Bull. Chem. Soc. Jpn.* **1991**, *64*, 543–551.

[20] Mills, A.; Wang, J. *J. Photochem. Photobio. A* **1999**, *127*, 123–134.

[21] Houas, A.; Lachheb, H.; Ksibi, M.; Elaloui, E.; Guillard, C.; Herrmann, J.-M. *Appl. Catal. B* **2001**, *31*, 145–157.

[22] Yan, X.; Ohno, T.; Nishijima, K.; Abe, R.; Ohtani, B. *Chem. Phys. Lett.* **2006**, *429*, 606–610.

[23] Zhou, X.; Hu, C.; Hu, X.; Peng, T.; Qu, J. *J. Phys. Chem. C* **2010**.

[24] Zhai, W.; Xue, S.; Zhu, A.; Luo, Y.; Tian, Y. *ChemCatChem* **2011**, *3*, 127–130.

[25] Tada, H.; Jin, Q.; Nishijima, H.; Fujishima, M.; Okuoka, S.; Hattori, T.; Sumida, Y.; Kobayashi, H. *Angew. Chem. Int. Ed.* **2011**, *50*, 3501–3505.

[26] Hou, W.; Liu, Z.; Pavaskar, P.; Hung, W. H.; Cronin, S. B. *J. Catal.* **2011**, *277*, 149–153.

[27] Fujishima, A.; Rao, T. N.; Tryk, D. A. *J. Photochem. Photobio. C* **2000**, *1*, 1–21.

[28] Fujishima, A.; Zhang, X.; Tryk, D. A. *Surf. Sci. Rep.* **2008**, *63*, 515–582.

[29] Kudo, A.; Kato, H.; Tsuji, I. *Chem. Lett.* **2004**, *33*, 1534–1539.

[30] Tang, J.; Durrant, J. R.; Klug, D. R. *J. Am. Chem. Soc.* **2008**, *130*, 13885–13891.

[31] Li, Y.-F.; Liu, Z.-P.; Liu, L.; Gao, W. *J. Am. Chem. Soc.* **2010**.

[32] Heller, A. *Acc. Chem. Res.* **1995**, *28*, 503–508.

[33] Kikuchi, Y.; Sunada, K.; Iyoda, T.; Hashimoto, K.; Fujishima, A. *J. Photochem. Photobio. A* **1997**, *106*, 51–56.

[34] Sunada, K.; Kikuchi, Y.; Hashimoto, K.; Fujishima, A. *Environ. Sci. Technol.* **1998**, *32*, 726–728.

[35] Lewis, N. S. *Acc. Chem. Res.* **1990**, *23*, 176–183.

[36] Zhang, Z.; Yates, Jr., J. T. *J. Phys. Chem. C* **2010**, *114*, 3098–3101.

[37] Ondersma, J. W.; Hamann, T. W. *J. Am. Chem. Soc.* **2011**.

[38] Yates, Jr., J. T. *Surf. Sci.* **2009**, *603*, 1605–1612.

[39] Cesar, I.; Kay, A.; Martinez, J. A. G.; Grätzel, M. *J. Am. Chem. Soc.* **2006**, *128*, 4582–4583.

[40] Cesar, I.; Sivula, K.; Kay, A.; Zboril, R.; Grätzel, M. *J. Phys. Chem. C* **2009**, *113*, 772–782.

[41] Thimsen, E.; Le Formal, F.; Grätzel, M.; Warren, S. C. *Nano Lett.* **2011**, *11*, 35–43.

[42] Goldberger, J.; He, R.; Zhang, Y.; Lee, S.; Yan, H.; Choi, H.-J.; Yang, P. *Nature* **2003**, *442*, 599–602.

[43] Henderson, M. A. *Surf. Sci. Rep.* **2011**.

[44] Sato, S. *Chem. Phys. Lett.* **1986**, *123*, 126–128.

[45] Asahi, R.; Morikawa, T.; Ohwaki, T.; Aoki, K.; Taga, Y. *Science* **2001**, *293*, 269–271.

[46] Kisch, H.; Macyk, W. *ChemPhysChem* **2002**, *3*, 399–400.

[47] Umebayashi, T.; Yamaki, T.; Itoh, H.; Asai, K. *Appl. Phys. Lett.* **2002**, *81*, 454–456.

[48] Lindgren, T.; Mwabora, J. M.; Avendaño, E.; Jonsson, J.; Hoel, A.; Granqvist, C.-G.; Lindquist, S.-E. *J. Phys. Chem. B* **2003**, *107*, 5709–5716.

[49] Irie, H.; Watanabe, Y.; Hashimoto, K. *J. Phys. Chem. B* **2003**, *107*, 5483–5486.

[50] Burda, C.; Lou, Y.; Chen, X.; Samia, A. C. S.; Stout, J.; Gole, J. L. *Nano Lett.* **2003**, *3*, 1049–1051.

[51] Tada, H.; Tanaka, M. *Langmuir* **1997**, *13*, 360–364.

[52] Hägglund, C.; Apell, S. P.; Kasemo, B. *Nano Lett.* **2010**, *10*, 3135–3141.

[53] Mor, G. K.; Shankar, K.; Paulose, M.; Varghese, O. K.; Grimes, C. A. *Nano Lett.* **2005**, *5*, 191–195.

[54] Paulose, M.; Shankar, K.; Yoriya, S.; Prakasam, H. E.; Varghese, O. K.; Mor, G. K.; Latempa, T. A.; Fitzgerald, A.; Grimes, C. A. *J. Phys. Chem. B* **2006**, *110*, 16179–16184.

[55] Prakasam, H. E.; Shankar, K.; Paulose, M.; Varghese, O. K.; Grimes, C. A. *J. Phys. Chem. C* **2007**, *111*, 7235–7241.

[56] Zhu, K.; Neale, N. R.; Miedaner, A.; Frank, A. J. *Nano Lett.* **2007**, *7*, 69–74.

[57] Grimes, C. A. *J. Mater. Chem.* **2007**, *17*, 1451–1457.

[58] Wei, Z.; Liu, Z.; Jiang, R.; Bian, C.; Huang, T.; Yu, A. *J. Solid State Electrochem.* **2010**, *14*, 1045–1050.

[59] Aurora, P.; Rhee, P.; Thompson, L. *J. Electrochem. Soc.* **2010**, *157*, K152–K155.

[60] Ranney, E.; Mansfield, J.; Sun, K.; Schwank, J. *J. Mater. Res.* **2010**, *25*, 89–95.

[61] Banerjee, S.; Mohapatra, S. K.; Misra, M. *J. Phys. Chem. C* **2011**.

[62] Roy, P.; Berger, S.; Schmuki, P. *Angew. Chem. Int. Ed.* **2011**, *50*, 2904–2940.

[63] Subramanian, V.; Wolf, E.; Kamat, P. V. *J. Phys. Chem. B* **2001**, *105*, 11439–11446.

[64] Arabatzis, I. M.; Stergiopoulos, T.; Bernard, M. C.; Labou, D.; Neophytides, S. G.; Falaras, P. *Appl. Catal. B* **2003**, *42*, 187–201.

[65] Subramanian, V.; Wolf, E. E.; Kamat, P. V. *J. Am. Chem. Soc.* **2004**, *126*, 4943–4950.

[66] Silva, C. G.; Juárez, R.; Marino, T.; Molinari, R.; García, H. *J. Am. Chem. Soc.* **2011**, *133*, 595–602.

[67] Primo, A.; Corma, A.; García, H. *Phys. Chem. Chem. Phys.* **2011**, *13*, 886–910.

[68] Tian, Z.-Q.; Ren, B. *Annu. Rev. Phys. Chem.* **2004**, *55*, 197–229.

[69] Tian, Y.; Tatsuma, T. *J. Am. Chem. Soc.* **2005**, *127*, 7632–7637.

[70] Awazu, K.; Fujimake, M.; Rockstuhl, C.; Tominaga, J.; Murakami, H.; Ohki, Y.; Yoshida, N.; Watanabe, T. *J. Am. Chem. Soc.* **2008**, *130*, 1676–1680.

[71] Christopher, P.; Ingram, D. B.; Linic, S. *J. Phys. Chem. C* **2010**, *114*, 9173–9177.

[72] Kowalska, E.; Abe, R.; Ohtani, B. *Chem. Comm.* **2009**, 241–243.

[73] Kowalska, E.; Mahaney, O. O. P.; Abe, R.; Ohtani, B. *Phys. Chem. Chem. Phys.* **2010**, *12*, 2344–2355.

[74] Kumar, M. K.; Krishnamoorthy, S.; Tan, L. K.; Chiam, S. Y.; Tripathy, S.; Gao, H. *ACS Catal.* **2011**, *1*, 300–308.

[75] Ingram, D. B.; Linic, S. *J. Am. Chem. Soc.* **2011**, *133*, 5202–5205.

[76] Chen, J.-J.; Wu, J. C. S.; Wu, P. C.; Tsai, D. P. *J. Phys. Chem. C* **2011**, *115*, 210–216.

[77] Liu, Z.; Hou, W.; Pavaskar, P.; Aykol, M.; Cronin, S. B. *Nano Lett.* **2011**, *11*, 1111–1116.

[78] Primo, A.; Marino, T.; Corma, A.; Molinari, R.; García, H. *J. Am. Chem. Soc.* **2011**.

[79] El-Sayed, M. A. *Acc. Chem. Res.* **2001**, *34*, 257–264.

[80] Burda, C.; Chen, X.; Narayanan, R.; El-Sayed, M. A. *Chem. Rev.* **2005**, *105*, 1025–1102.

[81] Kelly, K. L.; Coronado, E.; Zhao, L. L.; Schatz, G. C. *J. Phys. Chem. B* **2003**, *107*, 668–677.

[82] Brus, L. *Acc. Chem. Res.* **2008**, *41*, 1742–1749.

[83] Xia, Y.; Xiong, Y.; Lim, B.; Skrabalak, S. E. *Angew. Chem. Int. Ed.* **2009**, *48*, 60–103.

[84] Rycenga, M.; Cobley, C. M.; Zeng, J.; Li, W.; Moran, C. H.; Zhang, Q.; Qin, D.; Xia, Y. *Chem. Rev.* **2011**.

[85] Palik, E. D. *Handbook of Optical Constants of Solids*; Academic Press: New York, 1985.

[86] Pinchuk, A.; von Plessen, G.; Kreibig, U. *J. Phys. D: Appl. Phys.* **2004**, *37*, 3133–3139.

[87] Ming, T.; Zhao, L.; Yang, Z.; Chen, H.; Sun, L.; Wang, J.; Yan, C. *Nano Lett.* **2009**.

[88] Xia, X.; Oldman, R.; Catlow, R. *Chem. Mater.* **2009**, *21*, 3576–3585.

[89] Taflove, A.; Hagness, S. C. *Computational Electrodynamics: The Finite-Difference Time-Domain Method*; Artech House: Boston, 2005.

[90] McMahon, J. M. Ph.D. thesis, Northwestern University: Evanston, Illinois, 2010.

[91] Gunnarsson, L.; Rindzevicius, T.; Prikulis, J.; Kasemo, B.; Käll, M.; Zou, S.; Schatz, G. C. *J. Phys. Chem. B* **2005**, *109*, 1079–1087.

[92] Rycenga, M.; Xia, X.; Moran, C. H.; Zhou, F.; Qin, D.; Li, Z.-Y.; Xia, Y. *Angew. Chem. Int. Ed.* **2011**.

[93] Evanoff, D. D.; Chumanov, G. *J. Phys. Chem. B* **2004**, *108*, 13957–13962.

[94] Evanoff, D. D.; Chumanov, G. *ChemPhysChem* **2005**, *6*, 1221–1231.

[95] Derkacs, D.; Lim, S. H.; Matheu, P.; Mar, W.; Yu, E. T. *Appl. Phys. Lett.* **2006**, *89*, 093103.

[96] Pala, R. A.; White, J.; Barnard, E.; Liu, J.; Brongersma, M. L. *Adv. Mater.* **2009**, *21*, 1–6.

[97] Atwater, H. A.; Polman, A. *Nat. Mater.* **2010**, *9*, 205–213.

[98] Govorov, A. O.; Zhang, W.; Skeini, T.; Richardson, H.; Lee, J.; Kotov, N. A. *Nanoscale Res. Lett.* **2006**, *1*, 84–90.

[99] Hoepfner, M. P.; Roper, D. K. *J. of Anal. Cal.* **2009**, *98*, 197–202.

[100] Adleman, J. R.; Boyd, D. A.; Goodwin, D. G.; Psaltis, D. *Nano Lett.* **2009**.

[101] Jiang, J.; Bosnick, K.; Maillard, M.; Brus, L. *J. Phys. Chem. B* **2003**, *107*, 9964–9972.

[102] Nie, S.; Emory, S. R. *Science* **1997**, *275*, 1102–1106.

[103] Kühn, S.; Håkanson, U.; Rogobete, L.; Sandoghdar, V. *Phys. Rev. Lett.* **2006**, *97*, 017402–1–4.

[104] Jain, P. K.; Huang, X.; El-Sayed, I. H.; El-Sayed, M. A. *Acc. Chem. Res.* **2008**, *41*, 1578–1586.

[105] Larsson, E. M.; Langhammer, C.; Zorić, I.; Kasemo, B. *Science* **2009**.

[106] Schuller, J. A.; Barnard, E. S.; Cai, W.; Jun, Y. C.; White, J. S.; Brongersma, M. L. *Nat. Mater.* **2010**, *9*, 193–204.

[107] Youngblood, W. J.; Lee, S.-H. A.; Kobayashi, Y.; Hernandez-Pagan, E. A.; Hoertz, P. G.; Moore, T. A.; Moore, A. L.; Gust, D.; Mallouk, T. E. *J. Am. Chem. Soc.* **2009**, *131*, 926–927.

[108] Lee, J.; Javed, T.; Skeini, T.; Govorov, A. O.; Bryant, G. W.; Kotov, N. A. *Angew. Chem. Int. Ed.* **2006**, *45*, 4819–4823.

[109] Anger, P.; Bharadwaj, P.; Novotny, L. *Phys. Rev. Lett.* **2006**, *96*, 113002–1–4.

CHAPTER 3

Synthesis, Experimental and Computational Methods

3.1 Summary

Frequently used synthesis, preparation, characterization and computational methods are explained in detail. The subsequent chapters in the document explain some methods specific to experiments within those sections and also refer back to sections within this chapter. Synthesis methods are presented first, followed by thorough descriptions of preparation methods for samples used in each chapter. This is followed by descriptions of commonly used characterization techniques. Experimental details for measuring photo-catalytic activity for samples are discussed on a chapter-by-chapter basis. Finally, a detailed description of optical simulation methodology is presented.

3.2 Synthesis Methods

The metal nanoparticle synthesis methods are outlined below. For more details, please consult the publications referenced below. The metal nanoparticle synthesis methods are followed by detailed descriptions of the synthesis and preparation of semiconductors used in the experiments.

3.2.1 Plasmonic Metal Nanoparticles

In general, metal nanoparticles are synthesized by reduction of a metal salt precursor (typically $AgNO_3$ or $AuCl_4$) [1–3]. A reducing agent (reductant) is used to reduce the metal ion within the metal salt to its metallic state. The choice of reductant (ethylene glycol, sodium citrate, sodium borohydride, etc.) is one of many influences on the resulting particle shape and size. Another key reagent is the choice of stabilizer (or capping agent), which is designed to bind to the surface of the nanoparticles after they have formed, and provide favorable interactions with the surrounding solvent to prevent particle agglomeration and settling. The choice of stabilizer is influenced by the reductant and solvent used during the synthesis, as well as the desired solvent to be used for long-term storage of the colloidal solution. Spherical particles are the preferred geometry, because this shape minimizes the surface free energy [2]. Deviation from spherical nanoparticles (see below) requires additional reagents to direct the nanoparticle growth. The metal nanoparticle synthesis techniques used herein fall under the general category of polyol synthesis techniques. The advantages of the polyol synthesis are that nanoparticle yields per batch are relatively high, it is possible to direct the growth of Ag structures into cubes using an etchant (see below), and the polymeric stabilizer used allows for long-term storage of nanoparticles in water, ethanol or ethylene glycol [2–5].

Ag nanocubes were prepared using a modified polyol synthesis procedure [1, 4, 6]. This method involves slow addition of $AgNO_3$ (precursor) and polyvinylpyrrolidone (stabilizer) to a solution of ethylene glycol (solvent and reductant) and dilute HCl (etchant). A vial containing 5 mL of ethylene glycol was to 140 °C for 1 hour in an oil bath; after this initial hour the vial remains in the oil bath and held at 140 °C for the duration of the synthesis described below. The vial contained a magnetic

stir bar and a cap was loosely placed on top (to allow the escape of any vapors from contaminant in the glycol). The vial and stir bar must be very clean (used vials were discarded after synthesis and a new vial was used for each batch; stir bars were cleaned thoroughly each time with piranha solution). A 60-L solution of 30 mM HCl in ethylene glycol was prepared and added to the hot ethylene glycol solutions and allowed to mix for 10 minutes. Two solutions were then added simultaneously to the heated vial of ethylene glycol using a syringe pump at a rate of 0.75 mL/min. The first of these was 3 mL of a 0.1 M solution of $AgNO_3$ in ethylene glycol. The second solution was 3 mL of 0.15 M polyvinylpyrrolidone (PVP) in ethylene glycol (PVP molecular weight was 55,000). After addition of these two solutions the cap was replaced loosely onto the top of the vial. The solution was maintained at 140 °C in the oil bath for approximately 24 hours. Changing this reaction time allowed for control of the final particle size distribution. Essentially, dissolved oxygen also acts as an etchant, and the size of the resulting particles is mostly dictated by the length of time the reactant mixture is exposed to air and the concentration of HCl. After this reaction period, the vial cap was then closed completely to prevent the influx of air. Over the next few hours the solution changed from clear and colorless to an opaque and tan in color. PVP binds selectively to the (100) facet of the seed crystals and HCl acts to etch away the (111) facets. As (100) sites are exposed more PVP binds. The result was cubic Ag nanoparticles fully capped with a layer of polyvinylpyrrolidone (PVP) stabilizer on the surface to prevent agglomeration. The particles were washed with acetone once via centrifugation and re-dispersed in 200-proof ethanol, which did not significantly remove the PVP from the surface.

Two Ag cube samples were used throughout the experiments detailed in the following chapters, one with average edge length of 118 nm (Chapters 4 and 5) and the

other with 80-nm edge length (Chapter 6). Particle size distributions were determined from scanning electron microscopy (SEM), by applying the colloidal solutions to Si wafer fragments, taking several SEM images and measuring particles. A representative SEM image of the 118-nm Ag cube sample is shown in Figure 3.1a. Micrographs were obtained using an FEI Nova 200 Nanolab at the University of Michigan Electron Microbeam Analysis Laboratory (EMAL); the accelerating voltage was 5 kV. Metal nanoparticle samples were also characterized by UV-visible spectroscopy (see the Spectroscopy section below); an extinction spectrum is shown in Figure 3.1b. The major spectral features shown in Figure 3.1b are a consequence of the excitation of the Ag surface plasmon resonance (SPR), discussed in Chapter 2. At wavelengths below ∼325 nm, the extinction is due to the excitation of interband transitions in Ag (i.e. d-band to sp-band electronic transitions) [7, 8].

Spherical Au particles were synthesized in a process similar to that discussed above Ag cubes, the main differences were that (1) $AgNO_3$ was replaced with $AuCl_4$, (2) HCl was not added to etch the seed crystals and (3) the metal salt and PVP solutions were added quickly [3–5]. Specifically, a 5-mL vial of ethylene glycol was heated to 160 °C in an oil bath. Two solutions were prepared: a 3-mL solution of 0.05 M $AuCl_4$ in ethylene glycol solution and a 3-mL solution of 0.6 M PVP in ethylene glycol. Both of these solutions were added quickly to the heated ethylene glycol and the heated vial was then capped tightly. The solution was allowed to react for one hour at 160 °C, after which time it was removed from the heat. The result was spherical Au nanoparticles coated with PVP. Size could be controlled by changing the $AuCl_4$ and PVP concentrations. The particles were washed with acetone once via centrifugation and re-dispersed in 200-proof ethanol, which did not significantly remove the PVP from the surface.

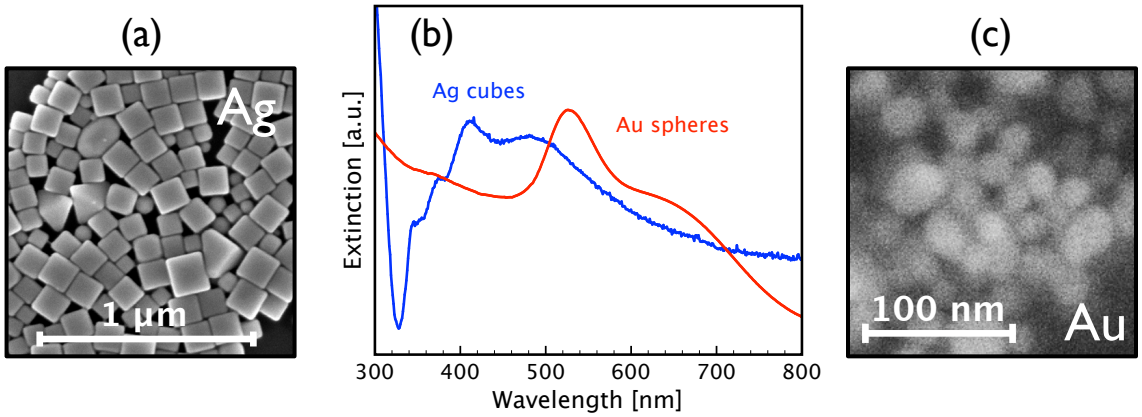

Figure 3.1: Characterization of cubic Ag nanoparticles and spherical Au nanoparticles. (a) Scanning electron microscopy (SEM) image of cubic Ag nanoparticles with edge length of 118 ± 25 nm. (b) UV-visible extinction spectra of cubic Ag nanoparticles and spherical Au particles. The extinction below 325 nm for Ag and below ~500 nm for Au is due to interband transitions. The main extinction features at higher wavelengths are due to the excitation of the metal surface plasmon resonance. (c) SEM image of spherical Au nanoparticles with diameter of 25.4 ± 4.5 nm.

The resulting Au spheres were 24.5 ± 4.5 nm in diameter as determined by SEM (Figure 3.1c). Figure 3.1b shows a UV-visible extinction spectrum for the spherical Au nanoparticles. The extinction peak around 550 nm is a consequence of the excitation of the Au SPR, as discussed in Chapter 2. At wavelengths below ∼500 nm, the Au extinction is due to the excitation of interband transitions [7, 8]. The main difference between Au and the Ag particles discussed above is that the Au SPR occurs only at wavelengths above ∼500 nm. As discussed more below and in subsequent chapters, this Au SPR does not overlap with the semiconductors used in experiments; because of this they were used as an important control in experiments testing the interaction of the SPR with a semiconductor.

3.2.2 Nano-particulate TiO_2 and N-TiO_2

The non-doped TiO_2 (sometimes called native TiO_2) used for experiments was as-purchased P25 TiO_2 from Evonik Industries, unless otherwise noted. P25 is the industrial standard non-porous nano-particulate TiO_2, and is often colloquially referred to as "Degussa P25" because it was manufactured by Degussa AG until that company's acquisition by Evonik in 2006. The average particle size is approximately 22 nm and the composition is approximately 80% anatase phase and 20% rutile phase. The only place where a different TiO_2 material was used was in Chapter 7, where sol-gel materials are briefly used (see the next section).

Nitrogen-doped TiO_2 (N-TiO_2) was synthesized by heating P25 TiO_2 particles in flowing gaseous NH_3 [9]. The P25 TiO_2 was packed in a quartz reactor (1-inch diameter tube containing approximately 5 grams TiO_2) and placed vertically in a tube furnace. Glass wool was placed on both sides of the P25 bed, in order to keep the fine powder stationary in the tube. A flow of gaseous NH_3 was initiated and held at 50 mL/min at room temperature for one hour. NH_3 flow was then increased

to 200 mL/min and the temperature was increased from ambient to 500° C with a ramp rate of 10 °C/hour. The temperature was then held at 500 °C for 5 hours, after which time the reactor was cooled to room temperature at a rate of ∼20 °C/min while maintaining flow an NH_3 flow of 200 mL/min. Once the reactor reached room temperature, NH_3 flow was stopped and the reactor was purged with air or nitrogen for a few minutes to ensure no residual noxious fumes would be encountered upon removal of the reactor tube.

The resulting N-TiO_2 powder, after cooling, had a light yellow color, meaning the material absorbs some blue light. This is quantified by Figure 3.2a, which shows a diffuse reflectance UV-visible spectrum of N-TiO_2 and as-purchased P25 TiO_2. A Raman spectrum of the synthesized N-TiO_2, shown in Figure 3.2b, was indistinguishable from that of as-purchased P25 TiO_2, indicating no significant change in the percent anatase/rutile. Preliminary X-Ray Diffraction (XRD) analysis was inconclusive, but we note that this data has been widely reported in the literature for this and other similar synthesis methods [9–12].

3.2.3 Sol-gel TiO_2

As discussed in Chapter 7, nano-particulate semiconductor photocatalysts often exhibit very low efficiencies because of poor electron diffusion to the current collector. One method of improving this problem is by using meso-porous photocatalyst films. Meso-porous TiO_2 films were synthesized using a sol-gel method, which is essentially the controlled hydrolysis of a precursor compound [13].

396 mL of de-ionized water was transferred to a 500 mL (or larger) beaker or flask. A Teflon-coated magnetic stir bar was added and liquid was stirred vigorously. 4 mL of 1.0 M nitric acid (HNO3) were added. 10 mL of titanium isopropoxide was diluted with 90 mL 2-propanol and transferred to a plastic syringe. Using a

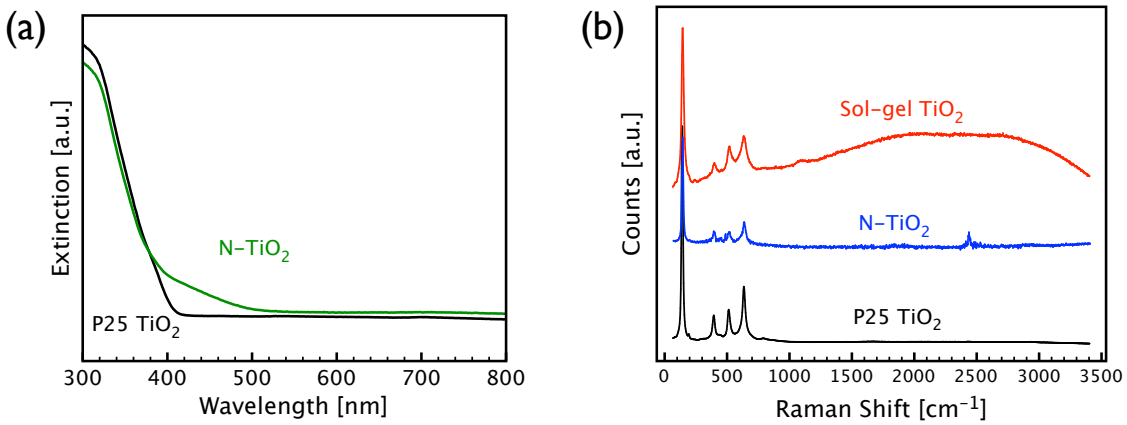

Figure 3.2: Characterization of P25 TiO_2, sol-gel TiO_2 and nitrogen-doped TiO_2. (a) UV-visible extinction spectra of as-purchased P25 TiO_2 and synthesized nitrogen-doped TiO_2 (N-TiO_2). (b) Raman spectra of as-purchased P25 TiO_2, synthesized nitrogen-doped TiO_2 (N-TiO_2) and synthesized sol-gel TiO_2. The spectra are arbitrarily offset vertically to allow for comparison.

syringe pump, the titanium isopropoxide solution was added to the stirred aqueous solution at a rate of 0.5 mL/min. After addition of the titanium isopropoxide, the solution appeared opaque and white. The solution was capped or covered and stirred at room temperature for 12 hours. After this period, the resulting colloidal solution could be stored in a sealed container almost indefinitely. After several weeks without stirring, a white precipitate sometimes formed on the bottom of the storage vessel, but vigorous stirring, agitation or sonication successfully re-dispersed the solids.

It is worth noting that at this point the solution does not contain crystalline TiO_2. To effectively use the photocatalyst it must be coated onto a substrate, dried then calcined in air at a temperature of at least 400 °C for at least 4 hours. Raman spectra of the sol-gel TiO_2 before calcination showed no discernible features, while Raman spectra after calcination (Figure 3.2b) indicates anatase phase TiO_2. We note that this method also allows for the production of meso-porous nitrogen-doped TiO_2 films, although these were not used in any experiments reported in this document. N-TiO_2 sol-gel films could be produced using the same method described above, but with the addition of NH_4OH to the initial de-ionized water vessel, resulting in a final NH_4OH concentration of 1.0 M. The resulting sol-gel was visibly indistinguishable from the non-doped synthesis; however, upon calcination the resulting N-TiO_2 films had the expected light yellow color.

3.3 Sample Preparation Methods

Composite photocatalysts used throughout the experiments in this dissertation were simple physical mixtures of metal and semiconductor nanoparticles. The specific methods used to prepare these photocatalysts are described in the following sections. In general, all of the nanoparticles were suspended in ethanol, then mixed

to create composite suspensions. Using ethanol as the solvent was important. Water could not be used because its surface tension is too high and it did not properly wet the substrates, which caused uneven drying and sometimes led to solids flaking off when submerged in water. Acetone could not be used, as PVP-capped metal nanoparticles are not stable in it—they instantly "crash out" of solution and form a black precipitate.

3.3.1 Organic Decomposition Photocatalysts (Chapter 4)

Semiconductor (TiO_2 and N-TiO_2) and metal (Ag and Au) nanoparticles were independently suspended in pure ethanol and sonicated. Semiconductor suspensions were typically 1 g semiconductor particles to 99 g pure 200-proof ethanol. Metal nanoparticle samples were ∼25 mg per mL of ethanol. Single-component samples (for example, TiO_2-only or Ag-only) were prepared by drop-coating these suspensions onto 1-cm^2 SiO_2 substrates and drying in a stagnant ambient atmosphere. For the purposes of this document, drop-coating means applying a solution to a substrate using a micropipette. Aliquots of no more than 100 L per square centimeter seemed to produce the best results (i.e. the most consistent homogeneous films). If thicker films were required, which was generally the case, multiple drop-coating cycles were performed, with sufficient time in between to ensure that all ethanol had evaporated. The total weight of films was determined by knowing the density of solids in each solution and simply tracking the total volume of solution applied to a substrate. For semiconductors, the amount of solids in a solution was determined by drying a known volume of the solution (several mL) and weighing the resulting solids. For metal particles, it was not expedient to waste this much of a nanoparticle solution, so a known volume of the solution (∼10 L) was applied to a fragment of Si wafer. Ten SEM images were then taken from different spots on the wafer, particles were

measured and counted, and the total mass of the Ag particles was estimated.

Composite suspensions were prepared by combining the pure nanoparticle suspensions and thoroughly mixing using agitation and sonication. Weight percent of the two constituents was determined by first determining the solids density of each individual solution and then simply tracking the mixing ratios. The amount of metal nanoparticles in the various experiments was varied and has been indicated in the respective chapters. Composite photocatalyst samples (for example, Ag/TiO_2) were prepared by the same drop-coating method using the mixed nanoparticle suspensions, resulting in a physical mixture of the two types of particles on the substrate. All photocatalysts samples used in the experiments contained constant weight (as well volume and surface area) of semiconductor particles. Figure 3.3a shows UV-visible extinction spectra measured in diffuse reflectance mode (see the Spectroscopy section below).

3.3.2 Water Splitting Photoelectrodes (Chapter 5)

The N-TiO_2 powder was suspended in 200-proof ethanol (EtOH) at a ratio of 99 g EtOH per gram of N-TiO_2; the solution was sonicated for one hour. Composite solutions were prepared by mixing the Ag nanocube colloidal solution or Au nanosphere solution with the N-TiO_2 in ethanol mixture and sonicating again for one hour. Composites were 5% metal by weight in both cases for all of the water splitting experiments. The samples were prepared by drop-coating the nanoparticle solution onto 1-in^2 conductive substrates (glass coated with indium tin oxide) with a micropipette; the samples were allowed to dry in a stagnant atmosphere. It was observed that the stagnant atmosphere was necessary to produce consistent, reasonable homogeneous films. It seems that if uncovered the substrates dried too quickly, which caused large-scale agglomeration of solids that sometimes resulted in some of

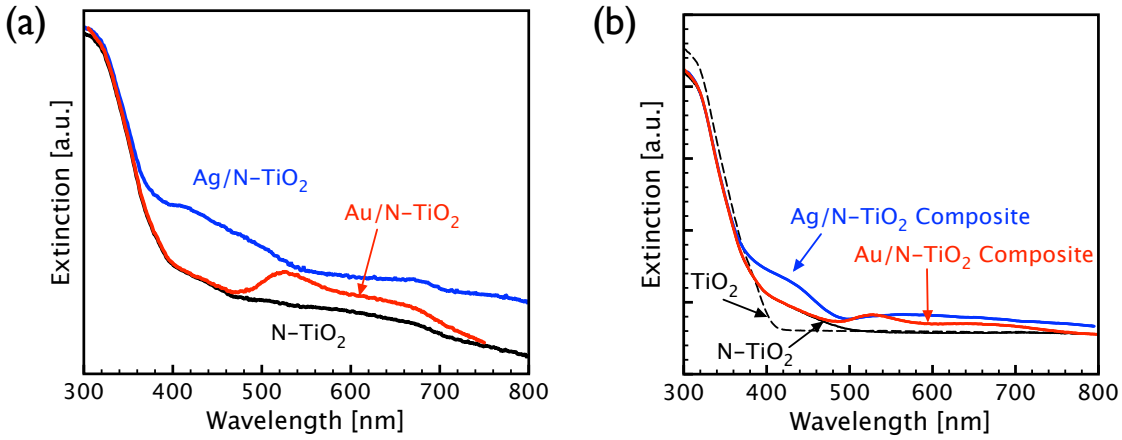

Figure 3.3: UV-visible extinction spectra for composite samples used in Chapters 4 and 5. (a) UV-visible extinction spectra for N-TiO_2-only, Ag cube/N-TiO_2 composite and Au sphere/N-TiO_2 composite photocatalysts, used in the methylene blue decomposition experiments in Chapter 4. (b) UV-visible extinction spectra for TiO_2-only, N-TiO_2-only, Ag cube/N-TiO_2 composite and Au sphere/N-TiO_2 composite photo-electrodes, used in the water splitting experiments in Chapter 5.

the material flaking off of the substrate when submersed in water. The resulting photo-electrode films were ∼0.75 μm thick (measured by ellipsometry). All samples contained 2 mg N-TiO_2 (constant semiconductor weight, volume, surface area). Figure 3.3b shows UV-visible extinction spectra (diffuse reflectance mode) of the samples.

3.3.3 Photo-electrodes for Distance Dependence Studies (Chapter 6)

For the distance dependence studies presented in Chapter 6, the preparation methods discussed above were insufficient. Essentially, drop coating multiple layers of different nanoparticle suspensions did not produce samples that were consistent or uniform in thickness. Instead, samples were prepared by spin coating successive layers of the constituent materials onto an inert transparent conductive support (fluorine-doped tin oxide (FTO)). Spin coating is a process by which the substrate is affixed to a plate that spins at a constant and controllable rate (a constant rate of 4,000 rpm was used in all of the steps discussed below). The suspension is then dropped onto the spinning substrate with a micropipette, as before. This produces much more uniform and consistent samples compared to the drop coating method discussed. The main drawback of spin coating is that, even at low spinning speeds, most of the applied solution spins off of the substrate and thus is wasted.

For the photocatalyst electrodes used in Chapter 6, the first step was spin coating a suspension of semiconductor particles (TiO_2 or N-TiO_2 in ethanol) on the FTO support. The semiconductor particles were suspended in pure (200 proof) ethanol at a ratio of 99 g ethanol to each gram of semiconductor (the semiconductor suspensions were sonicated for at least 15 minutes prior to each use). The weight of semiconductor particles was constant for each sample. A dilute solution of polyethylene glycol (PEG) in ethanol (2.5% PEG by weight) was then applied on top of the semicon-

ductor via spin coating. The thickness of the PEG layer was varied by changing the volume of PEG solution applied. Finally, a constant volume of Ag nanocube suspension in ethanol was applied on top via spin coating. A UV-visible extinction spectrum of one of the finished composite samples is shown in Figure 3.4. The figure also shows a schematic of the composite sample geometry.

The thickness of the spacer layer was estimated by applying the same volumes of PEG solution to a clean Si wafer with the same area as the FTO support, and measuring the resulting PEG thickness using ellipsometry, as shown in Figure 3.4a. Ellipsometry is an optical technique that can be used to analyze thin films by observing the change in the polarization of light that is reflected off of the sample. Measurements were performed using a J. A. Woollam BASE-160 ellipsometer with EC-270 control module. Fitting the measured spectra with a model comprising a 1 micron thick layer of Si and a variable-thickness PEG layer (refractive index of $\sim$1.4) allowed the estimation of the thickness of the PEG layer. The Si substrate was necessary because the ellipsometry technique relies on transmission through a very thin sample and then reflection off of the underlying substrate.

3.4 Characterization Methods

The following sections describe two important characterization techniques used throughout the following chapters. As described below, these two spectrophotometry techniques help determine how a material interacts with light, which is important for predicting and analyzing the observed photo-catalytic activity.

3.4.1 UV-Visible Spectrophotometry

As discussed in the following chapters, the performance of a photocatalyst is in large part dependent on the material's optical properties, for example the absorbance

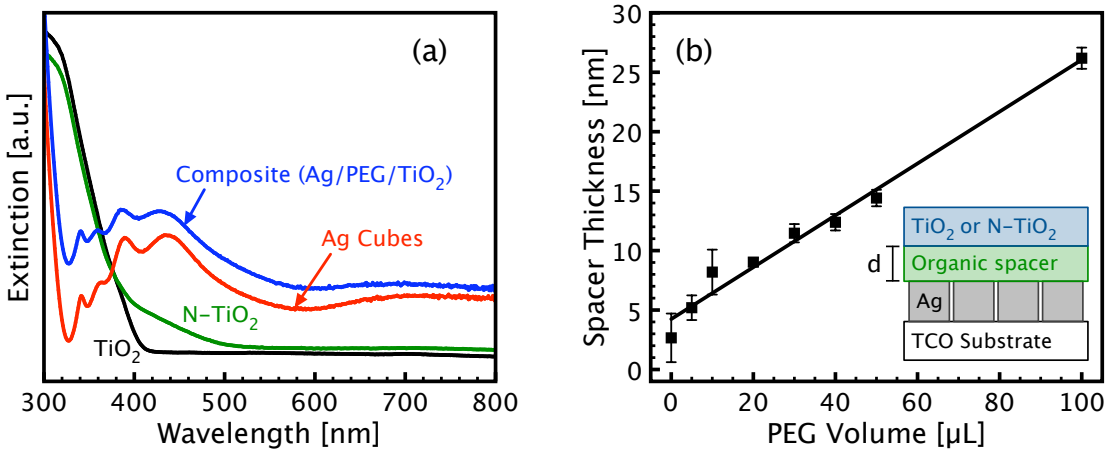

Figure 3.4: Characterization of photocatalysts used in the distance dependence studies in Chapter 6. (a) UV-visible extinction spectra for TiO_2-only, N-TiO_2-only, Ag cubes only and composite Ag/PEG/TiO_2 photocatalysts used in distance dependence studies in Chapter 6. (b) Measured thickness of the polyethylene glycol (PEG) layer applied to a Si substrate as a function of the total applied PEG solution volume, measured by ellipsometry. The inset shows a schematic of the composite photocatalyst construction.

of a semiconductor or the SPR of a metal nanoparticle. These properties dictate how a material responds to a photon flux; for example, the absorbance of a semiconductor is a direct measurement of the fraction of incident photons that produce charge carriers (electron/hole pairs). Spectrophotometry in general refers to a technique for measuring the interaction of a material with photons as a function of the photon wavelength. Since the studies presented in this dissertation use UV and visible light sources, the most useful characterization technique is UV-visible spectrophotometry (or simply UV-vis spectrometry). To explain the quantities that are measured, it is useful to define a few terms.

Absorbance: As mentioned above, absorbance is a measurement of the fraction of photons that interact with the material to produce excited charge carriers (electron/hole pairs). The charge carriers eventually relax and release the stored energy through some non-radiative process such as heating through excitation of phonon modes or through transferring charge to the surroundings [14–16]. This process is referred to as absorption and the measured quantity is the absorbance. Absorbance is usually defined in the field of analytical chemistry as the logarithm (base 10) of I_0/I, where I_0 is intensity of the incident light and I is the intensity of light transmitted through the sample to the detector. The quantity I_0/I is the reciprocal of transmittance, T (the amount of light not absorbed). In certain cases it is more useful to specify the fractional absorbance, which is simply $1 - T$. However, we note that these definitions are most commonly used for analysis of dilute liquid samples, where light may be absorbed due to excitation of electronic transitions in molecules but there is no significant scattering of light (see below). As such, one must be careful when performing the measurements not to falsely attribute any diminution of light to absorbance simply because the spectrometer seems to indicate. For example, if one

were to place a mirror in between the source and detector, the spectrophotometer would indicate 100% of photons were absorbed by the mirror, whereas in reality the measured loss of photons is due to scattering (or more specifically specular reflection).

Scattering: The scattering process is simply the interaction of a photon with a material, in which the net result is that the photon changes direction. This can be due to a few effects, such as the interaction of light with a structure similar in size to the light wavelength. It can also be due to temporary excitation of electronic states or virtual states within a material, which then relax by re-emitting a photon. This process is referred to as Rayleigh scattering if the emitted photon has the same energy as the incident photon, Stokes scattering if the emitted photon has less energy than the incident photon or anti-Stoke scattering if the emitted photon has gained energy. The emitted photons—the vast majority of which are Rayleigh scattered—are emitted in essentially random directions, sometimes called diffuse scattering or diffuse reflection. Because of this, if a sample scatters a high portion of the incident light, then very little signal will reach the detector of the spectrometer. To get around this problem we must use a special version of UV-visible spectrophotometry, referred to as diffuse reflectance spectrometry (DRS), which is discussed below.

Extinction: The total amount of the incident light in a spectrometer that does not reach the detector (i.e., the extinguished light) is called the extinction. Essentially, this amounts to the sum of the absorbance and scattering discussed above. As mentioned above, transmittance through a sample is defined as I_0/I, or the fraction of light that reaches detector. The quantity $1 - T$ then is actually the fractional extinction, rather than the fractional absorbance, since it can include scattering also. In fact, when we measure an "absorbance spectrum" in a spectrophotometer, we are actually measuring the extinction from the sample, and as mentioned above

we must be careful if trying to specifically assign this extinction to absorbance or scattering, since both effects could be present.

All of the spectra measured throughout this document were carried out using a ThermoScientific Evolution 300 UV-visible Spectrophotometer. As mentioned above, the machine nominally measures absorbance and transmittance. However, because of the issues we discussed, the actual measurements are extinction spectra and we have labeled them as such. When analyzing the optical properties of materials from these spectra it is necessary to exercise some judgment to aid interpretation. For example, if measuring the extinction of a semiconductor at photon energies far less than the band gap, one can assume that any measured extinction is due to scattering effects. For plasmonic metal nanoparticles, the extinction is a super-position of absorbance and scattering; the two are not separable using a conventional spectrophotometer.

As mentioned above, some samples scatter a high fraction of light diffusely in all directions (diffuse scattering). This makes it difficult to obtain spectra, as the detector essentially reads zero transmittance for all wavelengths. This is particularly a problem for opaque samples with rough surfaces (not "shiny"), where the beam cannot be passed directly through the sample, and specular reflection is not possible from the top of the sample. To get around this problem, we have used diffuse reflectance spectroscopy. Measurements were obtained using a Harrick Diffuse Reflectance cell within the UV-visible spectrophotometer listed above. The measurement is essentially the same, except that the beam is not passed through the sample, rather the sample is illuminated at an angle. Light is scattered in all directions and a parabolic mirror captures a relatively large portion of the light and focuses it back to the detector. The parabolic mirror does not completely surround the sample, so some light is still lost to scattering. Because of this, the measured quantity is still

extinction. Were the mirrors increased in size such that they collected and focused all scattered light to the detector, the real absorbance of the sample could be directly measured. This apparatus is called an integrating sphere, but such equipment was not employed in these studies.

3.4.2 Photoluminescence Spectroscopy

Photoluminescence (PL) spectroscopy on the surface looks similar to the spectroscopy techniques described above. However, rather than directly measuring the transmittance through a sample as described above, the quantity measured is the emission from the sample. In this way, PL allows a measure of the amount of charge carriers generated in a semiconductor due to illumination with a particular source [17–20]. PL can also be used for other similar measurement in other materials, but we will limit the discussion to semiconductors. A semiconductor sample is illuminated with a monochromatic illumination source, some of which may be absorbed and create electron/hole pairs. Many of the electron/hole pairs emit photons upon relaxation; as discussed above, most photons are Rayleigh scattered (the emitted energy is the same as the incident). The Raleigh scattered photons cannot be distinguished from source photons with the same energy; however, some emitted photons are shifted in energy away from the monochromatic source photons. The fractions of photons that are shifted in energy as well as the emission wavelengths are characteristic of a particular material. The recorded measurement in a PL experiment is the raw intensity of the shifted photons striking the detector as a function of photon energy (wavelength).

Photoluminescence experiments were conducted by recording the emission of photons with wavelength of 467 nm (an emission peak characteristic of anatase TiO_2 [17, 18]) as a function of excitation wavelength under ambient conditions using a Horiba

Jobin Yvon FluoroMax-3 spectrofluorometer. By comparing two samples, one can make comparisons about the relative number of charge carriers formed in the materials. For example, in Chapter 4 we measure the PL emission from a composite Ag/TiO_2 sample at a certain excitation wavelength, normalized by the emission for a TiO_2 sample excited at the same wavelength. The measurements indicated a higher emission at 467 nm for the composite sample compared to the pure semiconductor sample (pure Ag samples showed no discernable emission peaks). Since the emission is proportional to the total number of charge carriers in the semiconductor, this means that the rate of charge carrier formation in the semiconductor was enhanced by the presence of Ag in the composite.

3.5 Photocatalytic Activity Measurements

3.5.1 Methylene Blue Decomposition Experiments (Chapter 4)

To test the photochemical activity of semiconductor-only and composite metal semiconductor photocatalysts in Chapter 4, we measured the rate of photo-decomposition of methylene blue (MB) under illumination with a broadband visible source. MB is a blue dye commonly used as an analog for water-soluble organic pollutants [6, 10, 21–24]. Reactions were carried out at room temperature in a liquid phase batch reaction vessel with an open top. Photocatalyst substrates were placed on the bottom of the vessel, 2 mL of 0.05 mM MB in water was added and the system was allowed to sit in the dark for 1 hour prior to illumination. The system was continuously stirred and aerated by bubbling O_2. The reaction vessel was kept in a room temperature water bath to maintain isothermal reaction conditions.

The system was illuminated from the top by a visible light source with a wavelength range of ∼375–900 nm. MB demonstrates a strong absorbance of light from ∼550–700 nm; to prevent direct photolysis of MB we used a 500 nm short pass

filter to cut off photons with wavelengths higher than 500 nm. This ensures that the reactant molecule is essentially transparent to the source photons [23, 25, 26] and also effectively prevents the possibility of dye sensitization, since MB cannot be directly excited by the light source. The total source power delivered to the catalyst surface was 140 mW/cm^2. Figure 3.5a shows the wavelength distribution of the filtered source and the absorbance of MB. The MB concentration was monitored as a function of time by using transmission UV-visible spectroscopy to observe the decrease in the 610 nm MB peak. Photoluminescence experiments were conducted by recording the emission at 467 nm from the prepared photocatalysts as a function of excitation wavelength under ambient conditions, as described above.

3.5.2 Water Splitting Experiments (Chapter 5)

A glass beaker was fitted with a quartz window; this vessel and the accompanying apparatus described below is referred to as a photoelectrochemical (PEC) cell. The beaker was filled with 1.0 M KOH, which was continuously stirred with a magnetic stir bar and deaerated by bubbling Argon. The photo-electrodes, prepared as described above, were suspended in the beaker facing the quartz window and attached to the working electrode lead of a potentiostat (Princeton Applied Research PARSTAT-2273 Potentiostat/Galvanostat/FRA). A Pt wire counter electrode and Hg/HgO reference electrode were used and a constant external bias of 0.3 V was applied. Under illumination the bias is necessary to help evolve H_2 at the Pt counter-electrode (the photo-excited electrons in the metal are slightly lower in energy than the H+/H_2 potential). Without the bias the H_2 evolution half-reaction does not proceed and thus the process of overall water splitting is not possible [27, 28].

The photo-electrodes were illuminated with a broadband visible light source that delivers a total power of $\sim$500 mW/cm^2 at the photo-electrode surface (see Figure

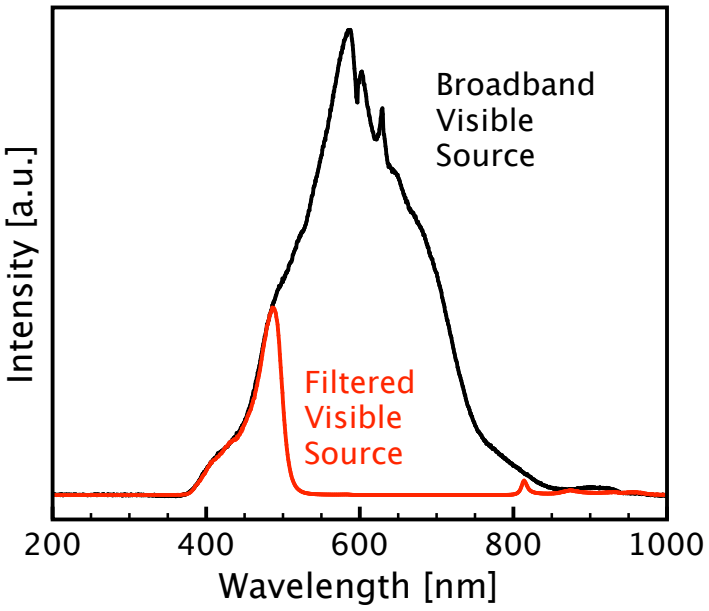

Figure 3.5: Visible light source spectra. Intensity of the broadband visible light source (black curve) as a function of wavelength. Intensity is a function of distance from the source; specific intensity values are reported within the subsequent chapters. The red curve shows the intensity of the broadband visible light source with 500 nm short pass filter, as used in Chapter 4.

3.5b). Wavelength dependent studies employed a series of optical filters to isolate the broadband source into roughly monochromatic points with a full-width at half-maximum (FWHM) of ∼25 nm. A monochromatic UV light source (365 nm, FWHM 5 nm, ∼5 mW/cm^2) was also used in these studies in order to probe activity in the UV region of the spectrum.

The water splitting reaction rate was monitored by measuring the evolved gases using quadupole mass spectrometry and by measuring the photocurrent conducted around the external circuit through the potentiostat. The cell was closed by fitting a glass dome with electrical feed throughs to accommodate the electrode connections. Argon was continuously bubbled through the cell at a known flow rate (5 sccm). Bubbling Argon helped to reduce back reaction due to dissolved oxygen in the water, helped to provide mixing in the cell and also acted as a carrier gas to help sweep the evolved H_2 and O_2 from the cell to the mass spectrometer. An electron multiplier was used to facilitate the measurement of small quantities of H_2 and O_2. Before each run, the mass spectrometer readings were carefully calibrated with known flow rates of gas containing known quantities of H_2, O_2, H_2O and Ar. We note that the mass spectrometry measurements showed no evidence of the evolution of carbon-containing species.

The photocurrent was monitored as a measure of the water splitting reaction rate using a Princeton Applied Research PARSTAT-2273 Potentiostat/Galvanostat/FRA under constant external bias of 0.3 V. Two molecules of water that are transformed into $2H_2$ and O_2 produces 4 electrons that flow through the external circuit. If we assume that the reaction occurring in the cell is the overall splitting over water, then the photocurrent is proportional to the reaction rate. To check this assumption the amount of gasses produced was also measured using mass spectrometry. As shown

in Chapter 5, H_2 and O_2 were produced in the correct stoichiometric amounts (i.e. 2 moles of H_2 for each mole of O_2), which suggests that the process occurring in the cell is in fact the overall splitting of water to form H_2 and O_2.

3.5.3 Distance Dependence Experiments (Chapter 6)

In Chapter 6, the photo-activity of samples was determined by measuring the PL emission and photocurrent generated in a PEC cell, exactly as described above for Chapters 4 and 5. Both TiO_2 and N-TiO_2 samples were constructed, both with and without the addition of Ag nanocubes. TiO_2 and Ag/TiO_2 samples were illuminated in the PEC cell by the 365-nm monochromatic source mentioned above and the resulting photocurrent was monitored. PL emission at 467 nm was also measured from these samples upon monochromatic 365-nm illumination. Photocurrent measurements and PL emission measurements for N-TiO_2 and Ag/N-TiO_2 samples upon illumination with 365-nm photons were indistinguishable from that of TiO_2-based samples. To obtain another data point and compare differences in activity upon changing the semiconductor excitation, N-TiO_2-based samples were illuminated with monochromatic 400-nm light and the resulting PL emission was measured. Unfortunately, a suitable monochromatic 400-nm light was not available for photocurrent measurements (Chapter 5 presents photocurrent upon illumination with broadband visible light).

3.6 Computational Methods (Optical Simulations)

The analyses in the following chapters depend heavily on optical simulations to predict analyze the behavior of materials in response to a photon flux. The optical simulations are particularly useful for investigating the plasmonic properties of metal nanoparticles. The simulations methodology is described below, along with a

description of the required inputs and the available outputs.

3.6.1 The Finite-Difference Time-Domain Method

Optical simulations were implemented using the finite-difference time-domain (FDTD) method (simulations were performed with two spatial dimensions unless otherwise noted). FDTD is a computational electro-dynamics modeling technique, which solves discretized Maxwell equations in space and time subject to the input geometry, material properties, and boundary conditions [29]. The specific code used was developed recently by Jeffrey McMahon at Northwestern University [30]. The optical properties of metals were represented using a Drude-Lorentz model [31, 32] with empirical optical constants [7], as described below. Unless otherwise noted, the background medium in simulations was water, which is implemented by specifying a constant background dielectric constant of 1.77 everywhere in the simulation cell not occupied by some other material. The perfectly matched layer (PML) construct [29] was used to truncate the simulation cell in all directions. The PML structures essentially absorb all light exiting the simulation cell (once the light has passed through, no radiation bounces back into the cell due to interactions with the system boundary). Incident radiation for all simulations was supplied via a Gaussian source with radiation in the region of approximately 200–1000 nm. The intensity across this range was not constant; to account for this, results at each wavelength were normalized by the source intensity at that wavelength. Figure 3.6 shows a sketch of a typical simulation geometry for a Ag cube. The material geometry is defined by specifying the dielectric constant as a function of wavelength on every point of a grid of points. Aside from material geometry, the materials' dielectric functions are the most important input in the FDTD simulations.

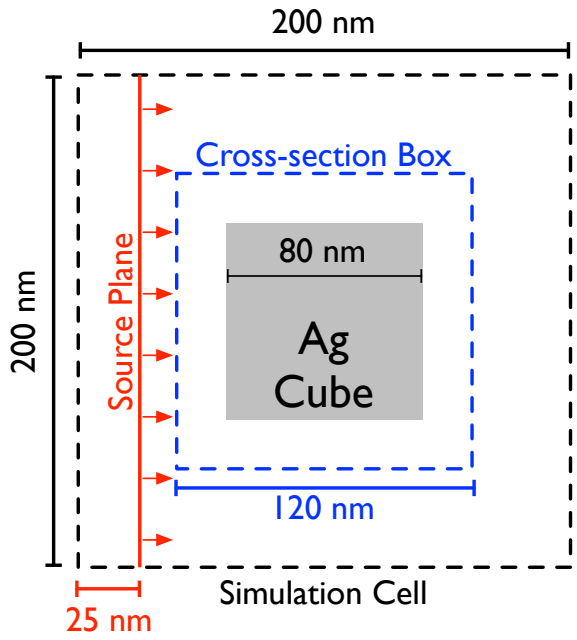

Figure 3.6: Example simulation cell geometry for finite-difference time-domain optical simulations. In this example, the total simulation area is 200 nm by 200 nm and the structure to be investigated is a silver cube with 80-nm edge length (actually a square, since this shows a two dimensional simulation). Source illumination (depicted in red) enters the cell from the left hand side, normal to the left boundary. The total-field scattered-field (TFSF) cross-section box is illustrated in blue surrounding the Ag structure.

3.6.2 Metal Optical Properties

Plasmonic metals are simulated by numerically modeling the dielectric function over the wavelengths of interest. Figure 3.7 shows the real and imaginary components of the Ag dielectric constant as a function of wavelength (data from ref. [33]). As discussed in Chapter 2, the interaction of light with a plasmonic metal is essentially the sum of two effects: (1) interband transitions (d- to sp-band excitations) and (2) the plasmon resonance, which is an intra-band effect. The dielectric function is modeled by a sum of terms that capture these effects, shown in Equation 3.1.

$$\epsilon(\omega) = \epsilon_\infty - \frac{\omega_D^2}{\omega^2 + i\gamma_D\omega} - \frac{\Delta\epsilon g_{L_1}\omega_{L_1}^2}{\omega^2 + 2i\gamma_{L_1}\omega - \omega_{L_1}^2} - \frac{\Delta\epsilon g_{L_2}\omega_{L_2}^2}{\omega^2 + 2i\gamma_{L_2}\omega - \omega_{L_2}^2} \tag{3.1}$$

The first term, ϵ_∞, is the dielectric constant at the limit of infinite frequency. The second term is the Drude model, which captures intraband effects (i.e. plasmon resonance) [31, 32]. ω_D is the plasma frequency and γ_D is the collision frequency. The contribution of interband transitions to the dielectric function is modeled using a 2-pole Lorentz oscillator model, which is the final two terms in Equation 3.1 [31, 32]. Two terms are included because, over the UV-visible portion of the spectrum, Au has two interband transitions (peaking around 3 and 4 eV [7, 8]) while Ag has one transition around 3.8 eV (having the extra term does not adversely effect the Ag model, it simply makes the model fit the data better). In the Lorentz terms, ω_L is the frequency corresponding to the transition, $\Delta\epsilon_L$ is the shift in the relative permittivity at the transition and γ_L is the electron dephasing rate. The four terms discussed above are combined, resulting in Equation 3.1, which is referred to the Drude plus 2-pole Lorentz (D2L) model.

While the Drude and Lorentz parameters can be determined from a material's

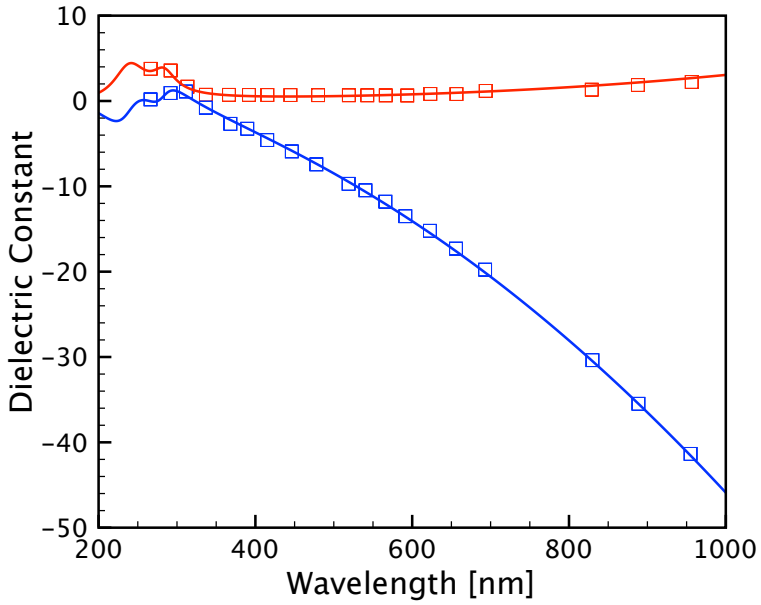

Figure 3.7: Dielectric constant data and empirical Drude-Lorentz model fit for Ag. Experimental data for the real (blue points) and imaginary (red points) dielectric constant of Ag are from ref. [33]. Drude-Lorentz model parameters for the fit (solid lines) are from ref. [34].

bulk physically properties (for example, the plasma frequency), it is more common and more accurate to adjust the model parameters to empirically fit experimental dielectric function data, as shown in Figure 3.7 for Ag [33]. The figure also shows the D2L model fit to this data, using parameters determined in ref. [34]. Similar analysis was performed for the Au dielectric function by ref. [7]. The parameters used for both metals have been shown to give accurate results for Ag and Au nanostructures [35, 36].

3.6.3 Semiconductor Optical Properties

Most of the simulations in the following chapters contain metal particles only. The purpose of the simulations is to predict the optical properties (SPR) of metal nanoparticles and to theoretically probe the near-field electromagnetic fields formed near the metal nanoparticles in response to the excitation of SPR. However, it is common in the literature to see FDTD simulations that also incorporate semiconductor materials and indeed we have also done so in a few places. In theory it is possible to simulate the optical response of any material as long as a suitable model for the dielectric function is available. Typically in the literature semiconductors are represented as a constant dielectric material as mentioned for the water background above (e.g. a constant real dielectric of 2.25 for all wavelengths for SiO_2 or $\sim$9 for TiO_2 [7]). In fact, this was the only method for including semiconductors in the FDTD code from ref. [30]. However, this approach captures only the effect of photon scattering and not photon absorption (which is due to the imaginary portion of the dielectric function). This works in the UV-visible spectrum for materials such as SiO_2, which does not have absorption in this range of the spectrum. However, for certain applications it is desirable to capture the semiconductor absorption effects in the simulations. For example, when modeling the UV-visible response of TiO_2 it

is necessary to capture the absorption of photons due to valence-to-conduction band electron transitions at wavelengths lower than the band gap (387 nm).

To incorporate the effects of TiO_2 absorbance (an interband transition effect), the same D2L model discussed above was used for the dielectric function. Experimental data for the dielectric constant as a function of wavelength was obtained from literature for anatase TiO_2, shown in Figure 3.8a [37]. The D2L model parameters were then fit to this data. The Drude term in Equation 3.1 is not necessary since there are no intra-band transitions for TiO_2, so the Drude parameters were all defined as zero. Only one Lorentz term is strictly necessary for TiO_2; however, two terms were necessary to capture the direct and indirect transitions in hematite Fe_2O_3. In addition, the code implements two terms regardless of material and using both for TiO_2 simply increases the numerical accuracy of the empirical fit. The D2L parameters determined for TiO_2 are shown in Table 3.1 and the resulting fit is plotted in Figure 3.8a along with the experimental data from ref. [37]. The resulting simulated absorption cross-section for anatase TiO_2 is shown in Figure 3.8b, along with the simulated absorption using the standard constant dielectric model.

Table 3.1: 2-pole Lorentz Model Parameters

	ϵ_∞	$\Delta\epsilon g_{L_1}$	ω_{L_1}	γ_{L_1}	$\Delta\epsilon g_{L_2}$	ω_{L_2}	γ_{L_2}
TiO_2	4.9	0.1	4.03 eV	0.1 eV	2.45	4.77 eV	0.55 eV
Fe_2O_3	3.3	2.2	4.52 eV	1.0 eV	1.9	2.96 eV	0.5 eV

The same procedure was repeated to determine D2L parameters for the implementation of hematite Fe_2O_3. No hematite simulations were performed for this dissertation; however, the resulting D2L parameters may be interesting to readers, so they are also included in Table 3.1. The empirical fit for Fe_2O_3 is shown in Figure 3.9a along with experimental data from ref. [38] and the resulting simulated absorption cross-section is shown in Figure 3.9b. Comparison of Figure 3.9b to experimental

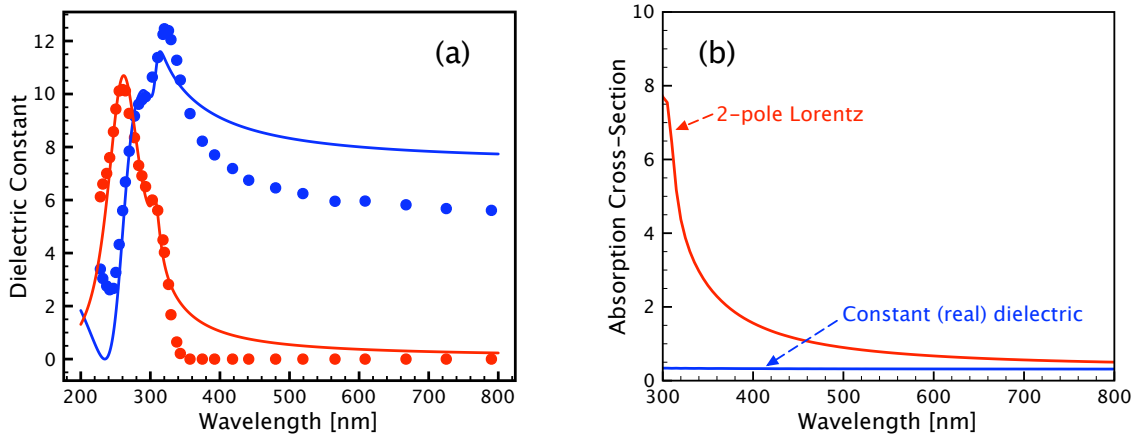

Figure 3.8: 2-pole Lorentz model of the optical properties of anatase TiO_2. (a) Experimental data for the real (blue points) and imaginary (red points) portions of the anatase dielectric function, from ref. [37]. Solid lines show the empirical fit using a 2-pole Lorentz model, with the resulting TiO_2 parameters given in Table 3.1. (b) Simulated absorbance cross-section (in arbitrary units) for anatase TiO_2 using a positive real dielectric constant at all wavelengths (blue line) or using the 2-pole Lorentz model for the complex dielectric function (red line).

spectra for anatase TiO_2 reveals that the absorbance is not predicted with perfect accuracy, but for the initial studies herein it is at least captured qualitative.

3.6.4 Types of Output

There are primarily two types of outputs produced from the FDTD simulations that are presented in the following chapters: simulated spectra and local electric field distributions. In addition. These output types are discussed below.

Simulated Spectra

Scattering, absorbance and extinction cross sections were calculated using the total-field/scattered-field (TFSF) formalism [29]. Essentially, the simulation cell is divided into two regions: the total field region and the scattered field region, as depicted in Figure 3.10a. The illumination source enters the simulation cell on the left hand side, with electromagnetic waves entering the TFSF box normal to the left-hand surface. After passing through the structure, any EM waves exiting the TFSF box normal to the right-hand side (i.e. the waves have not been deflected) is recorded as transmittance. Extinction is calculated as the intensity of incident illumination (entering the left side of the TFSF box) minus the transmitted intensity and then normalized by the intensity of incident illumination. The intensity of illumination exiting the TFSF box in all other directions is recorded as scattering. Absorbance spectra are then determined by subtracting scattering from extinction. The spectra are reported as extinction, absorbance or scattering cross-section, which has dimensions of length in these two-dimensional simulations. Figure 3.10b shows simulated extinction, absorbance and scattering spectra for a 120-nm Ag cube in water. Several points in the following chapters discuss extinction efficiency, which is simply defined as the calculated extinction cross-section for a nanoparticle at a

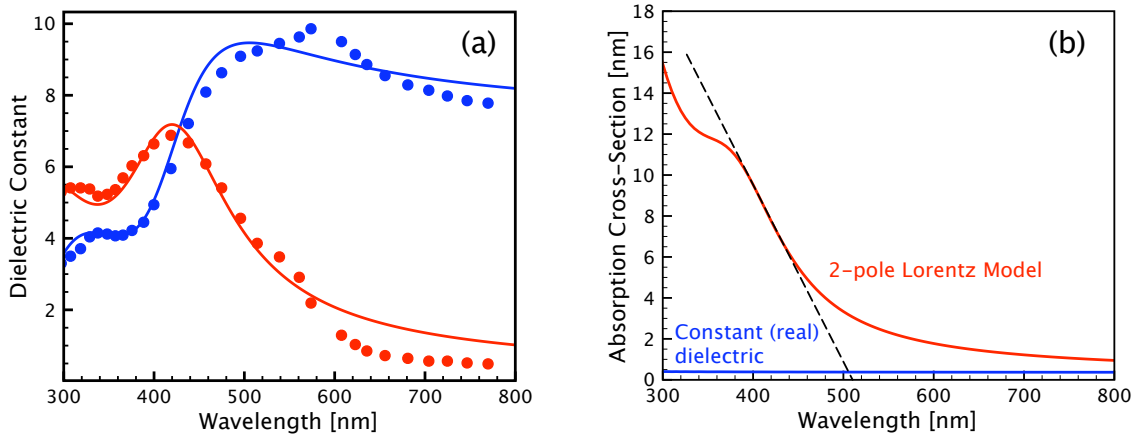

Figure 3.9: 2-pole Lorentz model of the optical properties of hematite Fe_2O_3. (a) Experimental data for the real (blue points) and imaginary (red points) portions of the hematite dielectric function, from ref. [38]. Solid lines show the empirical fit using a 2-pole Lorentz model, with the resulting Fe_2O_3 parameters given in Table 3.1. (b) Simulated absorbance cross-section (in arbitrary units) for hematite Fe_2O_3 using a positive real dielectric constant at all wavelengths (blue line) or using the 2-pole Lorentz model for the complex dielectric function (red line).

given wavelength divided by the geometric cross-section of the particle (scattering and absorbance efficiency are defined analogously). Another type of calculation presented in Chapter 4 is called "power dissipation". Essentially it is analogous to the calculation of absorbance spectra described above, except that absorbance is calculated locally only in a small region of space rather than averaged over the entire simulation cell. This is accomplished simply by changing the location and size of the TFSF box, so that rather than surrounding all of the simulation structures, it only encompasses a small area of interest. This is useful, for example, if we want to calculate how the absorbance of a semiconductor changes upon excitation of a nearby plasmonic metal structure. In this case, we do not want to measure the absorbance within the metal structure itself, which would be included in the overall system spectra.

Simulated Electric Fields

The other primary output from the FDTD simulations are spatial distributions of electric fields. In the simulation code, the electric field strength is monitored as a function of time at all points in space [30]. The field strength is normalized by the field strength associated with the incident photon flux, then Fourier transformed and the strength at a particular wavelength is plotted as a function of position. Note that typically the figures plot normalized field intensity ($|E|^2/|E_0|^2$) rather than simply field strength; a typical example is shown in Figure 3.10c.

3.7 Conclusion

The sections above detailed the synthesis, preparation, characterization and computational methods used frequently in the following chapters. Synthesis and sample preparation methods were described, and some material characterization was pre-

sented. This was followed by a description of the commonly used characterization methods (primarily UV-visible spectrophotometry). The measurements used to test photoactivity of samples were presented on a chapter-by-chapter basis. Finally, the FDTD optical simulation technique was described, including the major required inputs (dielectric functions of materials) and the major types of output used. The subsequent chapters in the document explain some methods specific to experiments within those sections and also refer back to sections within this chapter.

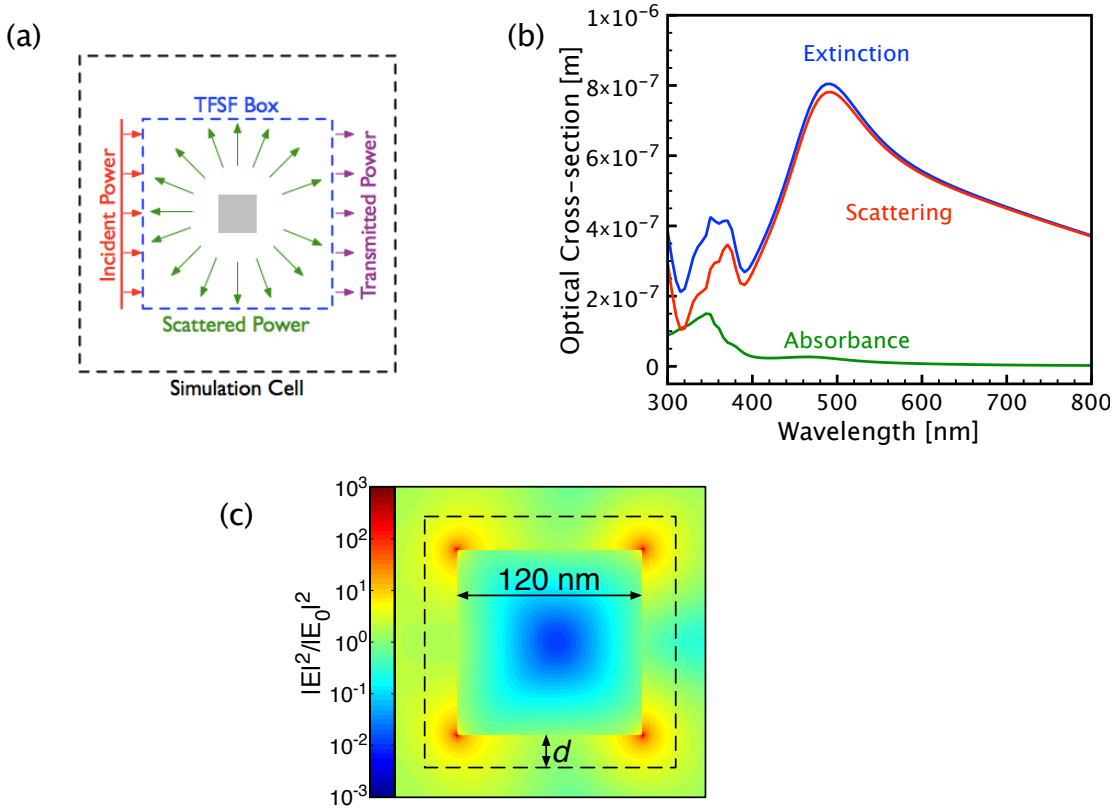

Figure 3.10: Summary of the major types of FDTD outputs. (a) Schematic showing how spectra are calculated. Radiation that passes through the TFSF box without changing angle is recorded as transmittance. The incidence less the transmittance is the extinction. Radiation leaving the TFSF box in all other directions is recorded as scattering, and absorbance is determined by subtracting scattering from extinction. (b) Simulated extinction, scattering and absorbance spectra for a Ag nanocube with 120-nm edge length in water. (c) Calculated enhancement in the intensity of electric fields oscillating at 500 nm (the top of the SPR peak) for the same 120-nm Ag cube simulation.

References

[1] Im, S. H.; Lee, Y. T.; Wiley, B.; Xia, Y. *Angewandte Chemie* **2005**, *44*, 2154–2157.

[2] Xia, Y.; Xiong, Y.; Lim, B.; Skrabalak, S. E. *Angew. Chem. Int. Ed.* **2009**, *48*, 60–103.

[3] Rycenga, M.; Cobley, C. M.; Zeng, J.; Li, W.; Moran, C. H.; Zhang, Q.; Qin, D.; Xia, Y. *Chem. Rev.* **2011**.

[4] Christopher, P.; Ingram, D. B.; Linic, S. *J. Phys. Chem. C* **2010**, *114*, 9173–9177.

[5] Christopher, P.; Linic, S. *ChemCatChem* **2010**, *2*, 78–83.

[6] Christopher, P.; Xin, H.; Linic, S. *Nat. Chem.* **2011**, *3*, 467–472.

[7] Palik, E. D. *Handbook of Optical Constants of Solids*; Academic Press: New York, 1985.

[8] Pinchuk, A.; von Plessen, G.; Kreibig, U. *J. Phys. D: Appl. Phys.* **2004**, *37*, 3133–3139.

[9] Irie, H.; Watanabe, Y.; Hashimoto, K. *J. Phys. Chem. B* **2003**, *107*, 5483–5486.

[10] Asahi, R.; Morikawa, T.; Ohwaki, T.; Aoki, K.; Taga, Y. *Science* **2001**, *293*, 269–271.

[11] Zhang, Z.; Goodall, J. B. M.; Morgan, D. J.; Brown, S.; Clark, R. J. H.; Knowles, J. C.; Mordan, N. J.; Evans, J. R. G.; Carley, A. F.; Bowker, M.; Darr, J. A. *Journal of the European Ceramic Society* **2009**, *29*, 2343–2353.

[12] Gole, J. L.; Stout, J. D.; Burda, C.; Lou, Y.; Chen, X. *J. Phys. Chem. B* **2004**, *108*, 1230–1240.

[13] Sato, S.; Nakamura, R.; Abe, S. *Applied Catalysis A: General* **2005**, *284*, 131–137.

[14] Nozik, A. J.; Memming, R. *J. Phys. Chem.* **1996**, *100*, 13061–13078.

[15] Fujishima, A.; Rao, T. N.; Tryk, D. A. *J. Photochem. Photobio. C* **2000**, *1*, 1–21.

[16] Fujishima, A.; Zhang, X.; Tryk, D. A. *Surf. Sci. Rep.* **2008**, *63*, 515–582.

[17] Anpo, M.; Tomonari, M.; Fox, M. A. *J. Phys. Chem.* **1989**, *93*, 7300–7302.

[18] Zhang, W. F.; Zhang, M. S.; Yin, Z.; Chen, Q. *Applied Physics B* **2000**, *70*, 261–265.

[19] Lee, J.; Govorov, A. O.; Dulka, J.; Kotov, N. A. *Nano Lett.* **2004**, *4*, 2323–2330.

[20] Jung, K. Y.; Park, S. B.; Anpo, M. *J. Photochem. Photobio. A* **2005**, *170*, 247–252.

[21] Mills, A.; Wang, J. *J. Photochem. Photobio. A* **1999**, *127*, 123–134.

[22] Houas, A.; Lachheb, H.; Ksibi, M.; Elaloui, E.; Guillard, C.; Herrmann, J.-M. *Appl. Catal. B* **2001**, *31*, 145–157.

[23] Yan, X.; Ohno, T.; Nishijima, K.; Abe, R.; Ohtani, B. *Chem. Phys. Lett.* **2006**, *429*, 606–610.

[24] Kumar, M. K.; Krishnamoorthy, S.; Tan, L. K.; Chiam, S. Y.; Tripathy, S.; Gao, H. *ACS Catal.* **2011**, *1*, 300–308.

[25] Ohtani, B. *Chem. Lett.* **2008**, *37*, 217–229.

[26] Ohtani, B. *J. Photochem. Photobio. C* **2010**, *11*, 157–178.

[27] Bard, A. J.; Fox, M. A. *Acc. Chem. Res.* **1995**, *28*, 141–145.

[28] Walter, M. G.; Warren, E. L.; McKone, J. R.; Boettcher, S. W.; Mi, Q.; Santori, E. A.; Lewis, N. S. *Chem. Rev.* **2010**, *110*, 6446–6473.

[29] Taflove, A.; Hagness, S. C. *Computational Electrodynamics: The Finite-Difference Time-Domain Method*; Artech House: Boston, 2005.

[30] McMahon, J. M. Ph.D. thesis, Northwestern University: Evanston, Illinois, 2010.

[31] Wooten, F. *Optical Properties of Solids*; Academic: New York, 1972.

[32] Ashcroft, N. W.; Mermin, N. D. *Solid State Physics*; Brooks Cole, 1976.

[33] Lee, T.-W.; Gray, S. K. *Optics Express* **2005**, *13*, 9652–9659.

[34] Johnson, P. B.; Christy, R. W. *Physical Review B* **1972**, *6*, 4370–4379.

[35] Link, S.; El-Sayed, M. A. *J. Phys. Chem. B* **1999**, *103*, 4212–4217.

[36] McMahon, J. M.; Wang, Y.; Sherry, L. J.; Van Duyne, R. P.; Marks, L. D.; Gray, S. K.; Schatz, G. C. *Journal of Physical Chemistry C* **2009**, *113*, 2731–2735.

[37] Cabrera, M. I.; Alfano, O. M.; Cassano, A. E. *J. Phys. Chem.* **1996**, *100*, 20043–20050.

[38] Chen, C. T.; Cahan, B. D. *J. Opt. Soc. Am.* **1981**, *71*, 932–934.

CHAPTER 4

Predictive Models for Plasmonic Metal/Semiconductor Photocatalysts

4.1 Summary

We demonstrate the design of composite plasmonic metal/semiconductor photocatalysts, which show enhanced visible light photocatalytic activity compared to the semiconductor alone. We show that the overlap between the illumination source spectrum, semiconductor absorbance spectrum and metal nanoparticle surface plasmon resonance spectrum provides a useful descriptor for predicting the relative rate enhancements induced by metal surface plasmons for composite photocatalysts with similar arrangements of metal and semiconductor building blocks. We also show that optical simulations can be used to predict the value of the descriptor of photocatalytic activity for any arbitrary combination of illumination source, semiconductor, and plasmonic metal, and therefore guide the formulation of optimal composite photocatalysts. We have used optical simulations to identify optimal plasmonic nanostructures for a few model low and large band gap semiconductors.

4.2 Introduction

Upon illumination, a semiconductor photocatalyst can absorb photons with energy exceeding the material's band gap and transfer the energy of light into excited

charge carriers (electron/hole pairs), which can then drive reactions at the photocatalyst surface. As mentioned in Chapter 2, oxide semiconductors have been shown to be useful for a range of photochemical transformations including photo-decomposition of organics and water splitting reactions [1–3]. However, due to low efficiencies of semiconductors in conversion of incident photons to useful charge carriers at the semiconductor surface, these photochemical processes generally exhibit low rates. As discussed in Chapter 2, it has recently been suggested that photo-excited, plasmonic nanostructures of silver (Ag) embedded in a matrix of TiO_2 can enhance the photocatalytic activity of TiO_2 [4, 5]. The critical characteristic of the Ag/TiO_2 composites governing the enhancements in photocatalytic rates is high optical activity of Ag nanoparticles manifested in the light-induced excitation of surface plasmon resonance (SPR) [6–9].

In Chapter 2 we outlined five possible mechanisms that could play a role when a photo-excited plasmonic metal is added to a semiconductor. As discussed, the SPR-induced heating mechanism requires a very intense light source and is negligible under sun-light illumination [10–12]. The co-catalyst mechanism discussed can have an effect, but is not dependent on the metal SPR [13–17]. Consequently, there are three primary mechanisms by which metal SPR can enhance the reaction rates on nearby semiconductors. In the first mechanism, often termed the charge transfer mechanism, it is proposed that SPR leads to the transfer of charge from photo-excited metal to the semiconductor, and that the charged semiconductor induces photo-catalytic transformations [17–21]. The second mechanism is based on the interaction of metal SPR with nearby semiconductor via an SPR-induced enhanced electromagnetic field, which leads to increased rates of e/h formation in the semiconductor, resulting in larger rates of photocatalytic reactions [4, 5, 22–25]. The third mechanism, the so-

called "scattering mechanism" as discussed in Chapter 2, is expected to have some effect, since the addition of metal nanoparticles does increase the extinction of the samples [26–28]. While this mechanism is reported to be the dominant effect in some systems (for example, in thin film solar cells [28]), it is generally observed to play a minor role in these photocatalytic experiments. This is because the semiconductor photocatalysts in these systems generally absorb most of the incident photons to begin with, so there is an upper limit on the possible enhancement due to increase in average photon pathlength. For example, if a semiconductor initially absorbs 50% of incident photons (absorbance value of 0.68), then the upper bound on the enhancement due to the scattering mechanism would be a factor of 2. In reality, these systems usually have significantly higher initial absorbance [4, 5] and reported rate enhancement factors are as high as 7 [4].

As discussed in Chapter 2, it has been hypothesized that the photocatalytic reaction rates on the composite photo-catalysts depend on multiple factors, including catalytic and optical properties of semiconductor and plasmonic metal building blocks and the geometric placement of the building blocks with respect to each other [5, 17, 23]; however, there are very few examples of direct investigations in the literature that separate the various possible mechanisms. Because of this, predictive models that capture the effects of these factors on the reaction rates are missing. In this chapter we take a step towards developing these models by probing how the optical properties of individual building blocks affect the reaction rates on composite photocatalysts. Photocatalysts used in these studies were designed not to exhibit any charge transfer between metal and semiconductor building blocks, i.e., the dominant interaction between the building blocks was due to SPR-induced electromagnetic field (this is discussed more below). We show that the overlap between

the wavelength of source photons, the absorption spectrum of the semiconductor, and the metal SPR spectrum is an excellent descriptor of photocatalytic activity of the composite photo-catalysts. We also demonstrate how this optical overlap descriptor of photo-catalytic activity allows for rapid evaluation of potential effectiveness of plasmonic metal nanoparticles of particular composition, shape and size, as promoters of photochemical activity of random semiconductors with any light source. We arrived to these conclusions by testing the photocatalytic activity of two semiconductor photocatalysts with different optical properties, TiO_2 and nitrogen-doped TiO_2 (N-TiO_2), upon addition of two plasmonic metal nanostructures with different optical properties: nanocubes of Ag of $\sim$ 120 nm edge length and nanospheres of Au of $\sim$ 25 nm diameter. The use of two different semiconductors (TiO_2 and N-TiO_2), two different metals (Ag and Au) and different metal weight loadings gives us several ways to change the system optical properties and correlate this to the resulting catalytic activity, as described below.

The photocatalytic activity was quantified in studies of the photo-decomposition of methylene blue (MB). Methylene blue (MB) is a bright blue organic dye molecule that is commonly used as an analog for water-soluble organic pollutants. This decomposition of MB is activated by energetic holes at the semiconductor surface [29, 30]. MB is a strong absorber of light around 550–700 nm (see Figure 4.2a). This is beneficial because the concentration of MB can be easily monitored using quick and accurate UV-visible absorption measurements. However, the visible absorption of dyes (such as MB) has also been reported to cause problems with the interpretation of experimental results when the compound is directly excited with the experimental light source [31–33]. There are several issues: (1) At wavelengths overlapping with the TiO_2 absorbance (i.e. approximately 420 nm and below, "Region I" in ref [31]),

the degradation of MB is catalyzed by the semiconductor, as discussed above. This is specifically the region of interest—i.e. the region in which the degradation of MB is catalyzed by TiO_2. (2) At wavelengths where there is negligible excitation of the TiO_2 absorbance or the MB absorbance (i.e. ∼420–550 nm for P25, "Region II" in ref. [31]) the degradation of MB is negligible. This is also shown by the action spectra for MB on P25 from ref. [31]. (3) However, at illumination wavelengths overlapping with the MB absorbance (∼550–700 nm), degradation can be due to direct photolysis of MB or a photosensitization effect. Photolysis refers simply to the un-catalyzed light-induced degradation of MB due to direct absorbance of photons. Photosensitization also involves direct absorbance of photons by the MB compound. However, this is followed by a transfer of an excited electron to the nearby semiconductor, leaving a positively charged MB ion, which then degrades. As a side note: this charge transfer process is the driving phenomenon behind dye-sensitized solar cells [34, 35]. The observed MB degradation in the wavelength range of (∼550–700 nm) in the action spectrum from ref. [31] (labeled "Region III" in that paper) clearly indicates the presence of photolysis and/or photosensitization effects, although the rates are very low compared to rates when the semiconductor absorbance is excited.

Because of these issues described in (3) above, it is sometimes concluded that visible dyes should not be used to characterize the photo-catalytic activity of semiconductors upon illumination with visible light [31–33]. However, this is somewhat of an overall generalization. It is more accurate to say that in order to avoid such issues, one should use a reactant molecule that is transparent to the source photons. To ensure this was the case, we have been careful to use a light source that does not overlap with the direct light absorbance of MB. The experiments with MB only and no photocatalyst (called "blank" in Figure 4.2b) as well as a comparison of our re-

sults with TiO_2 and N-TiO_2 confirm that we have successfully reduced or eliminated the effects of photolysis and photosensitization (this is discussed further below).

4.3 Methods

The TiO_2 photocatalyst was Degussa/Evonik P25 TiO_2 (∼20 nm diameter particles, ∼80% anatase phase). Nitrogen-doped TiO_2 (N-TiO_2) was synthesized by heating P25 TiO_2 particles in flowing gaseous NH_3 at 500°C for 5 hours [36]. Detailed synthesis methods are discussed in the Synthesis section of Chapter 3. N-TiO_2 has been investigated extensively in the literature, and this method has been found to yield N-TiO_2 powders with low N dopant concentrations, which show improved visible light activity compared to TiO_2 [36]. The UV-visible extinction spectra for TiO_2 and N-TiO_2 used in the experiments below are shown in Figure 4.1.

Cubic Ag nanoparticles were synthesized using a modified polyol process, described in detail in the literatureChristopher2010a, Christopher2011, Im2005 and also discussed in the Synthesis section of Chapter 3. Briefly, Ag nanocubes were produced by slow addition of $AgNO_3$ (precursor) and polyvinylpyrrolidone (stabilizer) to a solution of ethylene glycol (solvent and reductant) and dilute HCl (etchant). The result was cubic Ag nanoparticles with a layer of polyvinylpyrrolidone (PVP) stabilizer on the surface to prevent agglomeration. The particles were washed with acetone once via centrifugation and re-dispersed in 200-proof ethanol. The particle size (edge length of 118 ± 25 nm) was determined from scanning electron microscopy (SEM); a representative SEM image is shown in Figure 4.1. Micrographs were obtained using an FEI Nova 200 Nanolab. The accelerating voltage was 5 kV. Spherical Au particles were synthesized in a process identical to that previously reported in detail for Ag nanospheres [37], except that $AgNO_3$ is replaced with the same con-

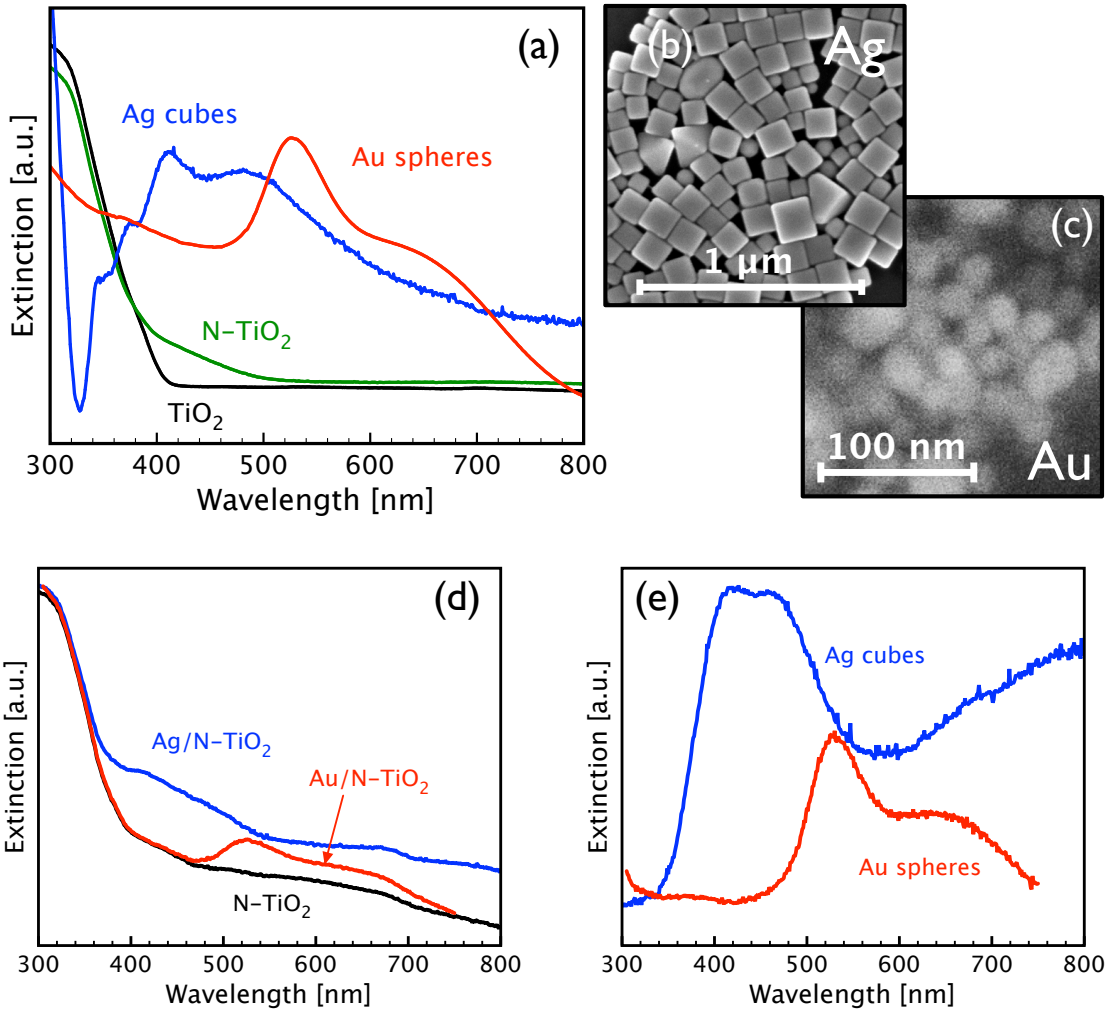

Figure 4.1: Characterization of metal and semiconductor building blocks and composite samples. (a) Diffuse reflectance UV-visible (DRUV) spectra of TiO_2, N-TiO_2, Ag nanocube and Au sphere films on a SiO_2 substrate. (b) Scanning electron micrograph (SEM) of the Ag nanocube sample (edge length 118 ± 25 nm). (c) SEM of spherical gold particles (diameter 25.4 ± 4.5 nm). (d) Diffuse reflectance UV-visible (DRUV) spectra of N-TiO_2, Ag/N-TiO_2 composite (4.5 wt% Ag) and Au/N-TiO_2 composite (4.5 wt% Au) samples. (e) Ag and Au difference spectra for the composite samples in (d), obtained by subtracting the N-TiO_2 spectrum from the composite spectra.

centration of $AuCl_4$. The resulting Au spheres were 25.4 ± 4.5 nm in diameter, as measured by SEM (Figure 4.1). We note that as used Ag and Au nanoparticles were coated with a non-conductive polymer layer (PVP); we comment more on this below.

Semiconductor (TiO_2 and N-TiO_2) and metal (Ag and Au) nanoparticles were independently suspended in pure ethanol and sonicated. Single-component samples (for example, TiO_2-only or Ag-only) were prepared by drop-coating these suspensions onto 1-cm^2 SiO_2 substrates and drying in a stagnant ambient atmosphere. Composite suspensions were prepared by combining the pure nanoparticle suspensions and thoroughly mixing using agitation and sonication. Composite photocatalyst samples (for example, Ag/TiO_2) were prepared by the same drop-coating method using the mixed nanoparticle suspensions. This resulted in a physical mixture of the two types of particles on the substrate; however, we note that because the metal particles are coated with PVP, there was minimal direct contact between semiconductor and metal particles within the composites. All photocatalysts samples used in the experiments contained constant weight (as well volume and surface area) of semiconductor particles. The amount of metal nanoparticles in the composite mixtures was varied, and the percentages listed in the text and figures indicate weight percent of the metal particles with respect to the constant weight of semiconductor particles.

To test the photochemical activity we measured the rate of photo-decomposition of methylene blue (MB) under illumination with a broadband visible source. Reactions were carried out at room temperature in a liquid phase batch reaction vessel with an open top. Photocatalyst substrates were placed on the bottom of the vessel, 2 mL of 0.05 mM MB in water was added and the system was allowed to sit in the dark for 1 hour prior to illumination. The system was continuously stirred and aerated by bubbling O_2. The reaction vessel was kept in a room temperature water bath to

maintain isothermal reaction conditions.

The system was illuminated from the top by a visible light source with a wavelength range of ∼375–900 nm. MB demonstrates a strong absorbance of light from ∼550–700 nm (see Figure 4.2); therefore, to prevent direct photolysis of MB we used a 500 nm short pass filter to cut off photons with wavelengths higher than 500 nm. As discussed above, this ensures that the reactant molecule is essentially transparent to the source photons [31], and also effectively prevents the possibility of dye sensitization, since MB cannot be directly excited by the light source. The total source power delivered to the catalyst surface was 140 mW/cm^2. Figure 4.2 shows the wavelength distribution of the filtered source and the absorbance of MB. The MB concentration was monitored as a function of time by using transmission UV-visible spectroscopy to observe the decrease in the 610 nm MB peak (using a Thermo-Scientific Evolution 300 spectrophotometer). Photoluminescence experiments were conducted by recording the emission at 467 nm from the prepared photocatalysts as a function of excitation wavelength under ambient conditions using a Horiba Jobin Yvon FluoroMax-3 spectrofluorometer.

Two dimensional finite-difference time-domain (FDTD) optical simulations were performed to simulate the optical response of the materials as a function of the wavelength of incident photons. As discussed in Chapter 3, FDTD is a computational electro-dynamics modeling technique, which solves discretized Maxwell equations in space and time subject to the input geometry, material properties, and boundary conditions [38, 39]. The optical properties of plasmonic metals were represented using a Drude-Lorentz model [40–42] with empirical optical constants [43] which has been shown to give accurate results for Ag and Au nano-structures [44, 45]. Water was used as the background dielectric medium. All simulations were truncated in

all directions with the perfectly matched layer (PML) construct [38]. Incident radiation was supplied via a 200–1000 nm Gaussian source. Scattering, absorbance and extinction cross sections were calculated using the total-field/scattered-field (TFSF) formalism [38]; please refer to the Optical Simulations section of Chapter 3 for greater detail.

4.4 Results and Discussion

The rate of MB decomposition over various catalysts using the broadband illumination source with 500 nm short pass filter is shown in Figure 4.2b. As discussed above, the use of the filtered light source (no illumination above ∼500 nm) was important to prevent the direct photo-excitation of MB, in order to minimize photolysis or sensitization effects [31]. The lack of decomposition due to direct photolysis is confirmed by the blank results; i.e. there is no significant decomposition of MB under the same light source without a photocatalyst. Comparison of the TiO_2 and N-TiO_2 decomposition rates show that sensitization is also not a major contributor, since similar performance would be expected for both materials if the photosensitization effect dominated the performance. Figure 4.2 shows that the addition of Ag nanocubes significantly enhances the rate of MB decomposition over both TiO_2 and N-TiO_2. For example, the rate of MB decomposition on Ag/N-TiO_2 is approximately 4 times larger than the rate on N-TiO_2. We observed that the addition of Au nanostructures has little effect on the reaction rate.

To understand the results in Figure 4.2, we analyze optical and catalytic properties of the building blocks used in the experiments. First, Figure 4.2 shows that Ag and Au nanostructures by themselves exhibit no photo-catalytic activity under these operating conditions. Also, due to low doping with N [36], we can assume that

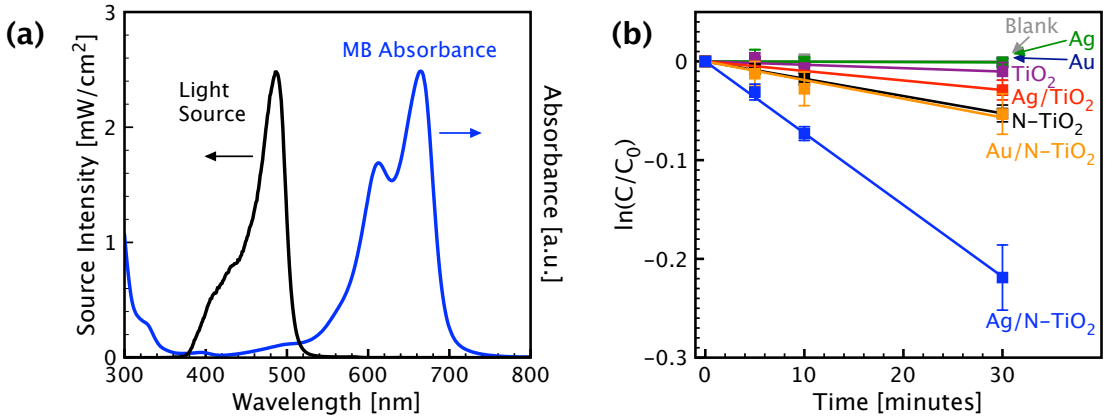

Figure 4.2: Methylene blue decomposition experiments. (a) Black curve: intensity of visible source with 500 nm short pass filter. Total intensity at the photocatalyst surface is 140 mW/cm^2. Blue curve: methylene blue absorption spectrum (arbitrary scale). (b) Aqueous phase MB decomposition over different photocatalysts: Ag cubes only (green), Au spheres only (dark blue), P25 TiO_2 only (purple), N-TiO_2 only (black), Ag/TiO_2 composite (red), Au/N-TiO_2 composite (orange) and Ag/N-TiO_2 (blue). The composite samples (Ag/TiO_2, Au/N-TiO_2, Ag/N-TiO_2) each contained 4.5 % metal particles by weight. All semiconductor-only and composite samples contained constant weight of semiconductor particles. The un-catalyzed (blank) photolysis of MB showed immeasurable decomposition (grey points).

the inherent capacity of TiO_2 and N-TiO_2 to support catalytic transformations by providing surface sites for reaction intermediates, are very similar to each other. This means we can assume that the difference in the performance of different composite materials is mainly a consequence of the difference in the optical properties of the building blocks contained in the composite photocatalysts rather than their inherent capacity to support chemical transformations. Very high dopant concentrations can cause decreased visible activity because of an increase in recombination centers, even though the absorption may increase, so we stress that this assumption is generally valid in the limit of low dopant concentration [36], as noted above.

The optical properties of the individual building blocks, measured as UV-vis extinction spectra, are shown in Figure 4.1. The figure shows that the TiO_2 extinction drops dramatically around 380 nm, whereas N-TiO_2 exhibits significant extinction intensity well into the visible region up to $\sim$ 500 nm. The extinction in semiconductors is the consequence of the absorption process, which results in the formation of excited charge carriers (e/h pairs). The formation of these carriers is responsible for photo-catalytic activity of both semiconductors. To understand the observed differences in MB decomposition rates on TiO_2 and N-TiO_2, we must look at the overlap of the semiconductor absorbance with the light source. The overlap is calculated by simply multiplying the light source spectrum (Figure 4.2a) with the semiconductor absorbance spectrum (Figure 4.1a). As shown in Figure 4.3, a small, but non-zero, overlap between the TiO_2 absorbance and light source is calculated, because the light source has photons down to approximately 375 nm and the absorbance of TiO_2 extends to approximately 410 nm. Since N-TiO_2 absorbs over a broader range of the visible source spectrum, it exhibits higher overlap with the visible light source, as shown in Figure 4.3. Furthermore, although there are not enough points in Figure

4.3 to draw definitive conclusions, it seems logical that these different semiconductor/source overlap values explain the observed differences in MB decomposition rates on the semiconductor-only samples.

Figure 4.1 also shows that the Ag nanocubes exhibit an extinction spectrum peaking at $\sim$ 450 nm and spreading +/- 100 nm. On the other hand, the Au spheres show extinction at $\sim$ 600 +/- 100 nm. For both metals, the main extinction peaks are due to excitation of SPR [6–9]. SPR is accompanied by intense oscillating electric fields that are a few orders of magnitude larger than the field associated with the source photons [9], which was shown in Chapter 2. SPR can be described as the resonant photon induced collective oscillation of valence electrons, established when the frequency of photons matches the natural frequency of surface electrons oscillating against the restoring force of positive nuclei. We note that the extinction below the main spectral features (below $\sim$500 nm for Au and below $\sim$325 nm for Ag) is due primarily to interband transitions, which are not critical to our discussion here [43, 46].

UV-vis extinction spectra for a few composite photo-catalysts are shown in Figure 4.1. The figure shows that the composite extinction is a superposition of the extinction due to the individual building blocks in the composite. The fact that the composite systems exhibit this behavior is an indication that there is no significant light-induced charge transfer from one building block to another, since charged semiconductor and plasmonic metals would exhibit additional extinction features [19, 47]. This is not surprising, considering that the metal and semiconductor building blocks are separated by nonconductive organic molecules chemisorbed on the surface of metal nanostructures and other studies have confirmed that this minimizes the amount of charge transfer possible at the semiconductor/metal interface [5, 48, 49].

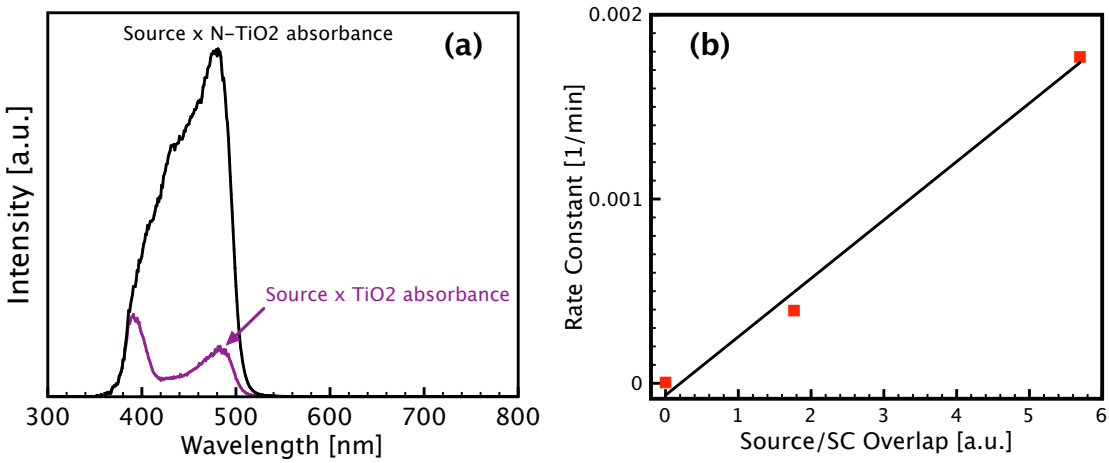

Figure 4.3: Source/semiconductor overlap explains difference in MB decomposition rates on different semiconductors. (a) Source/semiconductor absorbance overlap for N-TiO_2 (black curve) and TiO_2 (purple curve). (b) MB decomposition rate constant as a function of the overlap between illumination source and semiconductor absorbance. The source/semiconductor (SC) overlap is the area under the curve in (a). The three points are for the blank experiment (overlap = 0), TiO_2 sample (overlap $\sim$ 1.8) and N-TiO_2 sample (overlap $\sim$ 5.6).

Recently it has been suggested for similar plasmonic metal/semiconductor composite systems that the metal SPR-induced enhancement in the photo-catalytic activity of semiconductors is the consequence of the interaction of the SPR-induced intense oscillating electric field, concentrated around the metallic nanostructure (nanoparticles of Ag), and the nearby semiconductor [4, 5]. Essentially, the SPR-induced electric field increases the rate of e/h formation in the semiconductor, which in turn results in higher reaction rates. This supported by FDTD simulations showing enhanced absorption within a TiO_2 structure, due to local SPR-enhanced fields from a nearby Ag nanocube, shown in Figure 4.4a.

More importantly, this hypothesis is also supported experimentally by the comparison of composite samples containing Ag with those containing Au in Figure 4.2b. The Au nanostructures were chosen specifically because their plasmon resonance is not excited by the filtered light source. This is an important control experiment, which gives evidence to the mechanism of enhancement by the SPR-induced fields. Both metals facilitate charge transfer to a similar degree, but differ in the fact that the Ag SPR is excited by the light source while the Au SPR is not. This comparison suggests that the excitation of the Ag SPR (which is in resonance with the semiconductor absorbance) plays a crucial role in governing the enhancement. Essentially this gave us a way to turn on and off the SPR and investigate the effect on semiconductor activity.

Our hypothesis is also supported by a series of photoluminescence (PL) emission measurements performed under inert conditions. Photoluminescence spectroscopy involves measuring the emission of photons released from a material as electron/hole pairs re-combine [50–52]. There are essentially two ways that the rate of photon emission can be increased: (1) the rate of emission itself can be increased (with a

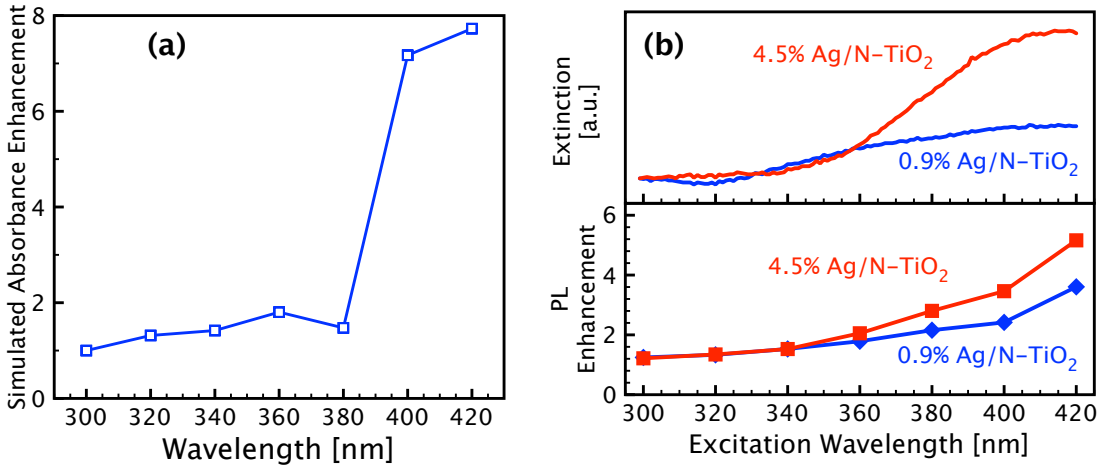

Figure 4.4: Simulated and measured enhancement in semiconductor absorption due to the presence of Ag SPR. (a) Simulated absorption enhancement in a TiO_2 structure due to the presence of a nearby excited Ag nanocube with 120-nm edge length. Power dissipation (see Chapter 3) was calculated in a 4 nm^2 area of the TiO2 structure near the TiO_2/liquid interface with and without the presence of a nearby 120-nm Ag cube. Absorption enhancement was then defined as the calculated power dissipation for the TiO_2 with Ag simulation divided by that of the simulation without Ag. (b) Top: Ag difference spectra (DRUV spectra of composite systems minus that of N-TiO_2); original DRUV spectra are given in Figure 4.1. Bottom: Enhancement of photoluminescence (PL) emission at 467 nm as a function of excitation wavelength. PL enhancement is calculated by dividing the emission for composite Ag/N-TiO_2 systems by the emission for N-TiO_2 at the same excitation wavelength. For example, the value of PL enhancement at 400 nm is defined as emission from the Ag/N-TiO_2 sample upon excitation at 400 nm, divided by emission from the N-TiO_2 upon excitation at 400 nm (emission is measured at 467 nm in all cases).

constant rate of e/h excitation), this is referred to as "emission enhancement" or (2) the rate of e/h pair formation can be enhanced while the inherent emission probability is unchanged, referred to as "excitation enhancement" (both processes can also occur at the same time) [48, 49]. It has been shown that both processes can be enhanced by the addition of excited plasmonic particles [48, 49]. It is important to note that for a given system, the emission enhancement due to SPR-enhanced fields for a given emission wavelength is independent of the excitation wavelength [48, 49]. This is because the emission enhancement at a particular emission wavelength depends only on the intensity of SPR-induced electric fields at the emission wavelength ($|E|^2_{em}$). This quantity is constant as a function of excitation wavelength because it depends only on the number of SP states available at the emission wavelength (which does not change if the source wavelength is changed). On the other hand, excitation enhancement depends on the intensity of SPR-induced fields at the excitation wavelength ($|E|^2_{em}$), which does change with changing source wavelength.

In these studies the intensity of the 467-nm TiO_2 emission peak was measured as a function of excitation wavelength for semiconductor-only and composite photocatalysts. PL emission enhancements for two composite Ag/N-TiO_2 photocatalysts are plotted as a function of the excitation wavelength in Figure 4.4b (bottom). PL enhancement is calculated by dividing the emission for a composite Ag/N-TiO_2 system by the emission for N-TiO_2 at the same excitation wavelength. For example, the value of PL enhancement at 400 nm is defined as emission from the Ag/N-TIO_2 sample upon excitation at 400 nm, divided by emission from the N-TiO_2 upon excitation at 400 nm (emission is measured at 467 nm in all cases). Figure 4.4b shows that the emission enhancement tracks the intensity of Ag SP states (Figure 4.4b, top), i.e. the highest emission is observed for excitation wavelengths that maximize the

intensity of SPR. Since the emission enhancements are affected by the source wavelength, the increase in the emission is assigned to the metal SPR-induced increase in the rate of e/h formation in the semiconductor of the composite material [5, 48, 49], as discussed above.

Below in this text we attempt to quantify the interaction of the metal SPR-induced electric field with the nearby semiconductor and in doing so relate the optical properties of metal and semiconductor building blocks to the photo-catalytic activity of the composite photo-catalysts. For a plasmonic metal to enhance the rate of e/h formation in the nearby semiconductor and therefore to increase the photo-catalytic rates, the metal SPR–induced oscillating electric field must efficiently channel sufficient energy (i.e., the minimum energy required to overcome the band gap) into the nearby semiconductor. This essentially means that the there has to be an overlap between the metal SPR spectrum and the semiconductor absorption spectrum. Furthermore, since SPR is a resonant phenomenon, an excitation of SPR requires an overlap between the source spectrum and the metal SPR extinction spectrum. This explains why the addition of Au does not enhance the activity of TiO_2 or N-TiO_2. Au has been shown to enhance the activity of a semiconductor when the Au SPR is excited and overlaps in energy with the semiconductor absorbance [24, 25]. However, in the current system the Au SPR ($\sim$500–600 nm) is not excited by the light source ($\sim$375–500 nm) and is also not resonant with the absorbance of TiO_2 (below $\sim$400 nm) or N-TiO_2 (below $\sim$500 nm).

This analysis suggests that for a given composite geometry, mainly an equal spacing between individual building blocks in different composite photocatalysts, the relative reaction rate enhancement on composite photocatalysts should be proportional to the optical overlap between the illumination source spectrum, the metal

SPR (i.e., the extinction spectrum of the metallic building block), and the absorption spectrum of the semiconductor (illustrated in Figure 4.5). This is expressed by the simple relationship shown in Equation 4.1.

$$\text{RateEnhancement} \propto \text{OpticalOverlap} = \int I_0(\lambda) A_{SC}(\lambda) E_{SPR}(\lambda) \tag{4.1}$$

Where I_0 is the wavelength-dependent source spectrum, A_{SC} is the semiconductor absorbance spectrum and E_{SPR} is the metal nanoparticle extinction arising from excitation of SPR. This relationship assumes a constant composite material geometry (e.g. a simple homogeneous mixture of metal and semiconductor particles). The use of macroscopically observable extinction spectra as an approximation to capture the near-field behavior of the system, thereby providing a quick and scalable method to evaluate potential composite materials, is reasonable for comparing systems with the same geometry because an increase in local SPR-induced fields directly results in increased extinction. This is confirmed by the results of FDTD simulations shown in Figure 4.6, which show that the far-field properties of the system (spectra) qualitatively capture relative changes in the magnitude of the near-field effects. These results were obtained by calculating the average intensity of the electric field (i.e., the average strength of the near-field effect) at 450 nm for Ag spheres and Ag cubes of different sizes, and comparing this to the simulated far-field extinction spectra.

We note that Equation 4.1 also assumes geometric overlap between the SPR-induced electric fields and the semiconductor particles. If there were no spatial overlap between the SPR-induced fields and semiconductor in a composite system, there could be no rate enhancement from SPR-induced fields. Additionally, if the amount of spatial overlap between SPR-induced fields and semiconductor changed between systems (e.g. by changing particle geometry), then the system behavior would not necessarily be captured by the far field properties. We will comment more

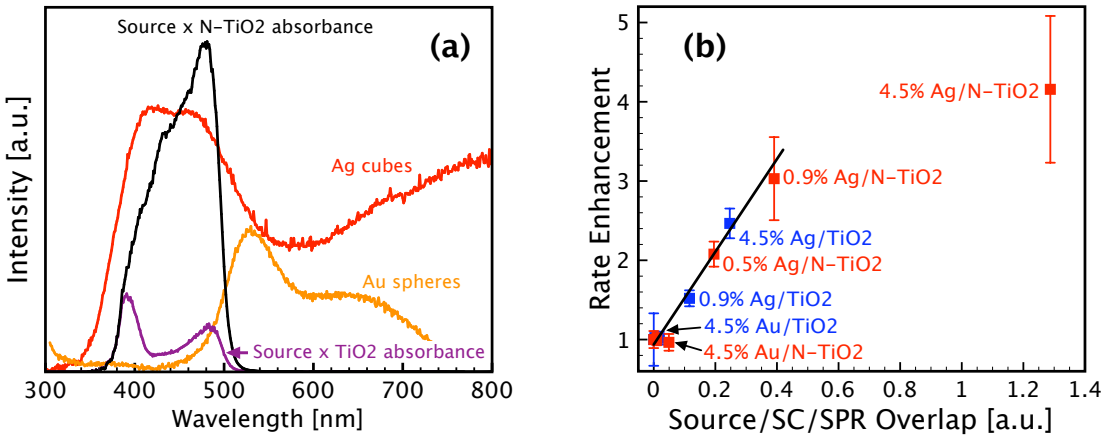

Figure 4.5: Experimental overlap of source spectrum, semiconductor absorbance and metal SPR. (a) Source/semiconductor absorbance overlap for N-TiO_2 (black curve) and TiO_2 (purple curve) and metal nanoparticle spectra (see Figure 4.3b) for 4.5% Ag and 4.5% Au. (b) Enhancement in the MB decomposition rate as a function of the overlap between illumination source, semiconductor absorbance and metal nanoparticle SPR. Blue points shows native TiO_2-based composites and red points show N-TiO_2-based composites.

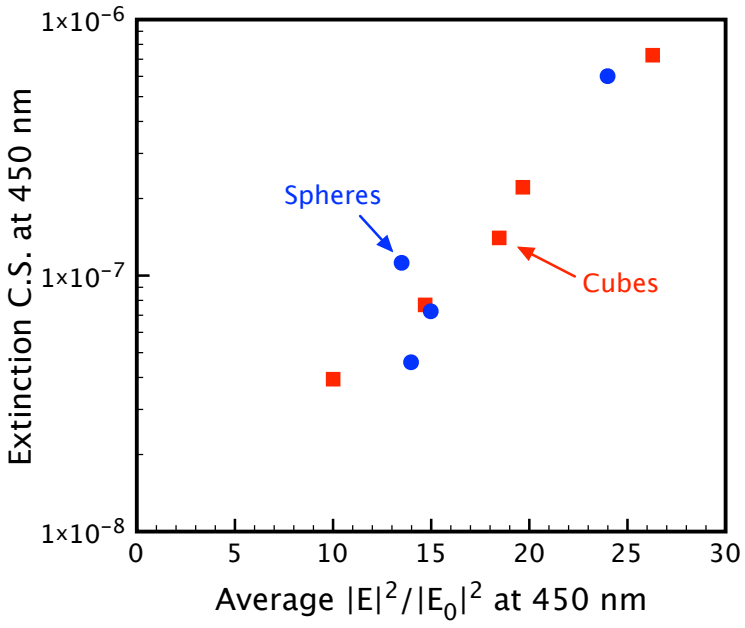

Figure 4.6: Comparison of averaged near-field intensity measurements and far-field spectra from FDTD simulations. The simulated extinction cross-section at 450 nm (in meters) is plotted as a function of the average local field intensity at 450 nm for a series of Ag spheres (blue points) and Ag cubes (red points). Cube sizes were 20, 30, 40, 50 and 100 nm edge length. Sphere sizes were 30, 40, 50 and 100 nm diameter. The average local field intensities were calculated by averaging the fields 1 nm away from the surface of the Ag structures.

below on the issue of the nano-scale geometric arrangement of composite building blocks.

To test the relationship in Equation 4.1, in Figure 4.5b we plotted the MB photo-decomposition rate enhancement as a function of the optical overlap between light source, semiconductor absorbance and metal SP states, for a range of tested photo-catalysts. The rate enhancement is calculated as the measured MB decomposition rate (see Figure 4.2) for a composite system divided by the rate for the semiconductor-only (e.g. Ag/N-TiO_2 compared to N-TiO_2 and Ag/TiO_2 compared to TiO_2). The optical overlap was calculated, as shown in Equation 4.1, by multiplying the illumination source spectrum (Figure 4.2) the semiconductor absorbance spectrum (Figure 4.1) and the metal nanoparticle extinction spectrum (Figure 4.1), and integrating over the entire wavelength range (300–800 nm). The rate enhancement for a pure semiconductor is unity by definition and the optical overlap for a pure semiconductor is defined as zero (since there are no SP states). Figure 4.5b shows that for a given geometry of composite photocatalysts (with similar inherent catalytic activity) the optical overlap, as defined in Equation 4.1, is linearly related to the activity of composite plasmonic metal/semiconductor photo-catalysts. The exception to this is for high Ag loading, which significantly under-performs the otherwise linear trend. This is not surprising considering that high Ag loading results in high overall extinction of the composite photocatalyst, which can shift the overall process into a light-limited reaction regime, i.e., the entire reactor volume is not exposed to light.

The relationship presented in Equation 4.1 and validated experimentally in Figure 4.5b can be used to guide the design of composite photo-catalysts. For example, the intensity and wavelength of metal SPR can be manipulated by changing the

composition, shape, size or dieletric environment of metal nanoparticles [7, 8, 53]. Plasmonic nano-particles of noble metals can be tuned to exhibit SPR spanning the entire near-UV/visible/near-IR spectrum [54, 55]. It is beneficial to be able to identify, a priori, the plasmonic nanostructures that would yield the maximum enhancements in reaction rates on a given semiconductor. In this context, optical simulation techniques (e.g. the FDTD method) provide a very useful tool, since the optical properties of any arbitrary metal nanoparticle geometry can be calculated with reasonable accuracy using these simulations.

We have used the model in Equation 4.1 to probe the effect of metal particle size, shape, and composition on the photochemical activity of a model semiconductor that absorbs light with wavelengths below 550 nm. In these studies, the absorbance of a semiconductor was modeled using a step function with full absorbance below 550 nm and no absorbance above 550 nm (see Figure 4.7). The metal SPR spectra were evaluated by calculating the extinction efficiency (extinction cross-section divided by particle volume) using the FDTD optical simulations. Using the calculated extinction efficiency (rather than extinction cross-section) in the model allows for comparison of nanoparticle performance on per volume (or per weight) basis. The illumination source spectrum for these calculations was the AM1.5 solar spectrum (National Renewable Energy Laboratory (NREL), http://rredc.nrel.gov/solar/spectra/am1.5/). The optical overlap, which is proportional to the reaction rate enhancement, was evaluated as in Equation 4.1. The lower limit of integration was the wavelength below which interband transitions, rather than SPR, dominate the metal extinction spectra ($\sim$325 nm for Ag and $\sim$490 nm for Au) [54, 56]; the upper limit was 800 nm.

Figure 4.8 shows the calculated optical overlap as a function of particle size (sphere diameter or cube edge length) for three different plasmonic nanoparticles: Ag spheres,

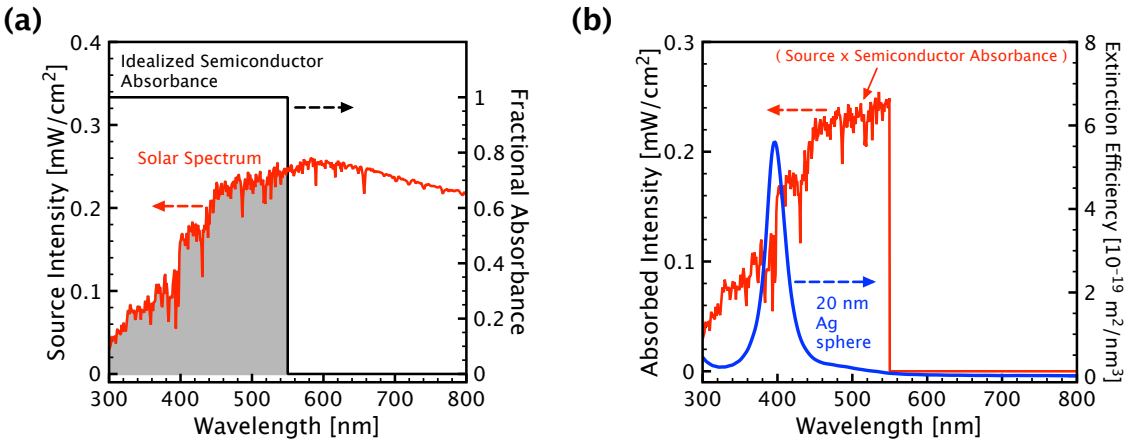

Figure 4.7: Theoretical model constructed from overlap of source intensity, semiconductor absorbance and metal SPR spectrum. (a) Intensity of the solar spectrum (left ordinate) and fractional absorbance of an idealized SC with band gap of 550 nm (right ordinate). AM1.5 solar spectrum data are from the National Renewable Energy Laboratory (NREL), http://rredc.nrel.gov/solar/spectra/am1.5/. The product of the two curves (shaded area) gives the number of photons absorbed by the SC as a function of wavelength. (b) Product of source intensity and SC absorbance, shown as the shaded area in Figure 4.7a (left ordinate), and simulated extinction (SPR) efficiency for a 20-nm Ag sphere (right ordinate). Extinction efficiency is defined herein as the extinction cross-section (calculated from FDTD simulation) for a particle divided by the physical volume of the particle. Source/SC/SPR overlap is calculated by multiplying the two curves in Figure 4.7b and integrating from the metal interband transition wavelength (325 nm for Ag and 490 nm for Au) to 800 nm.

Ag cubes and Au spheres. In general, large Ag cubes (edge length of ∼120 nm) and smaller Au spheres (edge length 50 nm) have the highest overlap with the 550 nm band gap semiconductor under solar illumination. We anticipate that these plasmonic nanostructures should show the highest photo-catalytic rate enhancement. Figure 4.8 also indicates that for a 550 nm band gap semiconductor under solar illumination Au spheres should out-perform Ag spheres for a broad range of sizes. This is primarily due to the difference in SPR wavelengths for Ag and Au. For small spheres, the Ag SPR is centered around 390 nm where the solar illumination has relatively low intensity (see Figure 4.7), while the Au SPR is centered around 550 nm where the illumination is much more intense. Ag cubes generally out-perform Au spheres primarily because, for a given particle size and composition, cubic nanoparticles intrinsically have much larger extinction efficiency [5]. In addition, the spectra for cubes are generally broader than for spheres, which increases overlap.

While Figure 4.8 specifically focuses on a semiconductor with 550 nm band gap under solar illumination, the method we have detailed allows extension to any semiconductor and light source. For example, by simply changing the band gap of our idealized semiconductor from 550 nm to any value, we can determine which metal nanostructures are promising for any given semiconductor band gap under solar illumination. The results of this analysis are shown in Figures 9 for Ag spheres (left), Ag cubes (middle) and Au spheres (right), which display the calculated optical overlap for a given metal particle (composition, shape and size) as a function of the semiconductor band gap.

Figure 4.9 shows that for semiconductors with large band gap (∼ 3 eV), small Ag nanostructures exhibit the highest overlap integral and should lead to the largest enhancements in reactions rates. The main reason for this is relatively high intensity

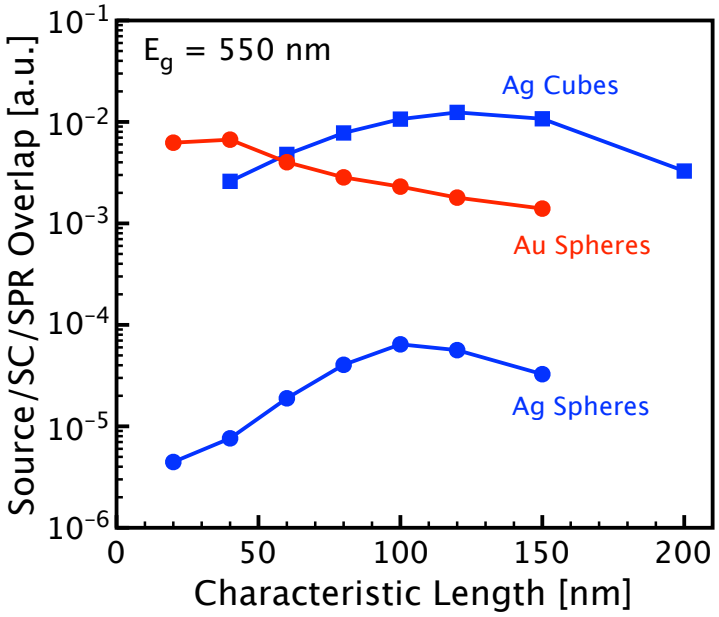

Figure 4.8: Model predicted overlap values under solar illumination as a function of particle size. Calculated source/SC/SPR overlap integral as a function of the characteristic length (diameter for spheres and edge length for cubes) of plasmonic nanoparticles for an idealized SC with band gap of 550 nm. The light source was the the AM1.5 solar spectrum (data from the National Renewable Energy Laboratory (NREL), http://rredc.nrel.gov/solar/spectra/am1.5/).

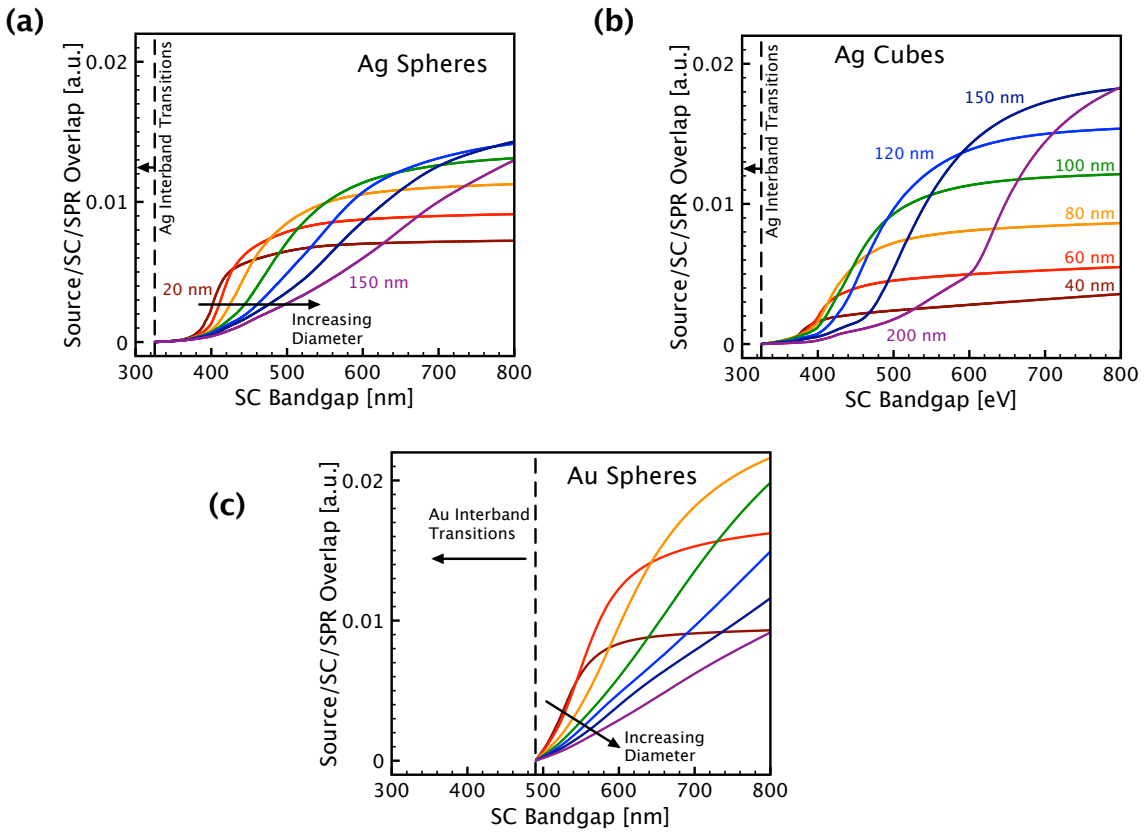

Figure 4.9: Calculated source/SC/SPR overlap integral as a function of semiconductor band gap. Illumination source was the AM1.5 solar spectrum (data from the National Renewable Energy Laboratory (NREL), http://rredc.nrel.gov/solar/spectra/am1.5/), for (a) Ag spheres with varying diameters, (b) Ag cubes with varying edge length and (c) Au spheres with varying diameters. Cube edge lengths are labeled in Figure 4.9b. Sphere diameters in Figures 9a and 9c are 20, 40, 60, 80 100, 120 and 150 nm. The overlap quantity is not calculated at wavelengths lower than the metal interband transition (325 nm for Ag and 490 nm for Au).

of SPR of these Ag nanostructures under UV light. For semiconductors with small band gap, fairly large Ag and smaller Au nanostructures show the most promise. It is important to reiterate that this analysis applies for composite systems with identical geometries (building blocks are position identical with respect to each other). We also assume that the rate of parasitic loss of e/h due to the presence of the metal surface is similar irrespective of the size, shape, or composition of the plasmonic metal particles. While we have focused on three specific metal nanoparticle examples, the model is easily extended to any metal composition, shape and size with the only necessary input being the inclusion of the appropriate bulk metal optical properties in the FDTD simulations (i.e. the complex dielectric function which can be fit using, for example, a Drude-Lorentz model) [57].

The optical overlap integral in Equation 4.1 represents a simple predictor allowing us to identify optimal semiconductor/plasmonic metal combinations based only on the far-field optical properties of the building blocks (extinction spectra). However, the model cannot separate the effects of the near-field electromagnetic enhancement mechanism and the far-field scattering mechanism discussed above and in Chapter 2. As mentioned, the scattering mechanism is generally observed to play a relatively minor role in similar systems; however, both mechanisms are dependent on the metal SPR and both are expected to play a role. Furthermore, as we have discussed above, an increase in the average intensity of local near-fields around a plasmonic particle are captured (at least quantitatively) by the far-field spectra. This raises the question: how can the near-field mechanism be responsible for enhancements above and beyond that predicted by the scattering mechanism? At this point, the near-field mechanism has not been directly probed experimentally and there is no clear answer to this question.

It is also important to reiterate that the model in Equation 4.1 does not give insights into the most favorable arrangement (geometries) of the constituent building blocks with respect to each other. The SPR-induced electric fields around a plasmonic metal particle vary greatly throughout space around the particle. For example, for an isolated cube the SPR-induced fields are concentrated at the corners of the cube, and the arrangement of particle aggregates has a large effect on the spatial distribution of fields. The consequence of this is that the SPR-induced enhancement in charge carrier generation in a semiconductor is not constant throughout space [22], which is discussed in the next chapter. Optimal designs of composite photocatalysts will require controlling not only the macroscopic optical properties as discussed herein, but also the nano-scale geometric arrangement of building blocks, see Chapter 6.

4.5 Conclusions

We demonstrated the design of a composite plasmonic metal/semiconductor photocatalysts that show enhanced photocatalytic activity compared to the semiconductor alone. The enhancement could not be explained simply by invoking only direct MB photolysis (present to the same degree in all samples) or dye sensitization of the semiconductor (present to the same degree in all semiconductor-only and metal/semiconductor composite samples). The observed photo-catalytic activity enhancement is attributed to metal SPR, which can increase the rate of formation of charge carriers within the semiconductor. We showed that the optical overlap between the illumination source spectrum, semiconductor absorbance spectrum and metal nanoparticle SPR spectrum provides a useful descriptor for predicting the SP-induced rate enhancement for composite photocatalysts of similar geometries (specifically, similar arrangements of the nano-sized building blocks), and guiding

the formulation of optimal plasmonic metal/semiconductor photocatalysts.

References

[1] Linsebigler, A. L.; Lu, G.; Yates, Jr., J. T. *Chem. Rev.* **1995**, *95*, 735–758.

[2] Fujishima, A.; Rao, T. N.; Tryk, D. A. *J. Photochem. Photobio. C* **2000**, *1*, 1–21.

[3] Fujishima, A.; Zhang, X.; Tryk, D. A. *Surf. Sci. Rep.* **2008**, *63*, 515–582.

[4] Awazu, K.; Fujimake, M.; Rockstuhl, C.; Tominaga, J.; Murakami, H.; Ohki, Y.; Yoshida, N.; Watanabe, T. *J. Am. Chem. Soc.* **2008**, *130*, 1676–1680.

[5] Christopher, P.; Ingram, D. B.; Linic, S. *J. Phys. Chem. C* **2010**, *114*, 9173–9177.

[6] El-Sayed, M. A. *Acc. Chem. Res.* **2001**, *34*, 257–264.

[7] Burda, C.; Chen, X.; Narayanan, R.; El-Sayed, M. A. *Chem. Rev.* **2005**, *105*, 1025–1102.

[8] Kelly, K. L.; Coronado, E.; Zhao, L. L.; Schatz, G. C. *J. Phys. Chem. B* **2003**, *107*, 668–677.

[9] Brus, L. *Acc. Chem. Res.* **2008**, *41*, 1742–1749.

[10] Govorov, A. O.; Zhang, W.; Skeini, T.; Richardson, H.; Lee, J.; Kotov, N. A. *Nanoscale Res. Lett.* **2006**, *1*, 84–90.

[11] Hoepfner, M. P.; Roper, D. K. *J. of Anal. Cal.* **2009**, *98*, 197–202.

[12] Adleman, J. R.; Boyd, D. A.; Goodwin, D. G.; Psaltis, D. *Nano Lett.* **2009**.

[13] Subramanian, V.; Wolf, E.; Kamat, P. V. *J. Phys. Chem. B* **2001**, *105*, 11439–11446.

[14] Arabatzis, I. M.; Stergiopoulos, T.; Bernard, M. C.; Labou, D.; Neophytides, S. G.; Falaras, P. *Appl. Catal. B* **2003**, *42*, 187–201.

[15] Subramanian, V.; Wolf, E. E.; Kamat, P. V. *J. Am. Chem. Soc.* **2004**, *126*, 4943–4950.

[16] Silva, C. G.; Juárez, R.; Marino, T.; Molinari, R.; García, H. *J. Am. Chem. Soc.* **2011**, *133*, 595–602.

[17] Primo, A.; Corma, A.; García, H. *Phys. Chem. Chem. Phys.* **2011**, *13*, 886–910.

[18] Tian, Y.; Tatsuma, T. *Chem. Comm.* **2004**, 1810–1811.

[19] Tian, Y.; Tatsuma, T. *J. Am. Chem. Soc.* **2005**, *127*, 7632–7637.

[20] Kowalska, E.; Mahaney, O. O. P.; Abe, R.; Ohtani, B. *Phys. Chem. Chem. Phys.* **2010**, *12*, 2344–2355.

[21] Primo, A.; Marino, T.; Corma, A.; Molinari, R.; García, H. *J. Am. Chem. Soc.* **2011**.

[22] Ingram, D. B.; Linic, S. *J. Am. Chem. Soc.* **2011**, *133*, 5202–5205.

[23] Kumar, M. K.; Krishnamoorthy, S.; Tan, L. K.; Chiam, S. Y.; Tripathy, S.; Gao, H. *ACS Catal.* **2011**, *1*, 300–308.

[24] Liu, Z.; Hou, W.; Pavaskar, P.; Aykol, M.; Cronin, S. B. *Nano Lett.* **2011**, *11*, 1111–1116.

[25] Hou, W.; Liu, Z.; Pavaskar, P.; Hung, W. H.; Cronin, S. B. *J. Catal.* **2011**, *277*, 149–153.

[26] Derkacs, D.; Lim, S. H.; Matheu, P.; Mar, W.; Yu, E. T. *Appl. Phys. Lett.* **2006**, *89*, 093103.

[27] Pala, R. A.; White, J.; Barnard, E.; Liu, J.; Brongersma, M. L. *Adv. Mater.* **2009**, *21*, 1–6.

[28] Atwater, H. A.; Polman, A. *Nat. Mater.* **2010**, *9*, 205–213.

[29] Mills, A.; Wang, J. *J. Photochem. Photobio. A* **1999**, *127*, 123–134.

[30] Houas, A.; Lachheb, H.; Ksibi, M.; Elaloui, E.; Guillard, C.; Herrmann, J.-M. *Appl. Catal. B* **2001**, *31*, 145–157.

[31] Yan, X.; Ohno, T.; Nishijima, K.; Abe, R.; Ohtani, B. *Chem. Phys. Lett.* **2006**, *429*, 606–610.

[32] Ohtani, B. *Chem. Lett.* **2008**, *37*, 217–229.

[33] Ohtani, B. *J. Photochem. Photobio. C* **2010**, *11*, 157–178.

[34] Grätzel, M. *Nature* **2001**, *414*, 338–344.

[35] Youngblood, W. J.; Lee, S.-H. A.; Kobayashi, Y.; Hernandez-Pagan, E. A.; Hoertz, P. G.; Moore, T. A.; Moore, A. L.; Gust, D.; Mallouk, T. E. *J. Am. Chem. Soc.* **2009**, *131*, 926–927.

[36] Irie, H.; Watanabe, Y.; Hashimoto, K. *J. Phys. Chem. B* **2003**, *107*, 5483–5486.

[37] Christopher, P.; Linic, S. *ChemCatChem* **2010**, *2*, 78–83.

[38] Taflove, A.; Hagness, S. C. *Computational Electrodynamics: The Finite-Difference Time-Domain Method*; Artech House: Boston, 2005.

[39] McMahon, J. M. Ph.D. thesis, Northwestern University: Evanston, Illinois, 2010.

[40] Wooten, F. *Optical Properties of Solids*; Academic: New York, 1972.

[41] Ashcroft, N. W.; Mermin, N. D. *Solid State Physics*; Brooks Cole, 1976.

[42] Lee, T.-W.; Gray, S. K. *Optics Express* **2005**, *13*, 9652–9659.

[43] Palik, E. D. *Handbook of Optical Constants of Solids*; Academic Press: New York, 1985.

[44] Link, S.; El-Sayed, M. A. *J. Phys. Chem. B* **1999**, *103*, 8410–8426.

[45] McMahon, J. M.; Wang, Y.; Sherry, L. J.; Van Duyne, R. P.; Marks, L. D.; Gray, S. K.; Schatz, G. C. *Journal of Physical Chemistry C* **2009**, *113*, 2731–2735.

[46] Pinchuk, A.; von Plessen, G.; Kreibig, U. *J. Phys. D: Appl. Phys.* **2004**, *37*, 3133–3139.

[47] Kamat, P. V. *Journal of Physical Chemistry B* **2002**, *106*, 7729–7744.

[48] Lee, J.; Govorov, A. O.; Dulka, J.; Kotov, N. A. *Nano Lett.* **2004**, *4*, 2323–2330.

[49] Lee, J.; Javed, T.; Skeini, T.; Govorov, A. O.; Bryant, G. W.; Kotov, N. A. *Angew. Chem. Int. Ed.* **2006**, *45*, 4819–4823.

[50] Anpo, M.; Tomonari, M.; Fox, M. A. *J. Phys. Chem.* **1989**, *93*, 7300–7302.

[51] Zhang, W. F.; Zhang, M. S.; Yin, Z.; Chen, Q. *Applied Physics B* **2000**, *70*, 261–265.

[52] Jung, K. Y.; Park, S. B.; Anpo, M. *J. Photochem. Photobio. A* **2005**, *170*, 247–252.

[53] Linic, S.; Christopher, P. *ChemCatChem* **2010**, *2*, 1061–1063.

[54] Rycenga, M.; Cobley, C. M.; Zeng, J.; Li, W.; Moran, C. H.; Zhang, Q.; Qin, D.; Xia, Y. *Chem. Rev.* **2011**.

[55] Xia, Y.; Xiong, Y.; Lim, B.; Skrabalak, S. E. *Angew. Chem. Int. Ed.* **2009**, *48*, 60–103.

[56] Hou, W.; Hung, W. H.; Pavaskar, P.; Goeppert, A.; Aykol, M.; Cronin, S. B. *ACS Catal.* **2011**, *1*, 929–936.

[57] Lee, J.; Govorov, A. O.; Kotov, N. A. *Angew. Chem. Int. Ed.* **2005**, *44*, 7439–7442.

CHAPTER 5

Plasmon-Enhanced Water Splitting

5.1 Summary

A critical factor limiting the rates of photocatalytic reactions, including water splitting, on oxide semiconductors is high rates of charge carrier recombination. In this contribution we demonstrate that this issue can be alleviated significantly by combining a semiconductor photocatalyst with tailored plasmonic metal nanostructures. Plasmonic nanostructures support the formation of resonant surface plasmons in response to a photon flux, localizing electromagnetic energy close to their surface. We present evidence that the interaction of localized electric fields with neighboring semiconductor allows for the selective formation of e^-/h^+ pairs in the near surface region of the semiconductor. The advantage of the formation of e^-/h^+ pairs in the semiconductor surface is that these charge carriers are separated from each other readily, and that they migrate to the surface easily where they can perform a photocatalytic transformation.

5.2 Introduction

The efficient conversion of solar energy into fuels through the photochemical splitting of water to form H_2 and O_2 is of critical importance for the development of a sustainable energy future. It has been demonstrated that various oxide semiconductors

are active photocatalysts for this reaction [1–4], which is usually carried out in a photoelectrochemical (PEC) cell (see Chapter 2). In these systems, the semiconductor is applied to a conductive substrate and this assembly forms the photo-anode (working electrode). When illuminated with energy exceeding the band gap are absorbed, excited charge carriers (electron/hole pairs) are formed in the semiconductor. For an n-type semiconductor (most of the common oxide materials), energetic holes diffuse to the semiconductor/liquid interface and drive the oxygen evolution half-reaction ($H_2O + 2h^+ \longrightarrow 2H^+ + 1/2O_2$). Energetic electrons diffuse away from the semiconductor/liquid interface to the conductive substrate (current collector). The electrons are conducted around an external circuit to a counter electrode (typically Pt), where they drive the hydrogen evolution half-reaction ($2H^+ + 2e^- \longrightarrow H_2$). Figure 5.1 shows a sketch of these processes; for more detailed discussion refer to Chapter 2. The net effect is that the energy of UV-vis photons is used to drive this highly endothermic chemical transformation (2.46 eV per H_2O molecule or ΔG = 237 kJ/mol), essentially allowing for the deposition and storage of energy from light into the energy of chemical bonds.

A crucial obstacle limiting the efficiency of almost every oxide semiconductor photocatalyst is the high rate of charge carrier (e^-/h^+) recombination [5–9]. Photons typically have a penetration depth in oxides on the order of hundreds of nanometers to microns (depending on the composition and morphology). On the other hand, bulk charge carriers typically have mean free paths (i.e. average distance a charge carrier can travel within the material before being consumed) on the order of one to tens of nanometers [8]. This means that most charge carriers are formed within the bulk of the material, with a distance to the surface that surpasses the charge carrier mean free path. The consequence of this discrepancy is that a majority of

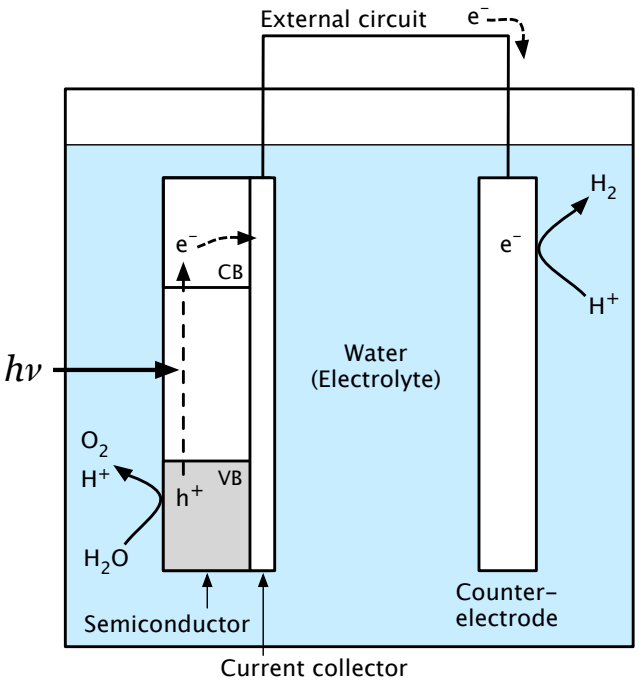

Figure 5.1: Photoelectrochemical cell system for production of H_2 and O_2 from water. Processes for an n-type semiconductor are shown. When illuminated with photons of energy exceeding the band gap, excited charge carriers are formed in the semiconductor photoanode. The holes diffuse to the semiconductor surface and drive the oxygen evolution half-reaction ($2H_2O + 4h^+ \longrightarrow O_2 + 4H^+$). Electrons are collected and travel to the counter electrode where they drive the hydrogen evolution half-reaction ($2H^+ + 2e^- \longrightarrow H_2$).

charge carriers are lost to recombination before reaching the semiconductor surface and performing photochemical reactions. Attempts to address this problem have primarily fallen into three categories: (1) controlling the photocatalyst structure so that photon absorption can be maximized while minimizing the distance charge carriers travel before reaching the surface [10–13], (2) improving charge mobility within the semiconductor bulk by adding mobility-promoting dopants [3, 14] or (3) partially alleviating the rate of bulk recombination by improving crystallinity (grain boundaries can act as charge carrier traps) [10].

In this chapter we demonstrate that the recombination problem can be alleviated significantly by combining an oxide semiconductor photocatalyst with tailored plasmonic metal nanostructures. There are several potentially relevant mechanisms, as discussed in Chapters 2 and 4. Plasmonic nanostructures support the formation of resonant surface plasmons (SP) in response to a photon flux, localizing very intense electromagnetic (EM) fields close to their surface [15–17]. When a semiconductor is brought into the proximity of a photo-excited plasmonic nanostructure it encounters these intense EM fields. Since the rate of e^-/h^+ formation in a semiconductor is proportional to the local intensity of the electric field (more specifically $|E|^2$) [18, 19], the rate of e/h formation in the semiconductor is enhanced if the energy of the SPR is sufficient to excite the semiconductor absorbance. As demonstrated in Chapter 2, the SP states can be tuned by tailoring the selection of metal particle composition, shape and size. This allows for plasmonic metal particles where the overlap of the SP states overlap with the semiconductor absorbance and light source.

The potential impact of this near-field electromagnetic enhancement mechanism is that, because the SPR-induced fields are most intense near the semiconductor surface, the enhancement in e/h formation may be the greatest at the semiconductor

surface. This has previously been suggested based on electrodynamics simulations, which show the enhanced fields near excited plasmonic particles [20–24], but direct experimental evidence has not been obtained. In this chapter we present experimental evidence that the interaction of localized electric fields with a neighboring semiconductor allows for the selective formation of e^-/h^+ pairs in the near surface region of the semiconductor. The charge carriers formed near the semiconductor surface reach the active surface sites more readily than charge carriers formed in the bulk. This results in a decrease of the charge carrier recombination rate and increases the water splitting rate on composite photocatalysts that contain plasmonic metal and a semiconductor.

Our conclusions were obtained in studies of the water splitting reaction under broadband visible light illumination in a conventional three-electrode PEC cell. A few previous examples of similar photo-catalysts have focused on photo-induced exothermic reactions such as photo-oxidation of methylene blue or other organic compounds [20, 21, 25–27]. The reversible nature of the water splitting reaction makes this process mechanistically different and potentially more sensitive to local surface concentrations of charge carriers than the exothermic photo-induced reactions. The photo-electrode for the O_2 evolution reaction in these studies was nitrogen-doped TiO_2 (N-TiO_2) or a composite material containing Ag nanocubes (edge length 118 ± 25 nm) or Au spheres (diameter 24.5 ± 4.5 nm) with N-TiO_2. Unlike native TiO_2, N-TiO_2 is optically active in the visible region of the solar spectrum as shown in Figure 5.2 [28–31]. We focused on these nanoparticle sizes because, as discussed in Chapter 4, the optimum plasmonic nanostructure for N-TiO_2 is moderate sized Ag nanocubes ($\sim$100–120 nm edge length). This is also corroborated by the simulation results shown in Figure 5.2, where the extinction efficiencies (averaged

over 400–500 nm source wavelength), are shown. Extinction efficiency is defined as the extinction cross-section, calculated using finite-difference time-domain (FDTD) simulations [32], divided by the geometric cross-section. The extinction is the consequence of the formation of resonant Ag SP states. Small spherical Au nanoparticles were also selected for use in control experiments. Au conductivity and electronic structure are similar to Ag; however, the Au SPR is red-shifted compared to Ag and it does not overlap significantly with N-TiO_2 absorption spectrum as shown in Figure 5.2.

5.3 Methods

Optical simulations were implemented using the finite-difference time-domain (FDTD) method in three spatial dimensions. FDTD is a computational electrodynamics modeling technique, which solves discretized Maxwell equations in space and time subject to the input geometry, material properties, and boundary conditions [32, 33]. The optical properties of Ag were represented using a Drude-Lorentz model [34, 35] with empirical optical constants [36], which has been shown to give accurate results for Ag and Au nano-structures [37, 38]. Water was used as the background dielectric medium by specifying a constant background index of refraction of 1.33. The simulation geometry comprised a single particle (Ag cube or Au sphere) sitting on a slab of SiO_2 (1.5 index of refraction); the SiO_2 slab was continuous in the x- and y-directions and 200 nm thick in the z-direction. All simulations were periodic in the x- and y-directions, while the perfectly matched layer (PML) construct [32] was used to truncate the simulations in the positive and negative z-directions. Incident radiation was supplied via a 300–800 nm Gaussian source.

Scattering, absorbance and extinction cross sections were calculated using the

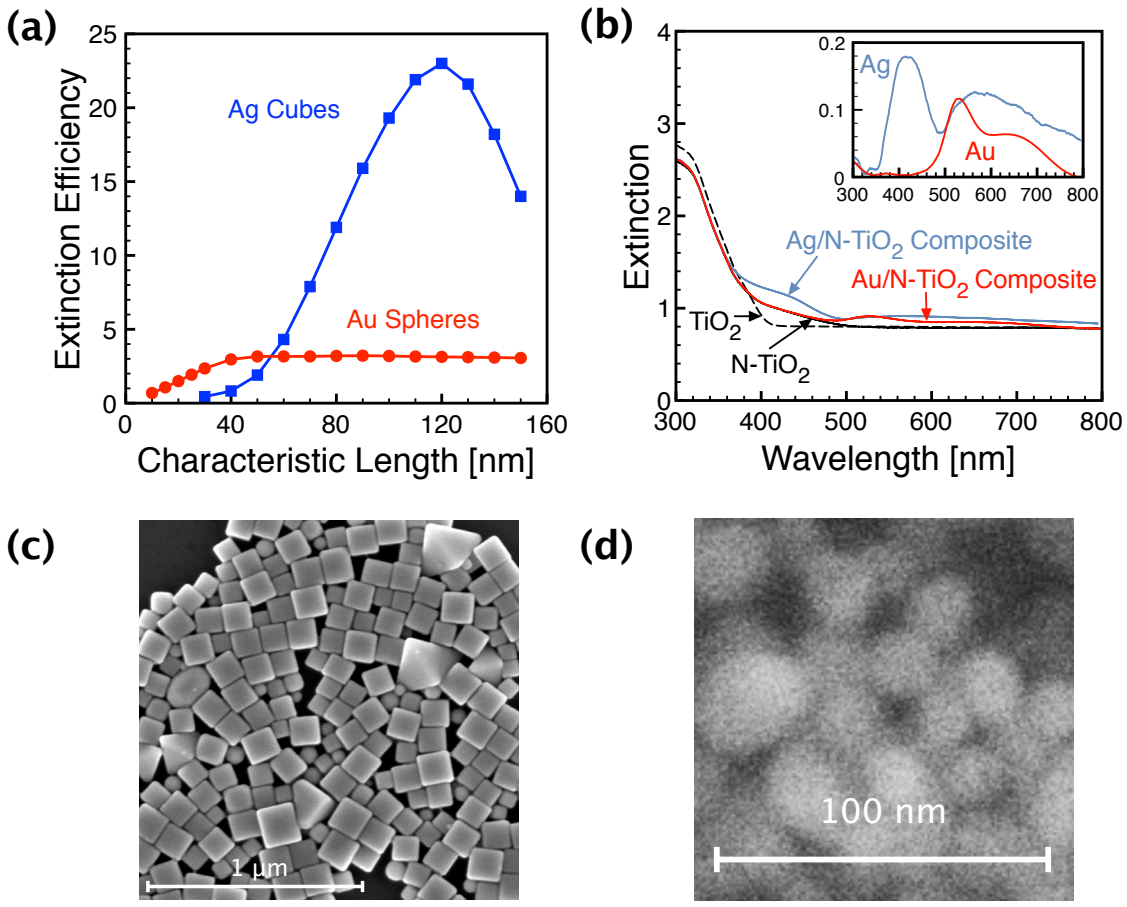

Figure 5.2: Characterization of semiconductors, plasmonic metals and composite photo-electrodes. (a) Extinction efficiencies (extinction cross-section divided by geometric cross-section) averaged over wavelengths of 400–500 nm for Ag cubes and Au spheres as a function of particle size (cube edge length or sphere diameter). These were calculated using finite-difference time-domain optical simulations (see supporting information). (b) UV-visible extinction spectra of TiO_2, N-TiO_2, Ag/N-TiO_2 and Au/N-TiO_2 samples. The inset shows difference spectra for Ag and Au (e.g. Ag/N-TiO_2 spectrum minus N-TiO_2 spectrum). (c) Scanning electron micrograph (SEM) of Ag nanocubes with an average edge length of 118 nm and a standard deviation of 25 nm. (d) SEM of Au spherical particles with an average diameter of 24.5 nm and a standard deviation of 4.5 nm.

total-field/scattered-field (TFSF) formalism [32]. The extinction efficiency reported in Figure 5.2a was calculated by averaging the extinction cross section from 400–500 nm and dividing by the particle's geometric cross-sectional area. The wavelength range of 400–500 nm was used because the N-TiO_2 particles (synthesized as described below) absorb light at wavelengths of ∼500 nm and below, while the visible light source used (see experimental details below) cuts off below 400 nm.

N-TiO_2 was synthesized by heating TiO_2 particles (∼20 nm diameter) in the presence of NH_3 [29], as described in detail in the Synthesis section of Chapter 3. The resulting N-TiO_2 powder was slightly yellow in color, as quantified by the increased visible absorbance shown in Figure 5.2b. Ag nanocubes and Au spheres were synthesized using a previously reported modified polyol process [39, 40]. This process is also described in the Synthesis section of Chapter 3. The resulting cubic Ag nanoparticles were 118 ± 25 nm edge length and the Au spheres were 24.5 ± 4.5 nm diameter, both measured by scanning electron microscopy (see Figure 5.2c and 5.2d). It is important to note that the metal nanostructures, as used in the experiments, were coated with non-conducting organic stabilizer molecules (polyvinylpyrrolidone, PVP). These stabilizer molecules play a critical role in separating the metal and semiconductor particles and limiting Förster energy transfer between the semiconductor and metal [41, 42]. This is discussed in more detail further below.

The N-TiO_2 powder was suspended in 200-proof ethanol (EtOH) at a ratio of 99 g EtOH per gram of N-TiO_2; the solution was sonicated for one hour. Composite solutions were prepared by mixing the Ag nanocube colloidal solution or Au nanosphere solution with the N-TiO_2 in ethanol mixture and sonicating again for one hour. Composites were 5% metal by weight in both cases. The samples were prepared by applying the nanoparticle solution to 1-in^2 conductive substrates (glass

coated with indium tin oxide) with a micropipette; the samples were allowed to dry in a stagnant atmosphere. All samples contained 2 mg N-TiO_2 (constant semiconductor weight, volume, surface area). UV-visible extinction spectra of the samples are shown in Figure 5.2b. All spectra were measured performed using a Thermo Scientific Evolution 300 UV-visible spectrophotometer with a Harrick Praying Mantis diffuse reflectance accessory.

The composite photo-electrodes were physical mixtures of Ag and N-TiO_2 (Ag/N-TiO_2) or Au and N-TiO_2 (Au/N-TiO_2). The metal loading was 5% by weight with respect to the semiconductor. Photo-electrodes were supported on an inert conductive substrate (glass coated with indium tin oxide). The mass, volume, and surface area of N-TiO_2 were constant in all experiments. UV-visible extinction spectra of the photo-electrode samples are shown in Figure 5.2b. The figure inset shows the difference in extinction between the composite materials and the samples containing N-TiO_2 only. The difference is due to the light-induced resonant formation of SP states on Au and Ag nanoparticles.

A glass beaker was fitted with a quartz window. The beaker was filled with 1 M KOH, which was continuously stirred with a magnetic stir bar and deaerated by bubbling Argon. The photo-electrodes, prepared as described in the previous paragraph, were suspended in the beaker facing the quartz window and attached to the working electrode lead of a potentiostat (Princeton Applied Research PARSTAT-2273 Potentiostat/Galvanostat/FRA). A Pt wire counter electrode and Hg/HgO reference electrode were used and a bias of 0.3 V was applied. The cell operating with 0.3 V bias in the dark does not split water (thermodynamics dictates that at least 1.23 V is required to electrolyze water at room temperature). Under illumination the bias is necessary to help evolve H_2 at the Pt counter-electrode (the photo-excited

electrons are slightly lower in energy than the H+/H_2 potential). Without the bias the H_2 evolution half-reaction does not proceed and thus the process of overall water splitting is not possible.

The photo-electrodes were illuminated with a broadband visible light source that delivers a total power of ∼500 mW/cm^2 at the photo-electrode surface (see Figure 5.3a). Wavelength dependent studies employed a series of optical filters to isolate the broadband source into roughly monochromatic points (FWHM ∼25 nm). The source intensities as a function of wavelength using the optical filters are shown in Figure 5.3b. A monochromatic UV light source (365 nm, FWHM 5 nm, ∼5 mW/cm^2) was also used in these studies, and is indicated by an open circle in Figure 5.3b.

The water splitting reaction rate was monitored by measuring the evolved gases using quadupole mass spectrometry and by measuring the photocurrent conducted around the external circuit through the potentiostat. The measured photocurrent and gas evolution rates were shown in the manuscript. We note that the mass spectrometry measurements showed no evidence of the evolution of carbon-containing species. The photocurrent was monitored as a measure of the water splitting reaction rate. Two molecules of water that are transformed into $2H_2$ and O_2 produces 4 electrons that flow through the external circuit. If we assume that the reaction occurring in the cell is the overall splitting over water, then the photocurrent is proportional to the reaction rate. To check this assumption the amount of gasses produced was also measured using mass spectrometry. H_2 and O_2 were produced in the correct stoichiometric amounts (i.e. 2 moles of H_2 for each mole of O_2), which suggests that the process occurring in the cell is in fact the overall splitting of water to form H_2 and O_2.

We note that we also tested un-doped P25 TiO_2 under UV illumination and

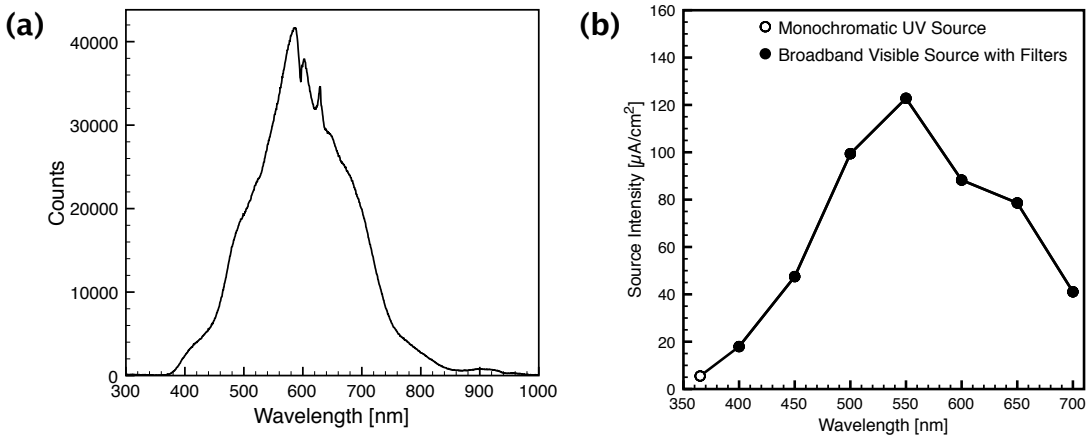

Figure 5.3: Visible light source characteristics. (a) Visible light source spectrum. The total intensity is ∼500 mW/cm^2 at the photo-electrode surface. (b) Source intensity as a function of wavelength for the broadband visible source using optical filters (closed circles); the FWHM for these points is ∼25 nm. The open circle represents a monochromatic UV light source (365 nm, FWHM 5 nm, ∼5 mW/cm^2).

observed the same effects. However, we focus on N-TiO_2 rather than P25 under visible sun-like illumination because the magnitude of the photocurrent generated by P25 under illumination with our visible source is quite small and difficult to measure accurately. There are several reasons for this: (1) While the band gap of rutile is nominally 3.0 eV (413 nm), the actual absorbance in this range is very low. (2) Because of the surface structure, the rutile phase shows much lower photo-activities than the anatase phase [43].

5.4 Results and Discussion

In Figure 5.4 we show that upon the illumination of photo-electrodes with a broadband visible source (400–900 nm, ∼500 mW/cm^2, spectral peak at 580 nm) stoichiometric amounts of H_2 and O_2 were produced, suggesting the overall splitting of water. The current response is also shown in Figure 5.4. The photocurrent is proportional to the water splitting reaction rate: transforming two molecules of water into $2H_2$ and O_2 produces 4 electrons that flow through the external circuit. Figure 5.4 shows that the addition of plasmonic Ag nanoparticles to N-TiO_2 increases visible light photocurrent by a factor of ∼10. On the other hand, the addition of Au nanoparticles has a small effect on the photocurrent.

Figure 5.5a shows the photocurrent as a function of source wavelength. Optical filters were used to modulate the wavelength of the broadband visible source; however, it is important to note that the illumination intensity was not constant across all wavelengths (see Figure 5.3b). Because of this it is more instructive look at the photocurrent for the composite at a particular wavelength, normalized by the photocurrent of the semiconductor alone at the same wavelength, which is shown in Figure 5.5b. The figure shows that the enhancement depends strongly on the source

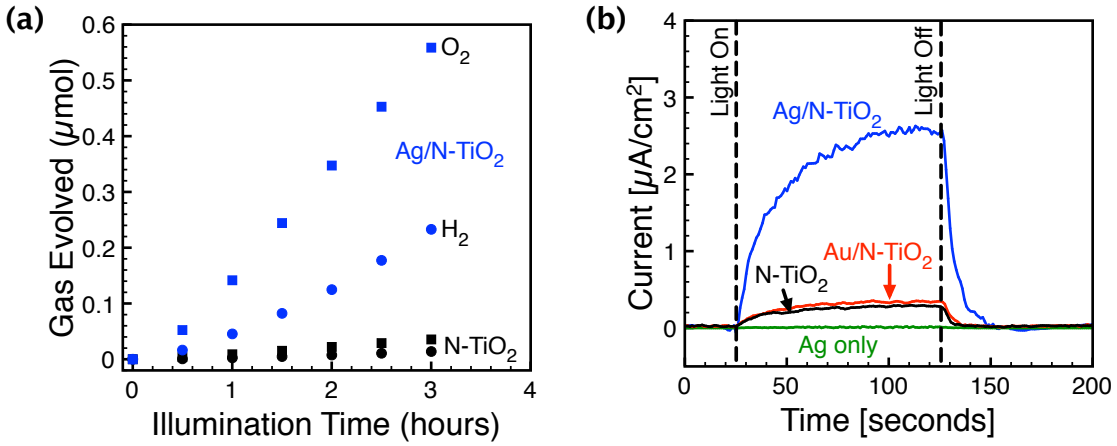

Figure 5.4: Water splitting rate measurements. (a) H_2 (squares) and O_2 (circles) production upon visible illumination of N-TiO_2 (black points) and Ag/N-TiO_2 (blue points) photocatalysts, measured by mass spectrometry. (b) Photocurrent response (per macroscopic electrode area) upon illumination with a broadband visible light source (400–900 nm).

wavelength, and that it qualitatively tracks with the intensity of the Ag UV-visible extinction (also shown in Figure 5.5b). Since the Ag extinction is a consequence of the excitation of Ag SP states, the qualitative mapping between the rate enhancement and the Ag extinction suggests that the Ag plasmons are responsible for the observed rate enhancement. We have previously investigated interactions between excited plasmonic metal particles, coated with non-conductive molecules, and a nearby semiconductor in a non-reactive environment. These studies showed that for these systems, the presence of the organic layer prevents direct electron transfer; instead, energy is transferred from the metal surface plasmons to the semiconductor in a radiative process, increasing the overall concentration of charge carriers in the semiconductor, see ref. [21] and Chapter 4.

Several alternative mechanisms have been proposed to describe the interaction between plasmonic metal nanoparticles and semiconductors, as discussed in Chapters 2 and 4. Several publications report an enhancement of photo-rates by the addition of metal nanoparticles (including Pt [44], Au [44–47], and others [44, 48]) and this is commonly attributed to a transfer of photo-excited electrons from the semiconductor to the metal particles, which increases the lifetime of charge carriers (mainly holes in the semiconductor). While charge transfer is certainly observed in some systems, our previous measurements using absorption spectroscopy [21] and photoluminescence measurements [21] have shown no evidence of charge transfer between Ag and TiO_2 in these systems (also see Chapters 3 and 4). In addition, the fact that the wavelength-dependent intensity of Ag surface plasmons and the wavelength-dependent rate enhancement are proportional to each other suggests that the surface plasmons play a critical role. More importantly, our measurements comparing Ag and Au (these two metals are very similar to each other with respect to their elec-

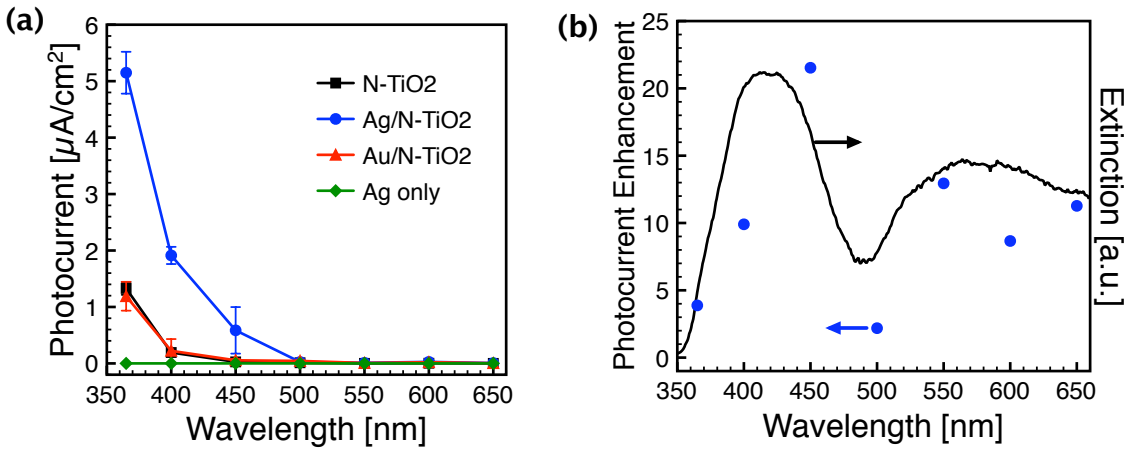

Figure 5.5: Wavelength-dependent photocurrent measurements. (a) Photocurrent as a function of source wavelength for N-TiO_2 only, Ag only and composite photo-electrodes. (b) Dots: Photocurrent enhancement for Ag/N-TiO_2 composite (photocurrent for Ag/N-TiO_2 divided by that of N-TiO_2 only) as a function of excitation wavelength. Line: Ag nanocube spectrum (spectrum for Ag/N-TiO_2 minus that of N-TiO_2 only, from Figure 5.2). While large enhancements are observed at energies lower than the N-TiO_2 absorbance (i.e. > 500 nm), the absolute reaction rates at these wavelengths are very small (see Figure 5.5a).

tron conductivity and the driving force to transfer electrons, i.e., the Fermi levels of these two metals are similar) show that the underlying mechanisms includes an energy (not charge) transfer from Ag to N-TiO_2. The main reason for the different mechanisms reported here and those discussed previously is the different geometric arrangement of metallic and semiconductor building blocks, i.e., in our system these are separated from each other by the stabilizer molecules, while in the other systems they are directly in contact with each other which makes the charge transfer process feasible.

It is also possible that Ag nanoparticles could act as a co-catalyst, either promoting the evolution of O_2 or H_2 (as has been shown for Pt, Au, Ir, etc. [44–48]). Samples containing Ag particles-only show no activity (see Figure 5.4b). In order for Ag to act as a co-catalyst for the O_2 evolution reaction, it would require that there was effective physical contact between the Ag and N-TiO_2 particles. Essentially, for Ag to be an O_2-evolution co-catalyst, the electric potential of the hole in Ag should be close to the hole potential in TiO_2, i.e., there needs to be a charge transfer from semiconductor to metal. As we have discussed above, this is not the case. In our system Ag and N-TiO_2 are separated from each other and they communicate only by the electric field near Ag exciting the formation of charge carriers in TiO_2. The same arguments can be used to rule out the potential role of Ag in H_2 evolution. The situation is even worse here since the energy of excited electron in TiO_2 is not sufficient to evolve H_2 on Ag. We note that Ag is not as active as Pt for this reaction. For Ag, the electron energy significantly higher than zero (on the NHE scale) is required to evolve H_2. Please refer back to Chapter 2 for additional discussion of these mechanisms.

The near-field electromagnetic enhancement mechanism is further supported by a

comparison of the water splitting performance of composites containing Ag and Au nanostructures. Unlike the Ag/N-TiO_2 composites, the photo-electrodes containing Au do not show significant rate enhancements, see Figure 5.4. The only significant difference between the optical properties of Ag and Au is that the Au SPR is red-shifted compared to that of Ag cubes. Figure 5.2b shows that the Au nanostructures support SPR at wavelengths above 500 nm. This energy of the Au SPR is insufficient to lead to the formation of e^-/h^+ pairs in N-TiO_2 in the radiative energy transfer process—N-TiO_2 absorbs only below ∼500 nm. The different performance of Ag/N-TiO_2 and Au/N-TiO_2 provides additional evidence that the role of the metal in this system is not to promote the conduction of charge carriers in the composite photo-electrodes.

It is important to analyze how this energy transfer from plasmonic Ag nanostructures results in such a dramatic increase in the reaction rates. To address this issue we analyze the interaction of the Ag SP states with a flux of resonant source photons. For large Ag nanostructures (characteristic length above ∼50 nm), this interaction leads to a very efficient scattering of resonant photons by the nanostructures [15–17]. Therefore, for large Ag nanoparticles, the extinction by the Ag/N-TiO_2 composites is a superposition of the direct absorption by N-TiO_2 (leading to e/h pairs) and mainly scattering from the Ag structures (Figure 5.2). The scattering of photons by Ag increases the average photon path length in the composites, causing an increased rate of e^-/h^+ pair formation in N-TiO_2 [49–51]. Here, Ag would essentially be acting as a mirror—some resonant photons that are not absorbed by N-TiO_2 upon first pass through the composite material could be scattered by Ag, effectively giving those photons multiple passes through the system. The scattering effect can be isolated and quantified by measuring the increase in photon extinction in the sample due to

the addition of Ag particles. If we assume that every photon that is scattered by Ag is absorbed by N-TiO_2 and converted to an e/h pair, we would expect one-to-one mapping between the rate enhancement and the enhancement in the number of scattered photons (related but not equal to the difference spectrum in Figure 5.5). Based on analysis of the UV-visible extinction spectra in Figure 5.2b, we estimate that at 400–500 nm there is at most approximately a 25% increase in the number of photons absorbed in the Ag/N-TiO_2 sample compared to N-TiO_2. This increase in absorbed photons is insufficient to explain the much larger observed enhancements in the reaction rate.

In addition to efficient photon scattering, the formation of resonant SP states results in an enhancement of local electric fields in the neighborhood of the Ag nanostructures [15–17]. This is illustrated in Figure 5.6, which shows the FDTD-calculated field enhancements from a 120-nm Ag cube in water. When a semiconductor is brought in the proximity of Ag, it encounters these intense electric fields. This process results in the rapid formation of e^-/h^+ pairs in the semiconductor. An important feature of the electric fields is that they are spatially non-homogenous—the field strength is highest in the proximity of the nanostructures. This suggests that SP-induced e^-/h^+ pair formation should be highest in the part of the semiconductor that is the closest to Ag, i.e., near the surface of the semiconductor particles (essentially at the semiconductor/liquid interface). The advantage of the formation of e^-/h^+ pairs in the semiconductor surface, compared to a bulk formation is that: (i) under the influence of the surface potential the charge carriers are separated from each other readily and (ii) charge carriers migrate shorter distances to the surface where they can perform a photo-catalytic transformation. This effectively means that the probability of photo-reaction is enhanced compared to the probability of charge

carrier recombination. It should be mentioned that the optimal distance between a semiconductor and a plasmonic nanostructure is also affected by Förster energy transfer from the semiconductor to the metal [19, 42]; this is addressed in more detail in Chapter 6. In photo-electrodes used herein, the organic PVP layer represents a buffer that keeps the two nanostructures at a finite distance from each other without physically touching, providing an environment where the negative effect of the Förster energy transfer is diminished.

To further test the hypothesis that very intense local electric fields lead to increased rates of e^-/h^+ pair formation at the semiconductor surface resulting in large rate enhancements, we have measured the rate of the water splitting reaction as a function of the intensity of broadband visible illumination. Figure 5.7 shows that N-TiO_2 exhibits $\sim$ 1/2 order dependence on light intensity while the composite Ag/N-TiO_2 exhibits $\sim$1st order dependence. If we assume that the rate of oxygen evolution on the semiconductor is linearly dependent on the surface concentration of h^+, then Figure 5.7 shows that the surface concentration of h^+ follows 1st and order intensity dependence in Ag/N-TiO_2 and N-TiO_2, respectively. It has been shown previously in surface science measurements that the surface h^+ concentration for charge carriers formed in the bulk of TiO_2 shows a order dependence on light intensity [7]. This is because the bulk recombination is second order with respect to charge carriers, as shown in Equation 5.1.

$$e^- + h^+ \longrightarrow \text{heat or photon emission} \tag{5.1}$$

In separate experiments, the same group studied the surface-specific formation of charge carriers by using a flux of energetic electrons [8]. The electron flux has a much shorter penetration depth ($<$ 1 nm) and therefore selectively creates electron/hole

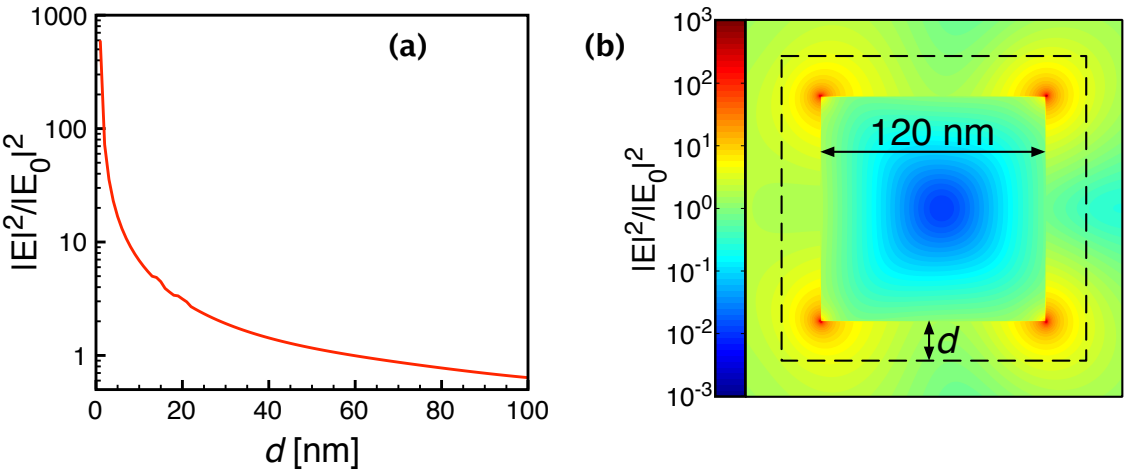

Figure 5.6: Simulated spatial distribution of EM fields. (a) Average electric field enhancement, calculated using FDTD simulations, around an Ag sphere with the edge length of 120 nm as a function of distance d from the sphere. (b) Local enhancement of the electric field calculated from FDTD simulation of a 120-nm Ag cube in water.

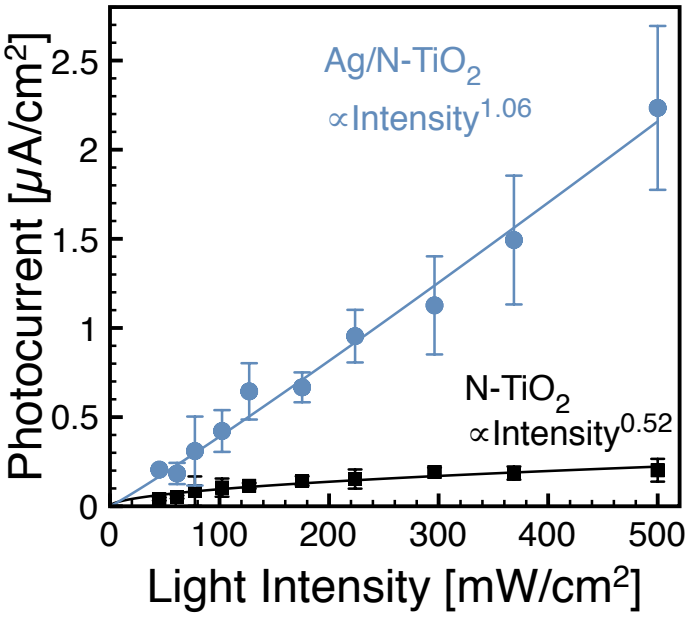

Figure 5.7: Photocurrent as a function of broadband visible light intensity for N-TiO_2 and composite Ag/N-TiO_2 samples. Ag/N-TiO_2 exhibits approximately a linear dependence on light intensity while N-TiO_2 exhibits $\sim 1/2$ power dependence.

pairs at the surface of the semiconductor. They found that the concentration of h^+ for charge carriers formed in the surface layers of TiO_2 depends linearly on light intensity [7, 8]. This is because the primary surface recombination route is via recombination with surface trap states. As shown in Equations 5.2 and 5.3, these surface trap recombination processes are first-order with respect to charge carriers.

$$h^+ + \text{Trap} \longrightarrow \text{Trap}^+ \tag{5.2}$$

$$e^- + \text{Trap}^+ \longrightarrow \text{Trap} \tag{5.3}$$

In light of these results, the observed linear dependence of the surface concentration of h^+ on light intensity for Ag/N-TiO_2 (Figure 5.7) is another indication that charge carriers are formed close to the semiconductor surface in the composite Ag/N-TiO_2 systems. The selective formation of e^-/h^+ pairs near the surface of the semiconductor offers several advantages, as previously mentioned. Chief among these is that the charge carriers have to travel a shorter distance to the surface where they can perform a photo-catalytic transformation. This means that there is an enhanced probability for photo-reaction (i.e. channeling photo energy into production of H_2 and O_2) compared to the probability of electron/hole pair recombination.

5.5 Conclusion

We have demonstrated that plasmonic Ag nanostructures can be employed as building blocks to create composite plasmonic-metal/semiconductor photo-electrocatalysts that exhibit enhanced water splitting performance, compared to semiconductor alone. Our experiments and simulations show that the enhancement can be primarily attributed to the formation of intense electric fields at the Ag particle surface, which increases the rate of formation of e^-/h^+ pairs at the nearby N-TiO_2

particle surface (i.e., at the semiconductor/liquid interface). The advantage of the formation of e^-/h^+ pairs in the semiconductor surface is that these charge carriers are separated from each other readily, and that they migrate to the surface easily where they can perform a photo-catalytic transformation. The ability to tune the size and shape of plasmonic metal nanoparticles, and thereby control the energy and intensity of the SPR, offers a great deal of flexibility in the design of efficient composite plasmonic-metal/semiconductor photo-catalysts. In addition to the critical importance of the size and shape of plasmonic nanostructures, the proximity of the semiconductor and metal building blocks is another important design parameter.

References

[1] Fujishima, A.; Honda, K. *Nature* **1972**, *238*, 37–38.

[2] Takata, T.; Tanaka, A.; Hara, M.; Kondo, J. N.; Domen, K. *Catal. Today* **1998**, *44*, 17–26.

[3] Cesar, I.; Kay, A.; Martinez, J. A. G.; Grätzel, M. *J. Am. Chem. Soc.* **2006**, *128*, 4582–4583.

[4] Kudo, A.; Miseki, Y. *Chem. Soc. Rev.* **2009**, *38*, 253–278.

[5] Linsebigler, A. L.; Lu, G.; Yates, Jr., J. T. *Chem. Rev.* **1995**, *95*, 735–758.

[6] Fujishima, A.; Zhang, X.; Tryk, D. A. *Surf. Sci. Rep.* **2008**, *63*, 515–582.

[7] Yates, Jr., J. T. *Surf. Sci.* **2009**, *603*, 1605–1612.

[8] Zhang, Z.; Yates, Jr., J. T. *J. Phys. Chem. C* **2010**, *114*, 3098–3101.

[9] Ondersma, J. W.; Hamann, T. W. *J. Am. Chem. Soc.* **2011**.

[10] Goldberger, J.; He, R.; Zhang, Y.; Lee, S.; Yan, H.; Choi, H.-J.; Yang, P. *Nature* **2003**, *442*, 599–602.

[11] Mor, G. K.; Shankar, K.; Paulose, M.; Varghese, O. K.; Grimes, C. A. *Nano Lett.* **2005**, *5*, 191–195.

[12] Zhu, K.; Neale, N. R.; Miedaner, A.; Frank, A. J. *Nano Lett.* **2007**, *7*, 69–74.

[13] Maiolo III, J. R.; Kayes, B. M.; Filler, M. A.; Putnam, M. C.; Kelzenberg, M. D.; Atwater, H. A.; Lewis, N. S. *J. Am. Chem. Soc.* **2007**, *129*, 12346–12347.

[14] Cesar, I.; Sivula, K.; Kay, A.; Zboril, R.; Grätzel, M. *J. Phys. Chem. C* **2009**, *113*, 772–782.

[15] El-Sayed, M. A. *Acc. Chem. Res.* **2001**, *34*, 257–264.

[16] Kelly, K. L.; Coronado, E.; Zhao, L. L.; Schatz, G. C. *J. Phys. Chem. B* **2003**, *107*, 668–677.

[17] Brus, L. *Acc. Chem. Res.* **2008**, *41*, 1742–1749.

[18] Lee, J.; Javed, T.; Skeini, T.; Govorov, A. O.; Bryant, G. W.; Kotov, N. A. *Angew. Chem. Int. Ed.* **2006**, *45*, 4819–4823.

[19] Anger, P.; Bharadwaj, P.; Novotny, L. *Phys. Rev. Lett.* **2006**, *96*, 113002–1–4.

[20] Awazu, K.; Fujimake, M.; Rockstuhl, C.; Tominaga, J.; Murakami, H.; Ohki, Y.; Yoshida, N.; Watanabe, T. *J. Am. Chem. Soc.* **2008**, *130*, 1676–1680.

[21] Christopher, P.; Ingram, D. B.; Linic, S. *J. Phys. Chem. C* **2010**, *114*, 9173–9177.

[22] Liu, Z.; Hou, W.; Pavaskar, P.; Aykol, M.; Cronin, S. B. *Nano Lett.* **2011**, *11*, 1111–1116.

[23] Hou, W.; Liu, Z.; Pavaskar, P.; Hung, W. H.; Cronin, S. B. *J. Catal.* **2011**, *277*, 149–153.

[24] Thomann, I.; Pinaud, B.; Chen, Z.; Clemens, B.; Jaramilo, T.; Brongersma, M. L. *Nano Letters* **2011**.

[25] Tian, Y.; Tatsuma, T. *J. Am. Chem. Soc.* **2005**, *127*, 7632–7637.

[26] Kowalska, E.; Abe, R.; Ohtani, B. *Chem. Comm.* **2009**, 241–243.

[27] Mori, K.; Kawashima, M.; Che, M.; Yamashita, H. *Angewandte Chemie* **2010**.

[28] Sato, S. *Chem. Phys. Lett.* **1986**, *123*, 126–128.

[29] Irie, H.; Watanabe, Y.; Hashimoto, K. *J. Phys. Chem. B* **2003**, *107*, 5483–5486.

[30] Lindgren, T.; Mwabora, J. M.; Avendaño, E.; Jonsson, J.; Hoel, A.; Granqvist, C.-G.; Lindquist, S.-E. *J. Phys. Chem. B* **2003**, *107*, 5709–5716.

[31] Asahi, R.; Morikawa, T.; Ohwaki, T.; Aoki, K.; Taga, Y. *Science* **2001**, *293*, 269–271.

[32] Taflove, A.; Hagness, S. C. *Computational Electrodynamics: The Finite-Difference Time-Domain Method*; Artech House: Boston, 2005.

[33] McMahon, J. M. Ph.D. thesis, Northwestern University: Evanston, Illinois, 2010.

[34] Wooten, F. *Optical Properties of Solids*; Academic: New York, 1972.

[35] Ashcroft, N. W.; Mermin, N. D. *Solid State Physics*; Brooks Cole, 1976.

[36] Palik, E. D. *Handbook of Optical Constants of Solids*; Academic Press: New York, 1985.

[37] Link, S.; El-Sayed, M. A. *J. Phys. Chem. B* **1999**, *103*, 4212–4217.

[38] McMahon, J. M.; Wang, Y.; Sherry, L. J.; Van Duyne, R. P.; Marks, L. D.; Gray, S. K.; Schatz, G. C. *Journal of Physical Chemistry C* **2009**, *113*, 2731–2735.

[39] Christopher, P.; Linic, S. *ChemCatChem* **2010**, *2*, 78–83.

[40] Im, S. H.; Lee, Y. T.; Wiley, B.; Xia, Y. *Angewandte Chemie* **2005**, *44*, 2154–2157.

[41] Clegg, R. M. *Current Opinion in Biotechnology* **1995**, *6*, 103–110.

[42] Govorov, A. O.; Lee, J.; Kotov, N. A. *Phys. Rev. B* **2007**, *76*, 125308.

[43] Augustynski, J. *Electrochim. Acta* **1993**, *38*, year.

[44] Subramanian, V.; Wolf, E.; Kamat, P. V. *J. Phys. Chem. B* **2001**, *105*, 11439–11446.

[45] Subramanian, V.; Wolf, E. E.; Kamat, P. V. *J. Am. Chem. Soc.* **2004**, *126*, 4943–4950.

[46] Silva, C. G.; Juárez, R.; Marino, T.; Molinari, R.; García, H. *J. Am. Chem. Soc.* **2011**, *133*, 595–602.

[47] Primo, A.; Corma, A.; García, H. *Phys. Chem. Chem. Phys.* **2011**, *13*, 886–910.

[48] Arabatzis, I. M.; Stergiopoulos, T.; Bernard, M. C.; Labou, D.; Neophytides, S. G.; Falaras, P. *Appl. Catal. B* **2003**, *42*, 187–201.

[49] Derkacs, D.; Lim, S. H.; Matheu, P.; Mar, W.; Yu, E. T. *Appl. Phys. Lett.* **2006**, *89*, 093103.

[50] Pala, R. A.; White, J.; Barnard, E.; Liu, J.; Brongersma, M. L. *Adv. Mater.* **2009**, *21*, 1–6.

[51] Atwater, H. A.; Polman, A. *Nat. Mater.* **2010**, *9*, 205–213.

CHAPTER 6

Geometric Model for Designing Plasmonic Metal/Semiconductor Composites

6.1 Summary

It has recently been demonstrated that the photocatalytic activity of semiconductors can be enhanced through interaction with enhanced local electromagnetic fields due to the excitation of surface plasmon resonance (SPR) on nearby metal nanoparticles. These interactions, as well as competing parasitic loss mechanisms, are highly dependent on the distance between the metal and semiconductor. We have investigated this distance dependence experimentally and constructed a model that captures this dependence. The SPR-induced fields are highest at the metal nanoparticle surface, suggesting that the enhancement is greatest when metal and semiconductor are placed close together. However, at very small distances, the interactions are governed by parasitic losses in charge carriers in the semiconductor due to non-radiative transfer to the metal (e.g. Förster transfer). The model constructed here suggests that small metal/semiconductor separation distances are beneficial but that a transparent spacer layer between the two may be necessary to prevent these parasitic losses.

6.2 Introduction

Semiconductor photocatalysts are useful for a range of photo-reactions, notably the production of H_2 from water using sunlight (photochemical water splitting), which is a promising technology for production of sustainable fuels [1–3]. When a semiconductor is illuminated with light having energy greater than its band gap, excited charge carriers (electron/hole pairs) are formed within semiconductor. The charge carriers, which are primarily formed in the bulk, then diffuse to the semiconductor surface where they can participate in the O_2 evolution ($H_2O + 2h^+ \longrightarrow 2H^+ + 1/2O_2$) and H_2 evolution ($2H^+ + 2e^- \longrightarrow H_2$) half reactions. Large-scale implementation of photocatalytic processes, such as water splitting, using conventional metal oxide semiconductors (e.g. anatase phase TiO_2 or hematite phase Fe_2O_3) is hindered by low reaction rates, primarily because of low photon absorption coefficients and high charge carrier recombination rates, as discussed in detail in Chapter 2. Attempts to address these problems have primarily focused on improving bulk charge carrier mobility (e.g. by improving crystallinity [4], by adding mobility-promoting dopants [5, 6]) or by controlling the photocatalyst structure so that photon absorption can be maximized while minimizing the distance charge carriers travel before reaching the surface [4, 7–9].

Recently it has been shown that another potential route to enhance semiconductor activity is the addition of photo-excited metal nanoparticles [10–20]. These composite metal/semiconductor photocatalysts are distinct from previous semiconductor/co-catalyst materials [21–23] because the metal particles are directly excited by the source illumination, whereas conventional co-catalysts are not. The photo-excited metal particles within this class of composite photocatalysts are characterized by

their strong interaction with light via the excitation of surface plasmon resonance (SPR) when illuminated with resonant photons [24–26]. Three primary mechanisms have been identified that dictate how the metal SPR can enhance photoreaction rates on a nearby semiconductor. The first mechanism involves excitation of the metal SPR by resonant photons, followed by transfer of electrons from metal to the semiconductor [10, 11, 14, 17, 18]. It is proposed that the charged semiconductor then facilitates the H_2 evolution half reaction. A hole scavenger is typically necessary, as the holes generated in the metal are generally too high in energy to facilitate the oxygen evolution half reaction. This mechanism is similar to dye-sensitization [27, 28] and is observed when there is close physical contact between the Ag and semiconductor, which is necessary to facilitate charge transfer.

The second mechanism is due to optical interactions between the metal and semiconductor. The photo-response of the metal nanoparticles is a consequence of the presence of very intense SPR-induced electromagnetic (EM) fields near the surface of the photo-excited metal nanoparticles [12, 13, 15, 16, 19, 20]. The rate of charge carrier formation in a semiconductor is proportional to the intensity of the incident EM field [29, 30]. Upon addition of plasmon-active metal particles, the rate of charge carrier formation in the semiconductor is increased due to the local SPR-enhanced EM field intensity, resulting in higher photocatalytic rates. The SPR-induced fields are spatially non-homogeneous. This is illustrated in Figure 6.1, which shows the results of a finite-difference time-domain (FDTD) optical simulation of a single Ag cube with 80-nm edge length in water. Please consult the Optical Simulation section of Chapter 3 for details regarding simulation methodology. The figure shows the spatial distribution of the electric field intensity ($|E|^2$) at the SPR peak; field intensity is enhanced by up to 10^3, with the most intense fields being concentrated at

the corners of the particles and decaying with distance approximately proportional to 1/distance. As discussed above and in previous chapters, it has been proposed that the SPR-induced enhancement of local EM fields leads to enhanced generation of charge carriers in a neighboring semiconductor. Furthermore, it has been shown that the spatial distribution of the EM field enhancement affects the spatial distribution of charge carrier formation the semiconductor, e.g. leading to a selective increase in formation of charge carriers at the semiconductor surface, which partially alleviates the problem of bulk charge carrier recombination [16], see Chapter 5.

The third mechanism is also due to the photo-response of metal nanoparticles, and can also lead to increased charge carrier formation in a nearby semiconductor [31–33]. In the limit of large separation (tens of nanometers) between metal and semiconductor, there is little spatial overlap of the SPR-induced EM fields with the semiconductor. However, the presence of the metal nanoparticles acts to increase the average pathlength of photons through the composite material. In this case, what is important is simply that the metal particles are strong photon scatterers—e.g. the same effect can be accomplished using non-metallic light scattering particles [34], where there is no excitation of SPR. Depending on the specific geometry of the system, this can be a major effect (e.g. in thin film solar cells [33]). This effect is often regarded as a fundamentally different mechanism; however, we will discuss it below as the far-field manifestation of the mechanism discussed above (in contrast to the near-field manifestation, which requires spatial overlap of the SPR-induced fields with the semiconductor). The point is that both near- and far-field manifestations enhance photo-activity by increasing the rate of charge carrier generation in the semiconductor and as such, both require that the metal SPR overlaps in energy with the semiconductor absorbance.

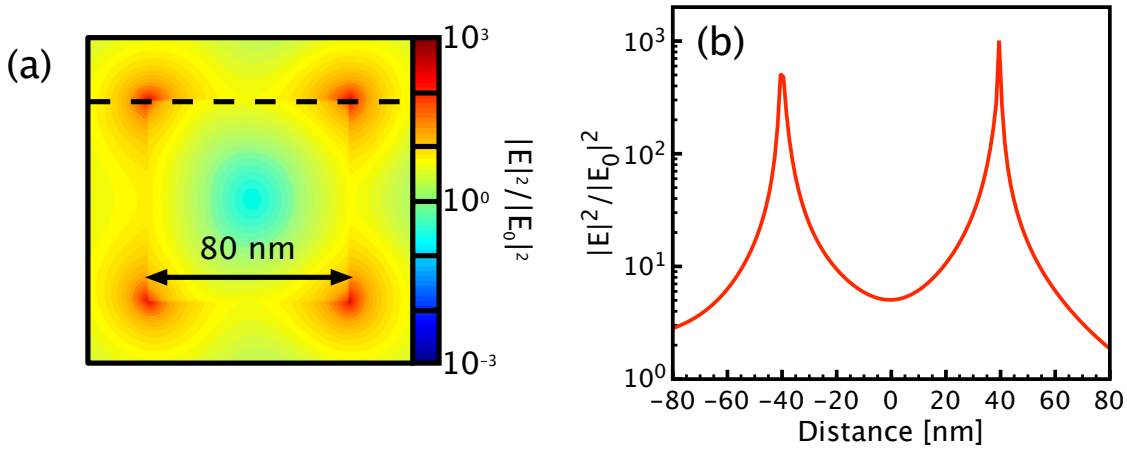

Figure 6.1: Spatial distribution of electric field intensity around a Ag nanocube. (a) Plasmon-induced enhancement in the intensity of electric fields in and around an 80-nm edge length Ag cube, calculated from an FDTD simulation. (b) Enhancement in the electric field intensity (Fourier transformed at the SPR peak) as a function of distance along the dashed line indicated in (a).

In addition to the spatial distribution of SPR-induced fields, parasitic/quenching mechanisms such as Förster resonance energy transfer (FRET) [30, 35–37] also play a role in governing the performance of composite systems under certain conditions. For example, it has been shown that the presence of a plasmonic metal particle can quench the rate of fluorescence emission from a nearby semiconductor particle through non-radiative energy transfer from the semiconductor to the metal via dipolar coupling [30]. This process results in a decrease in the charge carrier concentration in the semiconductor and consequently in a reactive system would decrease the photo-reaction rate [38]. As we will discuss in greater detail below, these parasitic loss mechanisms are also highly dependent on the separation distance between the metal and semiconductor particles.

These distance-dependent phenomena suggest that the nano-scale geometric arrangement of building blocks is important for constructing composite photocatalysts with the maximum photo-activity. That is, it is important to design (and synthesize) geoemetries that maximize the spatial overlap of SPR-induced EM fields with the semiconductor structures while avoiding parasitic losses. Recent work has laid the groundwork for understanding the design of such systems on a macroscopic scale based on the materials' optical properties (how to tailor the optical properties of each material for maximum interaction) [13, 19, 29, 39], see Chapter 4. However, the nanoscale phenomena discussed above are not well studied or understood and as a result nano-scale models for optimizing the geometry of these systems are missing.

In this chapter we investigate the dependence of the photoactivity on the separation distance between composite building blocks and make progress toward developing a model that can be used to design composite plasmonic metal/semiconductor photocatalysts. We measure photoactivity by monitoring both the photocurrent in

a photoelectrochemical (PEC) cell and the photoluminescence emission, which is directly related to the rate of charge carrier formation. We focus on composite systems containing cubic Ag nanoparticles and one of two semiconductors—TiO_2 or nitrogen-doped TiO_2 (N-TiO_2). Ag nanocubes were selected because the SPR of these structures overlaps well with the absorbance of the semiconductors (e.g. Au nanoparticles also have an intense photo-response, but the energy of the SPR is not in resonance with the TiO_2 absorbance), see Chapter 4. The use of both TiO_2 and N-TiO_2 gave us the ability to test the effect of changing the optical properties of the semiconductor, and thereby changing the optical overlap of the semiconductor and Ag structures, while ensuring that the semiconductor particles were morphologically similar. This is important to ensure that the differences in photoactivity are due to changes in the charge carrier formation rate rather than changes in the inherent ability of the semiconductor to facilitate surface chemical transformations.

6.3 Methods

Evonik/Degussa P25 TiO_2 was used and N-TiO_2 was synthesized by heating P25 in NH^3 [40]. Ag nanocubes with edge length of ∼80 nm were synthesized using a modified polyol technique, as described in detail previously [41–43]. UV-visible extinction spectra of the resulting Ag cubes, TiO_2 and N-TiO_2 are shown in Figure 6.2a. Please consult the Synthesis section of Chapter 3 for detailed synthesis methods. Samples were prepared by spin coating successive layers of the constituent materials onto an inert transparent conductive support (fluorine-doped tin oxide (FTO)). The first step was spin coating a suspension of semiconductor particles (TiO_2 or N-TiO_2 in ethanol) on the FTO support. The weight of semiconductor particles was constant for each sample. A dilute solution of polyethylene glycol (PEG) in ethanol

was then applied on top of the semiconductor via spin coating. The thickness of the PEG layer was varied by changing the volume of PEG solution applied. The thickness of the spacer layer was estimated by applying the same volumes of PEG solution to a Si wafer and measuring the resulting PEG thickness using ellipsometry, as shown in Figure 6.2b. Finally, a constant volume of Ag nanocube suspension in ethanol was applied on top via spin coating. A UV-visible extinction spectrum of one of the finished composite samples is shown in Figure 6.2a. A schematic of the composite sample geometry is also shown in Figure 6.2c. More sample preparation information is given in the Sample Preparation section of Chapter 3. TiO_2 only and Ag/PEG/TiO_2 composite systems were placed in a photoelectrochemical cell with 1 M KOH, Pt counter-electrode and Hg/HgO reference electrode. The photocurrent was measured at a constant bias of 0.3 V upon illumination with a monochromatic 365 nm light source (5 mW/cm^2, 3 nm FWHM).

6.4 Results and Discussion

The enhancement in photocurrent (photocurrent for a composite Ag/PEG/TiO_2 sample divided by photocurrent for TiO_2 only) is shown in Figure 6.3a as a function of the thickness of the PEG spacer layer. The photocurrent enhancement varies from ∼2–4 times, with a maximum around 5 nm. The figure also shows that the photocurrent enhancement levels off to a constant value of ∼2 as the distance increases. As discussed above, the charge transfer enhancement mechanism mentioned above requires physical contact between metal and semiconductor [10, 11, 18, 44], which is prevented by the PEG layer in this system. At short distances the enhancement is attributed to the interaction of SPR-induced enhanced electric fields with the nearby semiconductor, increasing the concentration of charge carriers within the semicon-

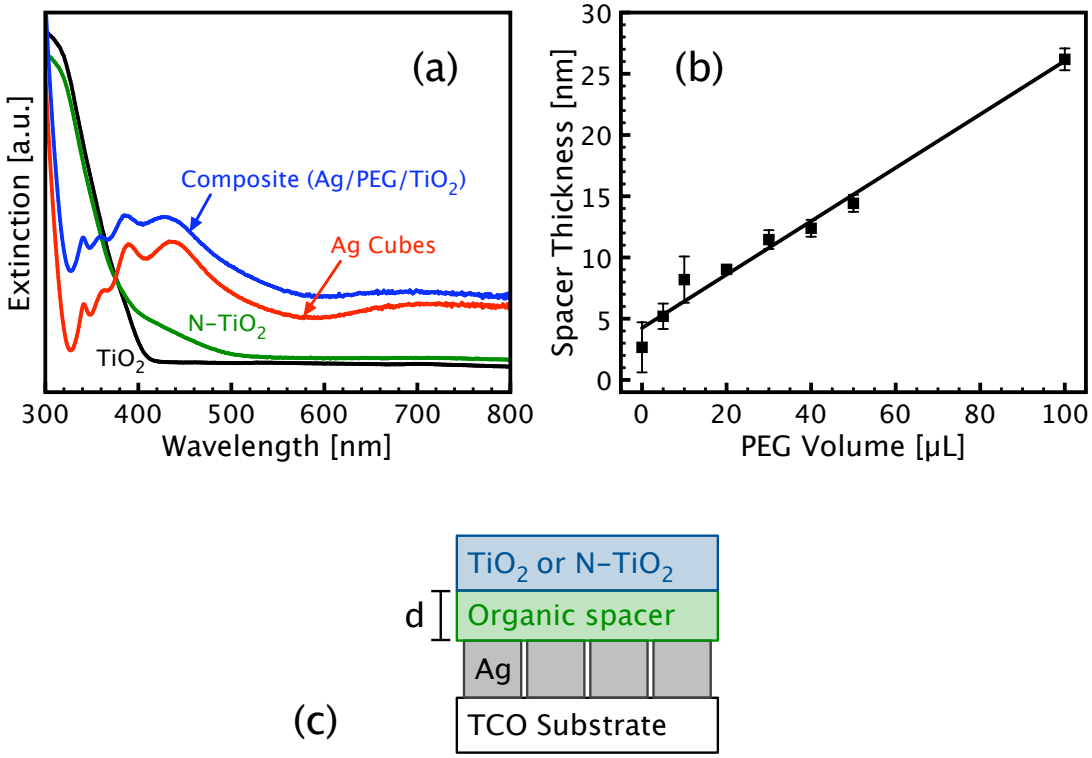

Figure 6.2: Characterization of the composite photocatalysts. (a) UV-visible spectra of 80-nm edge length Ag cubes, P25 TiO_2, N-TiO_2 and a composite Ag/PEG/TiO_2 sample with PEG thickness of ~5 nm. (b) Spacer layer thickness as a function of PEG solution applied, measured by ellipsometry. (c) Schematic illustration of the construction of a composite Ag/PEG/TiO_2 sample supported on a transparent conductive substrate (TCO).

ductor [12, 13, 15, 16, 19, 45]. As the distance between metal and semiconductor increases, the spatial overlap of the semiconductor with the SPR-induced fields decreases. In the limit of large distance the enhancement is driven by the far-field scattering phenomenon, which increases the average photon pathlength and thereby increases charge carrier formation [31–33].

A key experimental signature that indicates an increase in the formation of charge carriers in the semiconductor is increased photoluminescence (PL) emission from the semiconductor [13, 29, 39]. PL emission was measured for TiO_2 and Ag/PEG/TiO_2 samples upon illumination with 365 nm photons. Figure 6.3b shows the emission enhancement as a function of the spacer thickness. Emission enhancement was defined as emission at 467 nm for Ag/PEG/TiO_2 divided by that of TiO_2 only. The figure shows that TiO_2-based samples exhibit emission enhancement similar to the photocurrent enhancement from Figure 6.3a. The maximum emission enhancement occurs at a distance of $\sim$3–5 nm and again converges to a constant enhancement value of $\sim$2 as distance increases.

Figure 6.3b also shows a set of PL emission enhancement measurements from N-TiO_2-based composites (emission at 467 nm for Ag/PEG/N-TiO_2 divided by that of N-TiO_2 only) excited at a wavelength of 400 nm. These data again show an optimal spacing of $\sim$3–5 nm, with a significantly higher maximum enhancement value compared to TiO_2-based composites. A different excitation wavelength was chosen for N-TiO_2 in order to probe changing the overlap of the excited metal plasmon states with the semiconductor absorbance (i.e. when N-TiO_2 was excited at 365 nm, the system performance was identical to that of Ag/TiO_2). We note that photocurrent for N-TiO_2 was not measured in Figure 6.3a because a suitable monochromatic 400 nm source was not available.

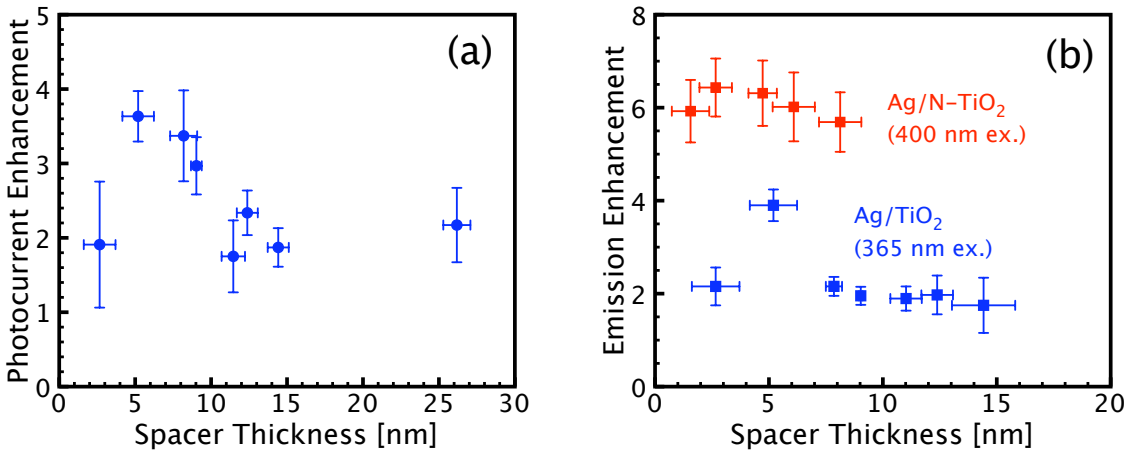

Figure 6.3: Photocurrent and photoluminescence enhancement as a function of spacer thickness. (a) Enhancement in the measured photocurrent for Ag/PEG/TiO_2 composite samples as a function of PEG thickness. Enhancement is calculated as the photocurrent for the composite sample divided by photocurrent for TiO_2 only. (b) Enhancement of photoluminescence emission for Ag/PEG/TiO_2 and Ag/PEG/N-TiO_2 composite samples as a function of PEG thickness. Enhancement is calculated as the emission for the composite sample, divided by the emission for the semiconductor-only sample (i.e. Ag/PEG/TiO_2 vs TiO_2 only and Ag/PEG/N-TiO_2 vs N-TiO_2 only). TiO_2 and the TiO_2-based composites were illuminated with 365 nm photons while N-TiO_2 and N-TiO_2-based composites were illuminated with 400 nm photons. Emission for all samples was measured at the 467-nm TiO_2 emission peak.

To quantitatively explain the effect of the spacer distance on the measured enhancement we must look at how the SPR-induced fields vary with distance. As discussed above, the SPR-induced EM fields are spatially non-homogeneous with maximum intensity enhancement of ∼1000 times near the surface of an excited Ag cube and dropping with approximately an exponential dependence on distance away from the particle (Figure 6.1). The rate of emission (γ), or charge carrier recombination, for a system is proportional to the product of the field intensity at the emission wavelength ($|E|^2_{em}$) and field intensity at the excitation wavelength ($|E|^2_{ex}$), as shown in Equation 6.1 [29, 30, 39].

$$\gamma \propto |E|^2_{\lambda_{\mathrm{ex}}} |E|^2_{\lambda_{\mathrm{em}}} \tag{6.1}$$

Therefore the total field-induced enhancement in the emission rate is given by Equation 6.2:

$$\frac{\gamma}{\gamma_0} = \left(\frac{|E|^2}{|E|^2_0}\right)_{\lambda_{\mathrm{ex}}} \left(\frac{|E|^2}{|E|^2_0}\right)_{\lambda_{\mathrm{em}}} \tag{6.2}$$

Field enhancements at the different wavelengths are captured by the FDTD simulation of an 80 nm Ag cube; Figure 6.4a shows the simulated UV-visible extinction spectrum. The enhancement of electric field intensity at the excitation wavelengths (365 nm for TiO_2 and 400 nm for N-TiO_2) and emission wavelength (467 nm for both) are shown in Figure 6.4b as a function of distance away from the surface of the Ag cube. As previously shown in Figure 6.1, the field enhancements are highest at the Ag cube surface and decrease with distance approximately proportional to 1/distance. However, the maximum field enhancements at these wavelengths are ∼5–15, much smaller than observed in Figure 6.1. This is because the fields plotted

in Figure 6.1 are on-resonance, i.e. Figure 6.1 shows the fields at the SPR peak (434 nm), whereas the fields in Figure 6.4b are shifted from the SPR peak.

The total predicted field-induced emission enhancement as a function of distance is calculated from Equation 6.2 using the FDTD simulation results in Figure 6.4b. The results are plotted in Figure 6.5b for both Ag/TiO_2 (λ_{ex} = 365nm and λ_{em} = 467nm) and Ag/N-TiO_2 samples (λ_{ex} = 400nm and λ_{em} = 467nm). The resulting emission enhancement for N-TiO_2 is larger across the distance range because the field enhancement at 400 nm is larger than that at 365 nm (see Figure 6.4b). For both samples the emission enhancement is highest at the surface of the Ag structure and decreases with distance. This suggests that the plasmonic metal particles and semiconductor particles should be placed close together, in order to maximize the spatial overlap of the SPR-enhanced fields with the semiconductor.

However, as discussed above, at small distances there are competing parasitic losses of charge carriers that must be considered. The non-radiative transfer of energy from the semiconductor to the metal SPR due to dipolar coupling (the FRET process) results in a loss of charge carriers in the semiconductor, thereby decreasing the reaction rate or emission rate. The efficiency of this process (η) is described by the FRET equation given in Equation 6.3 [30, 35–37].

$$\eta = \frac{R_0^6}{R_0^6 - d^6} \tag{6.3}$$

Where d is the distance between emitter (the semiconductor) and absorber (the plasmon-active metal) and R_0 is the Förster radius, which is defined as the distance between emitter/absorber pair that yields 50% FRET efficiency. The Förster radius can be calculated based on the system optical properties [35]. The most important factors dictating the Förster radius, and therefore the FRET efficiency, are the overlap between the emission spectrum of the emitter and the absorption spectrum

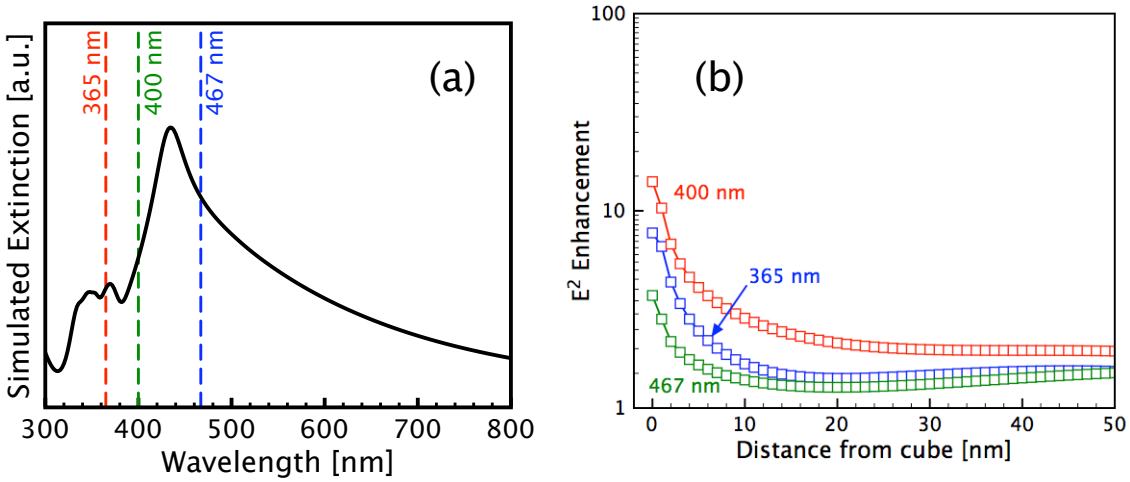

Figure 6.4: Simulated field intensities as a function of distance from an 80-nm Ag cube. (a) Extinction spectrum calculated from FDTD simulation of an 80-nm edge length Ag cube. (b) Enhancement in electric field intensity as a function of distance from the corner of an 80-nm edge length Ag cube. Fourier transformed fields are shown at 365 nm (TiO_2 excitation wavelength), 400 nm (N-TiO_2 excitation wavelength) and 467 nm (emission wavelength for both).

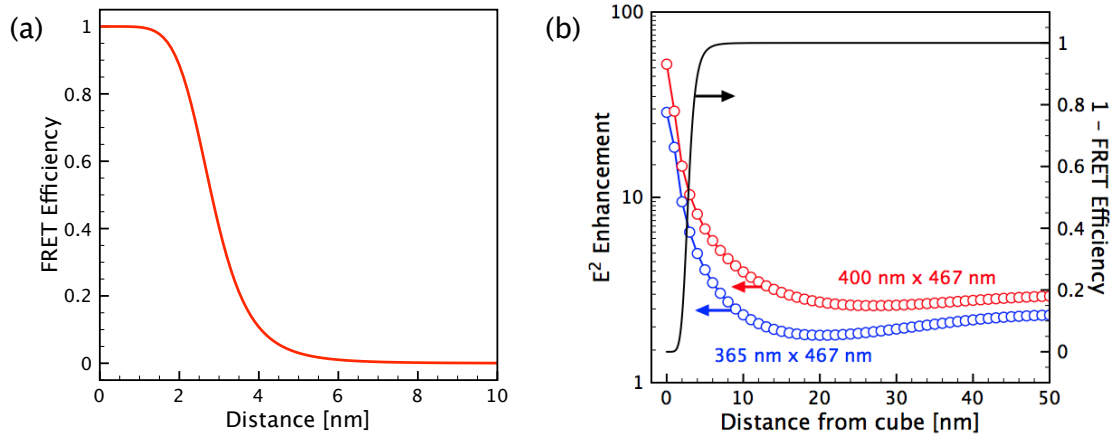

Figure 6.5: FRET efficiency and total field enhancement as a function of distance. (a) Efficiency of the Förster resonance energy transfer (FRET) process as a function of distance between the emitter/absorber pair, calculated from Equation 6.3. (b) (Left ordinate) Total electric field intensity enhancement as a function of distance from the cube corner. Total field enhancement is calculated as the product of the excitation field enhancement and the emission field enhancement, shown in Figure 6.4 (365 nm and 467 nm for TiO_2 or 400 nm and 467 nm for N-TiO_2). The black curve (right ordinate) shows one minus the FRET efficiency as a function of distance from the Ag cube.

of the absorber. If there is no spectral overlap between the emitter and absorber, the Förster radius is zero and therefore the FRET efficiency is zero. Stronger spectral overlap between the emitter and absorber pair leads to an increase in FRET efficiency. R_0 and η also depend on the refractive index of the medium separating the emitter/absorber pair, with higher refractive indices attenuating the transfer process. Published values of the Förster radius for different emitter/absorber pairs typically range from approximately 2 to 8 nm [35]. For the present Ag/TiO_2 and Ag/N-TiO_2 systems we have estimated R_0 to be approximately 3 nm and we note that small changes within the typical range should not significantly alter the results. The FRET efficiency indicates the fraction of charge carriers in the semiconductor lost via the FRET process. The fraction of photons not lost via FRET (i.e. one minus the FRET efficiency), is plotted in Figure 6.5a.

The total enhancement of PL emission is a compromise between the two phenomena discussed above. On one hand the EM field enhancement (and hence enhancement in charge carrier generation in the semiconductor) is highest very close to the plasmon-active metal particles. On the other hand the parasitic loss of charge carriers in the semiconductor due to the FRET process is also high very close to the surface of the metal. In fact, the theoretical FRET efficiency (percentage of charge carriers lost) is 100% at the interface of touching semiconductor and metal particles (d = 0), meaning that emission is quenched rather than enhanced regardless of the enhancement of EM field intensity [30]. In reality, because the particles have non-infinitessimal volume (as would a small molecule, for example), two touching particles may still show enhancement because there are always regions of the particles that are separated by some distance, and therefore the average FRET efficiency within the system will be less than 100%.

The total predicted emission enhancement is given by the product of the SPR-induced enhancement (Equation 6.2) and the fraction of charge carriers not lost via FRET (i.e. one minus the FRET efficiency). These individual quantities are plotted in Figure 6.5 and the resulting predicted emission enhancement is shown in Figure 6.6 for both the Ag/TiO_2 and Ag/N-TiO_2 systems. The predicted enhancements for both systems show similar results. At small d values the behavior is dominated by parasitic losses due to the high FRET effiency, resulting in small enhancement values. At large d values (greater than ∼6 nm) the efficiency of the FRET process is approximately zero and the enhancement is governed by the SPR-enhanced EM fields. Both systems exhibit maximum enhancement at approximately d = 5 nm; the Ag/N-TiO_2 system has a higher maximum value because the SPR-induced field enhancement at the excitation wavelength (400 nm) is higher than for Ag/TiO_2. The experimental measurements of emission enhancement and photocurrent enhancement (from Figure 6.3) are also plotted in Figure 6.6 and show good agreement with the model predicted enhancement values.

These conclusions have important ramifications on the design of composite metal/semiconductor photocatalysts. The SP-induced EM fields are highest at the metal particle surface, suggesting that a small metal/semiconductor separation is beneficial. However as shown above, the parasitic loss of charge carriers is very high for small separation distances. A compromise between these two phenomena is necessary in order to achieve high activity enhancement factors. This suggests that when designing such a composite system, a spacer layer around the metal nanoparticles may be necessary to prevent charge carrier quenching. However, it is important to again note here that when the metal and semiconductor particles are in direct contact, charge transfer from metal to semiconductor may occur, increasing the concentration of electrons

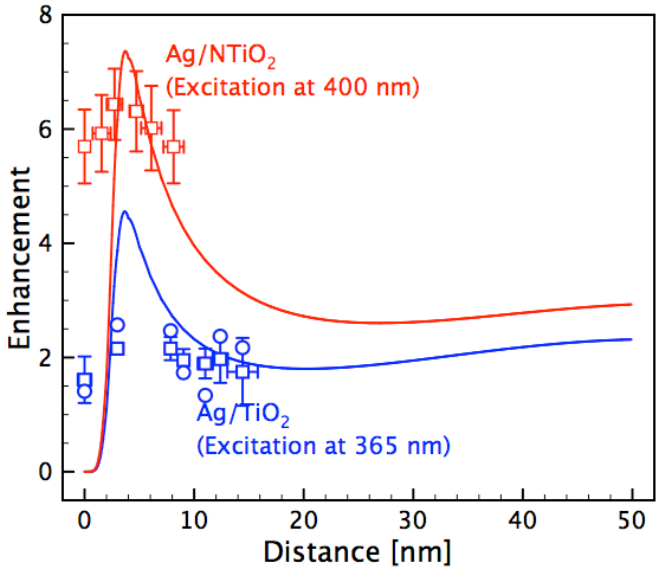

Figure 6.6: Model prediction versus experimental data. Lines: enhancement model calculated as the product of the total field enhancement and one minus FRET efficiency (Figure 6.5) at an excitation wavelength of 365 nm (blue) and 400 nm (red). Square points: Experimental PL emission enhancement as a function of distance from Figure 6.3 for Ag/TiO_2 excited at 365 nm (blue) and $Ag/N\text{-}TiO_2$ (red) excited at 400 nm. Circles: Experimental photocurrent enhancement as a function of distance from Figure 6.3 for Ag/TiO_2 composite samples illuminated with a 365 nm light source.

in the semiconductor. This would increase the measured photocurrent as well as the rate of electron-driven processes (e.g. the H_2 evolution half-reaction). Indeed, modest increases in photocurrent and H_2 evolution are generally observed, even with the particles in contact. However, it is not clear that this would increase the rate of the hole-driven O_2 evolution half-reaction, since the potential of the holes left in the metal is likely too low to drive this reaction. For this reason, one may expect to observe decreases in the rates of hole-driven processes (O_2 evolution) due to parasitic losses when the particles are in direct contact, although this has yet to be demonstrated. However, we also note that there is some suggestion that the holes may have sufficient potential when localized on very small metal particles [17, 18].

6.5 Conclusion

In conclusion, we have demonstrated how the SPR-induced enhancement in charge carrier formation in a semiconductor, and hence the activity, is a function of the distance between metal and semiconductor particles. The model constructed here provides insight into how the nano-scale building blocks should be geometrically arranged to create the optimal plasmonic metal/semiconductor composites. The SP-induced fields are highest near the metal particle surface; however, the results presented here suggest that a spacer layer is necessary to prevent high rates of charge carrier quenching via Förster transfer. Direct charge transfer from metal to semiconductor may to some degree offset the observation of charge carrier quenching, particularly when monitoring electron-driven quantities (e.g. photocurrent).

References

[1] Linsebigler, A. L.; Lu, G.; Yates, Jr., J. T. *Chem. Rev.* **1995**, *95*, 735–758.

[2] Fujishima, A.; Rao, T. N.; Tryk, D. A. *J. Photochem. Photobio. C* **2000**, *1*, 1–21.

[3] Fujishima, A.; Zhang, X.; Tryk, D. A. *Surf. Sci. Rep.* **2008**, *63*, 515–582.

[4] Goldberger, J.; He, R.; Zhang, Y.; Lee, S.; Yan, H.; Choi, H.-J.; Yang, P. *Nature* **2003**, *442*, 599–602.

[5] Cesar, I.; Kay, A.; Martinez, J. A. G.; Grätzel, M. *J. Am. Chem. Soc.* **2006**, *128*, 4582–4583.

[6] Cesar, I.; Sivula, K.; Kay, A.; Zboril, R.; Grätzel, M. *J. Phys. Chem. C* **2009**, *113*, 772–782.

[7] Mor, G. K.; Shankar, K.; Paulose, M.; Varghese, O. K.; Grimes, C. A. *Nano Lett.* **2005**, *5*, 191–195.

[8] Zhu, K.; Neale, N. R.; Miedaner, A.; Frank, A. J. *Nano Lett.* **2007**, *7*, 69–74.

[9] Maiolo III, J. R.; Kayes, B. M.; Filler, M. A.; Putnam, M. C.; Kelzenberg, M. D.; Atwater, H. A.; Lewis, N. S. *J. Am. Chem. Soc.* **2007**, *129*, 12346–12347.

[10] Tian, Z.-Q.; Ren, B. *Annu. Rev. Phys. Chem.* **2004**, *55*, 197–229.

[11] Tian, Y.; Tatsuma, T. *J. Am. Chem. Soc.* **2005**, *127*, 7632–7637.

[12] Awazu, K.; Fujimake, M.; Rockstuhl, C.; Tominaga, J.; Murakami, H.; Ohki, Y.; Yoshida, N.; Watanabe, T. *J. Am. Chem. Soc.* **2008**, *130*, 1676–1680.

[13] Christopher, P.; Ingram, D. B.; Linic, S. *J. Phys. Chem. C* **2010**, *114*, 9173–9177.

[14] Kowalska, E.; Mahaney, O. O. P.; Abe, R.; Ohtani, B. *Phys. Chem. Chem. Phys.* **2010**, *12*, 2344–2355.

[15] Kumar, M. K.; Krishnamoorthy, S.; Tan, L. K.; Chiam, S. Y.; Tripathy, S.; Gao, H. *ACS Catal.* **2011**, *1*, 300–308.

[16] Ingram, D. B.; Linic, S. *J. Am. Chem. Soc.* **2011**, *133*, 5202–5205.

[17] Silva, C. G.; Juárez, R.; Marino, T.; Molinari, R.; García, H. *J. Am. Chem. Soc.* **2011**, *133*, 595–602.

[18] Primo, A.; Corma, A.; García, H. *Phys. Chem. Chem. Phys.* **2011**, *13*, 886–910.

[19] Liu, Z.; Hou, W.; Pavaskar, P.; Aykol, M.; Cronin, S. B. *Nano Lett.* **2011**, *11*, 1111–1116.

[20] Hou, Y.; Abrams, B. L.; Vesborg, P. C. K.; Björketun, M. E.; Herbst, K.; Bech, L.; Setti, A. M.; Damsgaard, C. D.; Pedersen, T.; Hansen, O.; Rossmeisl, J.; Dahl, S.; Nørskov, J. K.; Chorkendorff, I. *Nat. Mater.* **2011**.

[21] Subramanian, V.; Wolf, E.; Kamat, P. V. *J. Phys. Chem. B* **2001**, *105*, 11439–11446.

[22] Arabatzis, I. M.; Stergiopoulos, T.; Bernard, M. C.; Labou, D.; Neophytides, S. G.; Falaras, P. *Appl. Catal. B* **2003**, *42*, 187–201.

[23] Subramanian, V.; Wolf, E. E.; Kamat, P. V. *J. Am. Chem. Soc.* **2004**, *126*, 4943–4950.

[24] El-Sayed, M. A. *Acc. Chem. Res.* **2001**, *34*, 257–264.

[25] Kelly, K. L.; Coronado, E.; Zhao, L. L.; Schatz, G. C. *J. Phys. Chem. B* **2003**, *107*, 668–677.

[26] Brus, L. *Acc. Chem. Res.* **2008**, *41*, 1742–1749.

[27] Grätzel, M. *Nature* **2001**, *414*, 338–344.

[28] Youngblood, W. J.; Lee, S.-H. A.; Kobayashi, Y.; Hernandez-Pagan, E. A.; Hoertz, P. G.; Moore, T. A.; Moore, A. L.; Gust, D.; Mallouk, T. E. *J. Am. Chem. Soc.* **2009**, *131*, 926–927.

[29] Lee, J.; Javed, T.; Skeini, T.; Govorov, A. O.; Bryant, G. W.; Kotov, N. A. *Angew. Chem. Int. Ed.* **2006**, *45*, 4819–4823.

[30] Anger, P.; Bharadwaj, P.; Novotny, L. *Phys. Rev. Lett.* **2006**, *96*, 113002–1–4.

[31] Derkacs, D.; Lim, S. H.; Matheu, P.; Mar, W.; Yu, E. T. *Appl. Phys. Lett.* **2006**, *89*, 093103.

[32] Pala, R. A.; White, J.; Barnard, E.; Liu, J.; Brongersma, M. L. *Adv. Mater.* **2009**, *21*, 1–6.

[33] Atwater, H. A.; Polman, A. *Nat. Mater.* **2010**, *9*, 205–213.

[34] Matheu, P.; Lim, S. H.; Derkacs, D.; McPheeters, C.; Yu, E. T. *Appl. Phys. Lett.* **2008**, *93*, 113108.

[35] VanDerMeer, B. W.; Coker, G.; Chen, S. Y. S. *Resonance Energy Transfer: Theory and Data*; Wiley, New York, 1994.

[36] Clegg, R. M. *Current Opinion in Biotechnology* **1995**, *6*, 103–110.

[37] Govorov, A. O.; Lee, J.; Kotov, N. A. *Phys. Rev. B* **2007**, *76*, 125308.

[38] Torimoto, T.; Horibe, H.; Kameyama, T.; ichi Okazaki, K.; Ikeda, S.; Matsumura, M.; Ishikawa, A.; Ishihara, H. *J. Phys. Chem. Lett.* **2011**, *2*, 2057–2062.

[39] Lee, J.; Govorov, A. O.; Dulka, J.; Kotov, N. A. *Nano Lett.* **2004**, *4*, 2323–2330.

[40] Irie, H.; Watanabe, Y.; Hashimoto, K. *J. Phys. Chem. B* **2003**, *107*, 5483–5486.

[41] Christopher, P.; Linic, S. *ChemCatChem* **2010**, *2*, 78–83.

[42] Christopher, P.; Xin, H.; Linic, S. *Nat. Chem.* **2011**, *3*, 467–472.

[43] Im, S. H.; Lee, Y. T.; Wiley, B.; Xia, Y. *Angewandte Chemie* **2005**, *44*, 2154–2157.

[44] Kowalska, E.; Abe, R.; Ohtani, B. *Chem. Comm.* **2009**, 241–243.

[45] Hou, W.; Liu, Z.; Pavaskar, P.; Hung, W. H.; Cronin, S. B. *J. Catal.* **2011**, *277*, 149–153.

CHAPTER 7

Conclusions and Future Outlook

7.1 Semiconductor Photocatalysts

It has been known for several decades that certain semiconductors can absorb photons in the UV-visible portion of the electromagnetic spectrum, and use the absorbed energy to activate water, producing hydrogen and oxygen. This phenomenon, called the Fujishima-Honda effect [1], was discussed in detail in Chapter 2. While this technology has been investigated for 40 years, the process produces hydrogen at very low rates because of inherent deficiencies of the semiconductors. More recent progress has demonstrated that adding metal nanoparticles to the semiconductor can enhance the photocatalytic rates through a variety of phenomena [2**?** –20].

7.2 Composite Plasmonic Metal/Semiconductor Photocatalysts

If the metal nanoparticles are specially tailored they can also interact with the UV-visible photons through the excitation of surface plasmons [21–24]. Very recently it was demonstrated that this interaction of photo-excited plasmonic metal nanoparticles with a semiconductor is potentially a much more powerful way to enhance the semiconductor activity [6**?** –20]. We have demonstrated that the addition of photo-excited plasmonic metal nanoparticles can enhance the photo-activity of both TiO_2 and nitrogen-doped TiO_2 (N-TiO_2) as measured by the rate of the decomposition

of methylene blue (Chapter 4). We also demonstrated the design and analysis of a composite plasmonic metal/semiconductor photocatalyst (Ag/N-TiO_2) that exhibits enhanced rates of H_2 and O_2 evolution from water (overall water splitting) under a visible light source, compared to the rate on the N-TiO_2 semiconductor alone (Chapter 5) [16]. Through a series of supporting experiments, the enhancement in both reactions was ascribed to the SPR-induced spatially non-homogeneous enhancement and concentration of electric fields around the Ag nanoparticles, which then increase the rate of charge carrier formation in the semiconductor. Specifically, we presented evidence that the non-homogeneous SPR-enhanced fields enhanced charge carrier formation rate selectively near the semiconductor surface (Chapter 5).

A number of other possible mechanisms were discussed, for example the role of the far-field scattering mechanism and charge transfer at the metal/semiconductor interface. Each mechanism was seen to play a minor role in the particular systems studied; however, these alternatively mechanisms can also be the dominant effects in other systems and/or under other conditions, as discussed throughout (especially Chapter 2). Most studies—including the majority of those presented in this dissertation—have used system designed to exhibit only one dominant mechanism. This was useful, as it allowed us to separate the mechanisms and directly probe the near-field electromagnetic mechanism. However, this also means that the analysis cannot provide a direct comparison between the competing mechanisms. As such, it remains to be seen which of the enhancement mechanisms has the greatest potential to ultimately produce the best possible photocatalyst for the production of solar fuels. It will be important in the future to perform more systematic studies using systems flexible enough to permit the investigation and comparison of all the various mechanisms.

7.3 Design Criteria

To investigate the effect of the optical properties of the individual building blocks on the composite activity, we measured the photo-activity of composite photocatalysts with two different semiconductors (TiO_2 and N-TiO_2), two different plasmonic metals (Ag and Au) and different relative amounts of the building blocks (Chapter 4). This gave us several ways to change the composite optical properties and compare this to the measured rate enhancements. We showed that the optical overlap between the illumination source spectrum, semiconductor absorbance spectrum and metal nanoparticle SPR spectrum provides a useful descriptor for predicting the SPR-induced rate enhancement for composite photocatalysts of similar geometries (Chapter 4). This simple model is useful for guiding the formulation of optimal plasmonic metal/semiconductor photocatalysts, under the assumption that comparisons are made between systems of the same geometry (same arrangement of the building blocks) and where the enhancement is dominated by the near-field electromagnetic mechanism. Data presented in Chapter 5 showed that the spatial distribution of the SPR-enhanced fields was an important factor in these systems. Therefore it will be important in the future to expand this simple optical model to make it robust enough to compare systems with different geometries, as well as build in the effects of the other mechanisms that could dominate some systems.

As a start to building more robust models that incorporate the crucial importance of the spatial distribution of SPR-enhanced fields, we demonstrated how the SPR-induced enhancement in charge carrier formation in a semiconductor, and hence the activity, is a function of the distance between metal and semiconductor particles (Chapter 6). The model provides insight into how the nano-scale building blocks

should be geometrically arranged to create the optimal plasmonic metal/semiconductor composites. The SPR-induced fields are highest near the metal particle surface; however, the results presented here suggest that a spacer layer is necessary to prevent high rates of charge carrier quenching via Förster transfer. However, even this more detailed model did not allow for the direct investigation of all the possible mechanisms (all the systems had a small insulating layer, preventing the direct charge transfer mechanisms). Future work will need to build on the foundations laid here, include all the possible mechanisms discussed throughout this document, and allow for the identification and analysis of optimal composite metal/semiconductor photocatalysts.

7.4 Future Outlook

The previous chapters and the sections above, have discussed the effect of adding photo-excited plasmonic metal particles to a semiconductor, and the resulting observed enhancements in photo-activity. However, a number of practical problems still need to be addressed. This section discusses some of these issues and potential solutions that are being investigated throughout the literature in parallel with the material presented in this dissertation. The hope is that combing the enhancement effects due to plasmonic nanoparticles with some of the other activity-enhancing strategies discussed below, the result will be photocatalysts with even higher activities, with the ultimate goal being the realization of highly efficient, cost effective systems for the production of solar fuels.

7.4.1 Efficiency

One of the main issues plaguing the use of photocatalysts in general is that of the overall efficiency of transforming solar energy into useful chemicals and fuels. While

the total energy provided by the sun globally (average rate of ∼120,000 TW [25, 26]) is massive, on a per surface area basis, the solar flux is actually quite diffuse. For example, in Michigan the solar flux during sunlight hours is on the order of 100 mW/cm^2, which means that approximately 10^{17} solar photons impinge on a surface area of 1 cm^2 each second. The result is that for a theoretical two-dimensional semiconductor surface only ∼100 solar photons collide with one surface atomic site (typical area of 10 $Å^2$) each second. This photo-impingement rate sets an upper bound on the maximum possible rate of photo-catalytic transformations. In order to produce solar fuels at high rates, while minimizing the required land area (more on this below), photocatalysts must be optimized to achieve high efficiencies at channeling the energy of these incident photons into useful chemical transformations.

There are a number of different metrics by which to measure photocatalyst efficiency. We will discuss these quantities below with respect to the overall water splitting reaction; however, they can easily be adapted to measure the efficiency of any photo-process. The best measure is the amount of chemical energy produced in the form of H_2 and O_2 produced divided by the total amount of energy input (energy of illumination and external potential bias). This quantity is referred to as the power conversion efficiency, or simply conversion efficiency. The energy of the H_2 and O_2 produced is given by the standard Gibbs free energy of the water splitting reaction ($H_2O \longrightarrow H_2 + 1/2O_2$), $\Delta G^0 = 273.2 kJ mol^{-1}$ (per mole of H_2O). The rate of chemical energy production is then given by multiplying ΔG^0 by the rate at which H_2O is converted to H_2 and O_2. In a photoelectrochemical (PEC) cell it is common to measure the photocurrent, which is proportional to the water splitting rate, rather than directly measuring the rate of H_2 and O_2 production. In this case, the resulting equation to calculate the rate of chemical energy production, $\dot{E}$, is given by Equation

7.1 [27].

$$\dot{E} = \frac{\Delta G^0}{zF} I \tag{7.1}$$

Where z is the number of electrons transferred per H_2O molecule ($z = 2$), F is the Faraday constant and I is the photocurrent. The quantity ΔG^0 divided by twice the Faraday constant is 1.23 V, the standard potential of the water splitting reaction. Using the photocurrent in lieu of the actual H_2 production rate assumes that every electron transferred through the external circuit (i.e. the photocurrent) goes to forming H_2. This is generally a reasonable assumption, but using the measured H_2 production rate (when available) would be more accurate. If we take into account the amount of applied external potential bias (U_{appl}), as discussed in Chapter 2, the power conversion efficiency (η) then is given by Equation 7.2 [27].

$$\eta = \frac{I}{P}(1.23V - U_{appl}) \tag{7.2}$$

Where P is the total power of the photon flux delivered to the photocatalyst surface.

Other common measures of efficiency are incident photon conversion efficiency (IPCE), sometimes referred to as external quantum yield, and absorbed photon conversion efficiency (APCE), sometimes called internal quantum yield. IPCE is simply defined as the number of electrons produced divided by the number of photons striking the sample, whereas APCE is the number of electrons normalized by the number of photons absorbed by the sample. Equations 7.3 and 7.4 define IPCE and APCE for a monochromatic source.

$$\text{IPCE} = \frac{hcI}{e_0 \lambda P} \tag{7.3}$$

$$\text{APCE} = \frac{hcI}{e_0 \lambda P A} \tag{7.4}$$

Where h is the Planck constant, c is the speed of light, e_0 is the fundamental charge of an electron and A is the fraction of photons of wavelength λ absorbed

by the photocatalyst (measured by an appropriate optical spectroscopy method, see Chapter 3). Note that APCE will never exceed IPCE since A cannot exceed 1. The quantities are often similar in many photocatalytic systems because the photo-electrodes are relatively thick and nearly all photons with energy exceeding the band gap are absorbed. Because of these definitions, it is common to see these quantities used for experiments employing a monochromatic light source (e.g. action spectra). When analyzing a broadband source, particularly a standardized sunlight source such as AM1.5, it is common to use conversion efficiency. Unfortunately, the number of different metrics available in conjunction with the non-standardized set of illumination sources makes it very difficult to directly compare figures from literature. Ultimately the figure of merit is how much hydrogen can be produced from sunlight using an apparatus covering a given land area. But other efficiency metrics are common and indeed useful on the lab scale. Many studies attempt to present the results as we have done throughout this document: in comparison to some baseline figure, i.e. it is useful to show the enhancement of the rate due to some modification of the catalyst, rather than simply the absolute rate. Ultimately, when studies attempt to set some record for the highest absolute efficiency or water splitting rate, the experiments should be performed with solar illumination in order to facilitate comparison across studies.

For these reasons, one must be careful when comparing conversion efficiency values for different sources. For example, to our knowledge the highest reported conversion efficiency in literature is 16.25% for a TiO_2 nanotube array with external bias [28]. However, these experiments used a light source with wavelengths of 320–400 nm; had they used sunlight the conversion efficiency would be much lower because visible light ($\sim$95% of sunlight) cannot be absorbed by TiO_2. In fact, un-doped anatase TiO_2

is limited to an absolute maximum solar conversion efficiency of ∼5% because of this reason. One approach to surmount this problem is to add dopants, as discussed throughout this document, and doing so extends the absorption of TiO_2 into the visible region of the spectrum. However, this is accompanied by a decrease in the UV-light absorbance and very high levels of dopants may not be stable over time.

Another method to increase the efficiency of a semiconductor is to improve the microstructure. Photocatalyst films constructed of nanoparticles, as used in the experiments throughout this dissertation, exhibit very low efficiencies [27]. This is illustrated in Figure 7.1, which shows the internal quantum yield values (APCE) as a function of wavelength for the water splitting experiments in Chapter 5. The low efficiency for nanoparticle photocatalysts is due primarily to poor electron transport; essentially, electrons must hop from particle to particle through the film before they can reach the current collector and be conducted around the external circuit [27, 29]. One method to address this problem is the use of mesoporous semiconductor films, which provide a semi-continuous path for electron transport to the current collector, which still maintaining porosity and reasonable microscopic surface area. Figure 7.2 shows measured photocurrent, APCE and IPCE for a mesoporous TiO_2 film under illumination with a monochromatic 365-nm light source (∼5 mW/cm^2). Comparison with Figure 7.1 shows that the efficiency is increased by approximately 10-fold (the total weight of TiO_2 is the same in both cases); this efficiency increase has also been reported in the literature [27]. Figure 7.2 also shows that addition of photo-excited Ag nanocubes (100 nm edge length) enhances the generation of photocurrent by a factor of 3–4, consistent with the results presented in Chapter 5. Another route that uses the same concept is the use of quasi-one-dimensional morphologies such as nanotubes [28, 30–40]. These structures improve efficiency even more because the

electron transport is even greater down the length of the tube, while the distance holes must travel to reach the semiconductor/liquid interface is very small (the upper limit is half of the tube wall thickness). These geometries may be even more favorable structures for the addition of plasmonic metal nanoparticles, which could be loaded into the tubes, but this has yet to be demonstrated.

Another route to improved efficiencies, of course, is the use of different semiconductors. There are many attributes that must be optimized (band positions, charge carrier mobility, stability, etc.). These were discussed in some detail in Chapter 2 so we will not repeat the entire list here. Suffice it to say that many advances with semiconductor materials have been made recently, which address some of the problems discussed throughout this thesis, but no perfect water splitting photocatalyst has been found. A variety of materials have shown promise, including GaAs [41], GaN [30] and Si/Mo_2C [42]; however, all of these materials still have problems precluding wide-spread use (mostly long-term stability and relatively low natural abundance and therefore higher cost). Hematite phase Fe_2O_3 has some favorable properties over TiO_2 as a semiconductor photocatalyst (mostly the narrower band gap) while still being very abundant and inexpensive. While hematite has many faults (as discussed in Chapter 2), some progress has been made recently mostly by improving the microstructure and by adding dopants to improve the charge mobility [18, 43–50]. Even still, hematite exhibits relatively low maximum solar conversion efficiencies because of its high charge carrier recombination rate and low absorbance efficiency due to the indirect band gap. Whatever materials end up being used, we have every reason to believe that the addition of plasmonic nanoparticles, when correctly optimized, should continue to enhance the semiconductor activity.

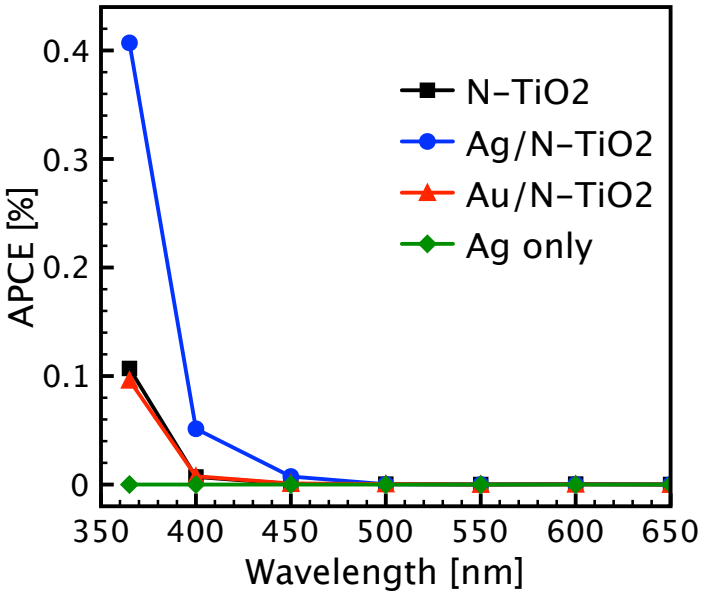

Figure 7.1: Absorbed photon conversion efficiency (APCE) as a function of wavelength for water splitting photo-electrodes from Chapter 5. APCE was calculated from Equation 7.4 for N-TiO_2 only, Ag only, Au/N-TiO_2 composite and Ag/N-TiO_2 composite samples.

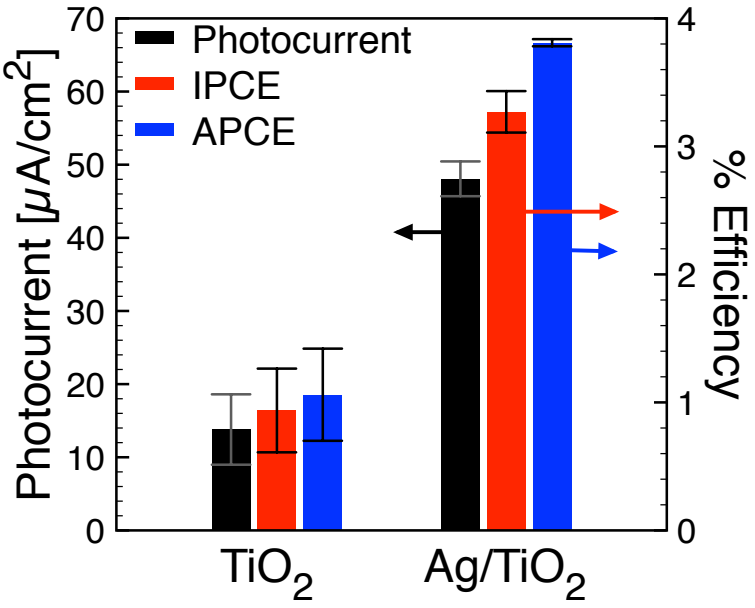

Figure 7.2: Performance of meso-porous TiO_2 with and without addition of Ag nanocubes under UV light (365 nm). Photocurrent is plotted on the left axis, while APCE and IPCE are both plotted on the right axis.

7.4.2 Stability of Metal Nanoparticles

We discussed above (and in Chapter 2) that stability is a key factor to consider when investigating potential semiconductor photocatalyst. However, stability of the metal nanoparticles in a metal/semiconductor photocatalyst is also an important consideration. The metal nanoparticles must be stable under illumination in water, which is true of Ag and Au, but would certainly be a concern if Cu nanoparticles were used. Furthermore, although Ag is generally stable in water, at electric potentials in the range of interested for water splitting, there are several Ag oxidation reactions that are potentially relevant [51, 52]. While formation of small amounts of surface oxides is not expected to significantly affect the plasmon resonance of Ag particles [53], over time large-scale oxidation formation or even dissolution of Ag ions into solution could be a worry.

To prevent large-scale oxidation and also to prevent the deleterious quenching effects discussed in Chapter 6, it is desired to coat the plasmonic nanoparticles with an inert, electrically insulating shell. The shell must be transparent to the source illumination in order to allow the excitation of the metal SPR. This was accomplished in the studies within this dissertation by coating the metal particles with organic polymers—polyvinylpyrrolidone (PVP) or polyethylene glycol (PEG). While this works on the lab time scale for a period of several hours, it is clear that organic molecules cannot be used over long periods of time. The polymers are both reasonably soluble in water, which means they will leach off into solution. Furthermore, as discussed in Chapters 2 and 4, semiconductor photocatalysts can catalyze the decomposition of many organic compounds and because of this, over the course several hours TiO_2 can facilitate the oxidation of PVP (and most likely PEG also) [10, 53].

A better route is to cap the metal nanoparticles with an inorganic shell, such as

SiO_2. Several excellent methods exist to synthesize spherical Ag nanoparticles with SiO_2 shells and the application of these core-shell structures has been demonstrated in the literature with varying levels of success [9, 14, 54]. However, as discussed in Chapter 4 and elsewhere [10], cubic Ag nanoparticles are more desirable than spheres and currently it is not clear how to synthesize core-shell particles with cubic geometry. Our initial attempts at this synthesis have been unsuccessful and have also demonstrated that the addition of SiO_2 to a TiO_2 film can dramatically decrease photo-activity under some conditions. In the long run, if the cubic core-shell synthesis cannot be achieved, it may be better to use Ag spheres, sacrificing some initial performance for greater long-term stability.

7.4.3 Large-Scale Design and Implementation

Even if the material design, synthesis and optimization problems discussed above and in previous chapters can be solved, there are still several questions to be answered regarding the large-scale production of solar fuels from water splitting, regardless of the specific photocatalyst materials used. While these broad issues are outside the technical scope of this dissertation, they do warrant some discussion, as these issues are important justifications for the importance placed on the scientific pursuit of high efficiency water splitting photocatalysts.

One of the primary concerns for solar water splitting, and indeed all solar technologies, is the land area required for mass implementation. As mentioned in Chapter 1, the total average rate at which energy is supplied from the sun to Earth's surface is approximately 120,000 TW [25, 26]. If we assume a large-scale water splitting implementation could achieve 10% total efficiency of solar energy (not unreasonable based on the current state-of-the-art), this means we have a total of 12,000 TW of realizable solar energy if we were to cover the entire surface area of the Earth (in-

cluding water). Since each mole of H_2 produced from water requires 273 kJ (ΔG of the water splitting reaction, $H_2O \longrightarrow H_2 + 1/2O_2$), this yields a maximum average H_2 production capacity of 8.8610^7 kg of H_2 each second if we cover the entire Earth's surface area. Obviously it is not possible to cover the entire Earth's surface with photo-reactors, but luckily we do not need to produce this much hydrogen either. In 2009 the total global consumption of petroleum was 85.3 million barrels per day [25]. From each 42-gallon barrel of crude oil, ∼19 gallons of gasoline and ∼10 gallons of diesel fuel were produced [25]. Taking into account the gallons of gasoline equivalent (GGE) rating of diesel and hydrogen, on an energy basis this is equivalent to an average worldwide consumption rate of 29,900 kg of hydrogen every second for transportation fuel. Taking the ratio of this required hydrogen rate to the maximum global solar hydrogen production capacity (assuming 10% efficiency), this means that we must cover 0.034% of the Earth's total surface area (0.12% of the land area), or approximately 172,000 square kilometers.* The is an enormous area to be sure, but to put it in perspective, the area of Michigan's lower peninsula is approximately 167,000 square kilometers. Even more surprising is that the estimated area of all paved surfaces (roads, parking lots and structures, etc.) in the United States is approximately 160,000 square kilometers [55]! To think that paving of this surface area was initiated only within the last 100 years, and that it is continuously re-paved, gives some hope for the utilization of solar energy to meet national and global fuel demands (see Figure 7.3 for a summary of these land area comparisons). Land is not the only required resource; production of H_2 on this scale requires a massive input of water. The water is regenerated when the H_2 is combusted or used in a fuel cell, so in a sense it is recyclable. However, the H_2 production infrastructure

*Note that this analysis was based only on global consumption of gasoline and diesel. Transportation fuels account for approximately 25% of global energy usage so the minimum required area (at 10% solar conversion efficiency) to meet total global energy demands would be approximately 700,000 square km.

would require a huge initial charge of water, and it remains to be seen how drastic changes to the global water cycle would affect climates and ecosystems. Although, it is not clear how pure the water would need to be for long-term operation, but it may be possible to satisfy some or all of the water demand using seawater.

We also note that this analysis is not specialized to water splitting technologies—all we have assumed is that 10% solar conversion efficiency can be realized. There are a large number of possible solar technologies that could potential reach this efficiency number on a reasonably large scale, for example, photocatalytic water splitting, photothermal processes, photovoltaic processes, etc. It remains to be seen which process will be the most efficient and economical, particularly at the massive scales required. Most likely, for the near future at least, we will have to pursue a mixture of all these different technologies.

Another economic concern is the direct monetary cost of the photocatalytic systems. For this reason, as stressed throughout several previous chapters, it is important that the selected semiconductor materials are inexpensive, which requires a high natural abundance or facile, scalable synthesis from materials with high natural abundance. The materials used on the lab scale are, by and large, highly abundant in nature and very inexpensive (e.g. semiconductors such as TiO_2 or Fe_2O_3). The notable exception to this is the counter-electrode used in the PEC cell, which is typically constructed of Pt. Because the hydrogen evolution half-reaction on Pt is very rapid, compared to oxygen evolution at a semiconductor photo-electrode, the Pt counter-electrode does not need to have a large area. However, high conductivity is required, and even a thin coating on an inert substrate is expensive. Luckily, there has been recent progress in the development of electrodes for the hydrogen evolution reaction. Most interesting of these are photo-cathodes, constructed of p-type semiconductors

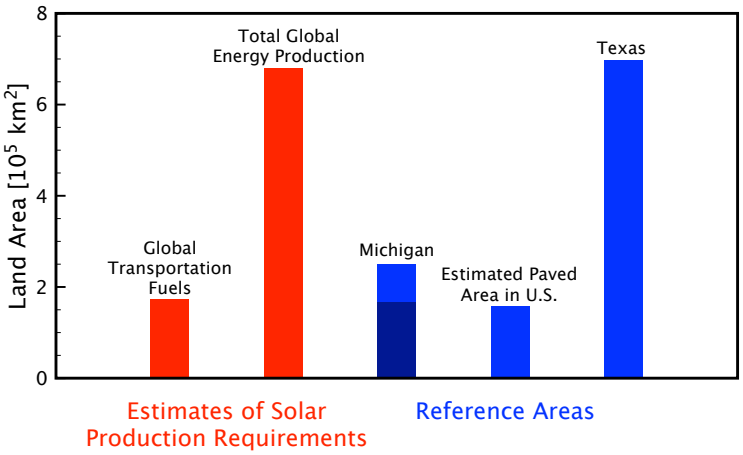

Figure 7.3: Estimated land area requirements for solar production of global energy demands. As discussed in the text, the analysis is performed on the basis of total energy requirements (i.e. rather than estimating production of gasoline and diesel fuel from solar energy, the analysis estimates requirements for the production of H_2 of equivalent energy). The bar for Michigan presents areas for the Upper (lighter blue) and Lower Peninsulas (darker blue).

such as Si, which can be used in tandem with n-type photo-anodes [35, 42]. This has the benefit of increasing the amount of light utilization, by using two different semiconductors that can absorb different wavelengths, as well as replacing expensive Pt electrodes with Si, which is abundant and inexpensive by comparison.

These economic requirements, of course, are also true of other solar energy technologies. In an attempt to develop a metric for comparing hydrogen production technologies, one group formulated an "overall figure of merit", based on the amount of CO_2 emission produced by a technology, the area required to produce a given amount of energy and the cost of producing a given amount of hydrogen (on the scale of 150 metric tons per day) including capital investment and operating costs [56]. The conclusion of the study was that of the renewable technologies investigated, H_2 production via photocatalytic water splitting and via photovoltaic electrolysis were indistinguishable by their figure of merit, and both were far more favorable than H_2 production via other renewable routes. While the photovoltaic route required slightly less land area and produced slightly less CO_2, the resulting capital and operating costs were significantly lower for photocatalysts water splitting [56]. While the cost analysis for some of the systems, especially photocatalytic water splitting, was a coarse estimate, the authors pointed out that many of the systems share similar requirements, such as electrical systems, pumping and fluid handling systems, etc. The major differences come in the materials with which the photons directly interact. The semiconductors for photovoltaics and photocatalysts are relatively inexpensive, while other technologies such as photothermal applications suffer from the requirement of very large concentrating mirrors, which are very expensive in comparison.

7.5 Conclusion

Photocatalytic conversion of water to hydrogen and oxygen is a potentially promising avenue to the future production of fuels from abundant solar energy. It has been known for several decades that some semiconductors can absorb solar photons and use the absorbed energy to produce hydrogen and oxygen from water. However, the process typically produces hydrogen at very low rates because of inherent deficiencies of the semiconductors. We have demonstrated that the addition of photo-excited plasmonic metal nanoparticles can enhance the photo-activity of semiconductors. Through a series of supporting experiments, the enhancement in both reactions was ascribed to the SPR-induced spatially non-homogeneous enhancement and concentration of electric fields around the Ag nanoparticles, which then increase the rate of charge carrier formation in the semiconductor, specifically near the semiconductor surface.

In the studies presented in this dissertation, we have investigated photocatalysts based on P25 TiO_2 particles because this material is so well studied and characterized that is it the de facto standard for comparison, even though its efficiency is not state-of-the-art. In the end, whatever semiconductor material(s) turn out to be the most promising, there is every reason to expect that the approach we have presented herein will translate to those materials. In the previous chapters we have illustrated the concept of composite plasmonic metal/semiconductor photocatalysts and investigated several relevant underlying mechanisms (especially the near-field electromagnetic enhancement mechanism).

We have also provided a framework to identify and predict the optimal construction of composites based on the optical properties of the constituent building blocks.

Our ever-improving understanding of the controlled synthesis of metal nanoparticles, coupled with the guiding predictive abilities of optical simulations, allows us to identify and synthesize plasmonic metal nanoparticles to maximize interaction with any semiconductor under solar illumination (Chapter 4). The importance of the spatial distribution of SPR-induced electric field enhancement was demonstrated. It is well known that the area between photo-excited plasmonic nanoparticles can display electric fields that are orders of magnitude higher than the fields around a single particle. This emphasizes the importance that controlling the geometric placement of the building blocks will have on the continued improvement of the particular class of composite photocatalysts. The so-called hot spots between plasmonic nanoparticles where electric fields can be enhanced by factors up to 10^6 may hold the key to designing highly efficient composite metal/semiconductor photocatalysts.

References

[1] Fujishima, A.; Honda, K. *Nature* **1972**, *238*, 37–38.

[2] Subramanian, V.; Wolf, E.; Kamat, P. V. *J. Phys. Chem. B* **2001**, *105*, 11439–11446.

[3] Arabatzis, I. M.; Stergiopoulos, T.; Bernard, M. C.; Labou, D.; Neophytides, S. G.; Falaras, P. *Appl. Catal. B* **2003**, *42*, 187–201.

[4] Subramanian, V.; Wolf, E. E.; Kamat, P. V. *J. Am. Chem. Soc.* **2004**, *126*, 4943–4950.

[5] Silva, C. G.; Juárez, R.; Marino, T.; Molinari, R.; García, H. *J. Am. Chem. Soc.* **2011**, *133*, 595–602.

[6] Primo, A.; Corma, A.; García, H. *Phys. Chem. Chem. Phys.* **2011**, *13*, 886–910.

[7] Tian, Z.-Q.; Ren, B. *Annu. Rev. Phys. Chem.* **2004**, *55*, 197–229.

[8] Tian, Y.; Tatsuma, T. *J. Am. Chem. Soc.* **2005**, *127*, 7632–7637.

[9] Awazu, K.; Fujimake, M.; Rockstuhl, C.; Tominaga, J.; Murakami, H.; Ohki, Y.; Yoshida, N.; Watanabe, T. *J. Am. Chem. Soc.* **2008**, *130*, 1676–1680.

[10] Christopher, P.; Ingram, D. B.; Linic, S. *J. Phys. Chem. C* **2010**, *114*, 9173–9177.

[11] Zhou, X.; Hu, C.; Hu, X.; Peng, T.; Qu, J. *J. Phys. Chem. C* **2010**.

[12] Kowalska, E.; Abe, R.; Ohtani, B. *Chem. Comm.* **2009**, 241–243.

[13] Kowalska, E.; Mahaney, O. O. P.; Abe, R.; Ohtani, B. *Phys. Chem. Chem. Phys.* **2010**, *12*, 2344–2355.

[14] Kumar, M. K.; Krishnamoorthy, S.; Tan, L. K.; Chiam, S. Y.; Tripathy, S.; Gao, H. *ACS Catal.* **2011**, *1*, 300–308.

[15] Zhai, W.; Xue, S.; Zhu, A.; Luo, Y.; Tian, Y. *ChemCatChem* **2011**, *3*, 127–130.

[16] Ingram, D. B.; Linic, S. *J. Am. Chem. Soc.* **2011**, *133*, 5202–5205.

[17] Chen, J.-J.; Wu, J. C. S.; Wu, P. C.; Tsai, D. P. *J. Phys. Chem. C* **2011**, *115*, 210–216.

[18] Thimsen, E.; Le Formal, F.; Grätzel, M.; Warren, S. C. *Nano Lett.* **2011**, *11*, 35–43.

[19] Liu, Z.; Hou, W.; Pavaskar, P.; Aykol, M.; Cronin, S. B. *Nano Lett.* **2011**, *11*, 1111–1116.

[20] Primo, A.; Marino, T.; Corma, A.; Molinari, R.; García, H. *J. Am. Chem. Soc.* **2011**.

[21] El-Sayed, M. A. *Acc. Chem. Res.* **2001**, *34*, 257–264.

[22] Burda, C.; Chen, X.; Narayanan, R.; El-Sayed, M. A. *Chem. Rev.* **2005**, *105*, 1025–1102.

[23] Kelly, K. L.; Coronado, E.; Zhao, L. L.; Schatz, G. C. *J. Phys. Chem. B* **2003**, *107*, 668–677.

[24] Brus, L. *Acc. Chem. Res.* **2008**, *41*, 1742–1749.

[25] U.S. Department of Energy, *Annual Energy Outlook*; Technical Report, 2011.

[26] Gust, D.; Moore, T. A.; Moore, A. L. *Acc. Chem. Res.* **2009**, *42*, 1890–1898.

[27] Hartmann, P.; Lee, D.-K.; Smarsly, B. M.; Janek, J. *ACS Nano* **2010**, *4*, 3147–3154.

[28] Paulose, M.; Shankar, K.; Yoriya, S.; Prakasam, H. E.; Varghese, O. K.; Mor, G. K.; Latempa, T. A.; Fitzgerald, A.; Grimes, C. A. *J. Phys. Chem. B* **2006**, *110*, 16179–16184.

[29] Leng, W. H.; Barnes, P. R. F.; Juozapavicius, M.; O'Regan, B. C.; Durrant, J. R. *Journal of Physical Chemistry Letters* **2010**, *1*, 967–972.

[30] Goldberger, J.; He, R.; Zhang, Y.; Lee, S.; Yan, H.; Choi, H.-J.; Yang, P. *Nature* **2003**, *442*, 599–602.

[31] Mor, G. K.; Shankar, K.; Paulose, M.; Varghese, O. K.; Grimes, C. A. *Nano Lett.* **2005**, *5*, 191–195.

[32] Prakasam, H. E.; Shankar, K.; Paulose, M.; Varghese, O. K.; Grimes, C. A. *J. Phys. Chem. C* **2007**, *111*, 7235–7241.

[33] Zhu, K.; Neale, N. R.; Miedaner, A.; Frank, A. J. *Nano Lett.* **2007**, *7*, 69–74.

[34] Grimes, C. A. *J. Mater. Chem.* **2007**, *17*, 1451–1457.

[35] Maiolo III, J. R.; Kayes, B. M.; Filler, M. A.; Putnam, M. C.; Kelzenberg, M. D.; Atwater, H. A.; Lewis, N. S. *J. Am. Chem. Soc.* **2007**, *129*, 12346–12347.

[36] Wei, Z.; Liu, Z.; Jiang, R.; Bian, C.; Huang, T.; Yu, A. *J. Solid State Electrochem.* **2010**, *14*, 1045–1050.

[37] Aurora, P.; Rhee, P.; Thompson, L. *J. Electrochem. Soc.* **2010**, *157*, K152–K155.

[38] Ranney, E.; Mansfield, J.; Sun, K.; Schwank, J. *J. Mater. Res.* **2010**, *25*, 89–95.

[39] Banerjee, S.; Mohapatra, S. K.; Misra, M. *J. Phys. Chem. C* **2011**.

[40] Roy, P.; Berger, S.; Schmuki, P. *Angew. Chem. Int. Ed.* **2011**, *50*, 2904–2940.

[41] Khaselev, O.; Turner, J. A. *Science* **1998**, *280*, 425–427.

[42] Hou, Y.; Abrams, B. L.; Vesborg, P. C. K.; Björketun, M. E.; Herbst, K.; Bech, L.; Setti, A. M.; Damsgaard, C. D.; Pedersen, T.; Hansen, O.; Rossmeisl, J.; Dahl, S.; Nørskov, J. K.; Chorkendorff, I. *Nat. Mater.* **2011**.

[43] Chen, C. T.; Cahan, B. D. *J. Opt. Soc. Am.* **1981**, *71*, 932–934.

[44] Lindgren, T.; Wang, H.; Beermann, N.; Vayssieres, L.; Hagfeldt, A.; Lindquist, S.-E. *Solar Energy Materials & Solar Cells* **2002**, *71*, 231–243.

[45] Cesar, I.; Kay, A.; Martinez, J. A. G.; Grätzel, M. *J. Am. Chem. Soc.* **2006**, *128*, 4582–4583.

[46] Cesar, I.; Sivula, K.; Kay, A.; Zboril, R.; Grätzel, M. *J. Phys. Chem. C* **2009**, *113*, 772–782.

[47] Souza, F. L.; Lopes, K. P.; Longo, E.; Leite, E. R. *Physical Chemistry Chemical Physics* **2009**, *11*, 1215–1219.

[48] Cowan, A. J.; Barnett, C. J.; Pendlebury, S. R.; Barrosos, M.; Sivula, K.; Grätzel, M.; Durrant, J. R.; Klug, D. R. *Journal of the American Chemical Society* **2011**.

[49] Klahr, B. M.; Hamann, T. W. *Journal of Physical Chemistry C* **2011**.

[50] Peter, L. M.; Wijayantha, K. G. U.; Tahir, A. A. *Faraday Discussions* **2011**.

[51] Pourbaix, M. *Atlas of electrochemical equilibria in aqueous solutions*; National Association of Corrosion Engineers, 1974.

[52] Blizanac, B. B.; Ross, P. N.; Markovic, N. M. *Electrochim. Acta* **2007**, *52*, 2264–2271.

[53] Christopher, P.; Xin, H.; Linic, S. *Nat. Chem.* **2011**, *3*, 467–472.

[54] Torimoto, T.; Horibe, H.; Kameyama, T.; ichi Okazaki, K.; Ikeda, S.; Matsumura, M.; Ishikawa, A.; Ishihara, H. *J. Phys. Chem. Lett.* **2011**, *2*, 2057–2062.

[55] Brown, L. *Paving the Planet: Cars and Crops Compete for Land*; Technical Report, 2011.

[56] Ewan, B. C. R.; Allen, R. W. K. *Int. J. Hydrogen Energy* **2005**, *30*, 809–819.